



**Università degli Studi di Padova**

---

DIPARTIMENTO DI INGEGNERIA CIVILE, EDILE ED AMBIENTALE  
Corso di Dottorato di Ricerca in Scienze dell'Ingegneria Civile ed Ambientale

TESI DI DOTTORATO DI RICERCA  
CICLO XXIX

**Long-term evolution of meandering rivers  
flowing above heterogeneous floodplains**

Coordinatore:  
**Ch.mo Prof. Stefano Lanzoni**

Supervisore:  
**Ch.mo Prof. Stefano Lanzoni**

Dottorando:  
**Manuel Bogoni**



*Grazie  
a mamma  
e papà*





# Contents

<b>Abstract</b>	<b>7</b>
<b>1 Introduction</b>	<b>9</b>
1.1 Sediment and vegetation . . . . .	9
1.2 Floodplain structure . . . . .	10
1.3 Numerical modeling . . . . .	13
1.4 Aims and outline of the thesis . . . . .	15
<b>2 Mathematical modelling of meander dynamics</b>	<b>17</b>
2.1 References and notations . . . . .	17
2.2 The long-term migration of the river . . . . .	19
2.3 Floodplain features . . . . .	24
2.4 The flow field . . . . .	26
<b>3 Statistical tools</b>	<b>31</b>
3.1 Fourier Analysis . . . . .	31
3.2 Singular Spectrum Analysis . . . . .	32
3.3 Multivariate Singular Spectrum Analysis . . . . .	33
3.4 Principal Component Analysis . . . . .	34
<b>4 On the floodplain heterogeneity</b>	<b>37</b>
4.1 A test case: two vs. three erodibility environments . . . . .	38
4.2 A synthetic database of meanders . . . . .	45
4.3 Time analyses . . . . .	47
4.4 Spatial analyses . . . . .	52
4.5 Discussion . . . . .	65

<b>5</b>	<b>On the floodplain singularities</b>	<b>69</b>
5.1	Mathematical framework . . . . .	69
5.2	Application to the Mississippi River . . . . .	89
5.3	Results . . . . .	94
5.4	Discussion . . . . .	97
<b>6</b>	<b>Conclusions and future developments</b>	<b>101</b>
	<b>List of tables</b>	<b>105</b>
	<b>List of figures</b>	<b>107</b>
	<b>References</b>	<b>111</b>

# Abstract

Floodplains, and rivers therein, constitute complex systems whose simulation involves modelling of hydrodynamic, morphodynamic, chemical, and biological processes which act, affecting each other, over a wide range of time scales (from days to centuries). Floodplain morphology and stratigraphy are shaped by the interplay of water flow, erosion, and deposition consequent to repeated flood events, as the river dissecting the floodplain evolves through feedbacks between bars, channels, vegetation and sediment characteristics shaping the floodplain itself.

The first topic of this thesis concerns the mutual interactions that leads to self-formed floodplains, produced by the sedimentary processes associated with the migration of river bends and the formation of abandoned oxbow lakes consequent to the cutoff of mature meanders. The second topic addresses the presence of internal boundary conditions able to affect the main flow field and thus the curvature-driven flow that drives bend migration. Point bar deposits and oxbow lakes are the products of lateral bend migration and meander cutoffs. The sediment deposits characterizing these geomorphic units link together the long term evolution of an alluvial river and the surrounding floodplain, altering the soil composition and, hence, bank strength controlling the rate of channel meandering. On the other hand, a localized forcing internal to the main flow field (e.g., a variation in bed slope or in flow discharge) propagates either upstream or downstream, affecting the river dynamics. Multivariate statistical and spectral tools may disclose the complexity of the resulting planform geometries, either simulated or natural, ensuring an objective comparison.



# Chapter 1

## Introduction

Floodplains, and rivers therein, constitute complex systems whose simulation involves modelling of hydrodynamic, morphodynamic, chemical, and biological processes which act, affecting each other, over a wide range of time scales (from days to centuries). Floodplain morphology and stratigraphy are shaped by the interplay of water flow, erosion, and deposition consequent to repeated flood events (Howard, 1996). This long-term interaction is controlled by the planform configuration, as the river dissecting the floodplain evolves through feedbacks between bars, channels, floodplain, vegetation and sediment characteristics (Kleinhans, 2010), shaping the floodplain itself (Figure 1.1).

### 1.1 Sediment and vegetation

Sediment accumulates across the floodplain mainly as a consequence of over-bank flooding events and lateral accretion associated with channel migration (Day et al., 2008). Neck and chute cutoffs of meanders, channel avulsions, crevasse splay sedimentation, over-bank spilling of tie and tributary channels, and floodplain channel occurrence also contribute to design the floodplain structure (Howard, 1996; Slingerland and Smith, 2004; Day et al., 2008; Swanson et al., 2008; David et al., 2016). On the other hand, sediment is continuously removed from the floodplain and swept back to the channel as a consequence of channel migration, i.e., bank erosion and channel cutting (Dunne et al., 1998; Aalto et al., 2008; Swanson et al., 2008; Lauer and Parker, 2008; Kleinhans, 2010). Understanding how sediment is transported onto a floodplain and where fine material likely accumulates is fundamental for both morphological and environmen-

tal reasons. The interplay of vertical accretion, channel migration and sediment sorting controls floodplain stratigraphy and, hence, the structure of aquifers and the possible location of oil and gas reservoirs (Howard, 1996). In addition, silt and clay particles are responsible for the fate and the transport of chemical species (carbon, nutrients, heavy metals, pollutant in general) adsorbed on their surface (Alin et al., 2008).

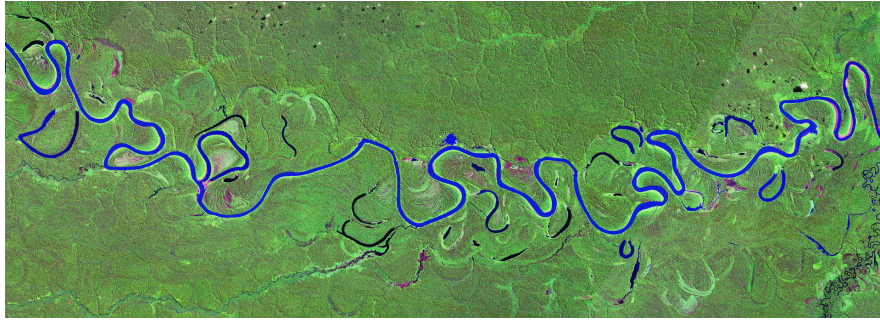


Figure 1.1: A Landsat detail of Jurua River floodplain, Brazil (source: <http://earthexplorer.usgs.gov>). Actual size of frame area is about  $85 \times 31$  km. River flows from left to right. Many of the typical features concerning river-floodplain systems are visible: skewed meanders, point bars at the inner side of bends, scroll bars, ancient river paths, incipient forming cutoffs, recent cutoffs still flooded, older oxbow lakes covered by vegetation of the Amazon rainforest.

Riparian vegetation affects and, in turn, is affected by morphodynamic processes (van Oorschot et al., 2016). Focusing on the active role, vegetation moderates the erosion processes, enhances the deposition of sediment (Zen et al., 2016), and, when flooded, affects the hydraulic resistance on the basis of plant characteristics, e.g. density, height, thickness (van Oorschot et al., 2016). On the other hand, rivers provide water, nutrients and sediment through flooding and the groundwater flow (Perucca et al., 2006), but can also erode, undermine or uproot vegetated areas (Zen et al., 2016).

## 1.2 Floodplain structure

Point bars, scroll bars, and oxbow lakes are widespread floodplain features generated by the lateral migration of meander loops. As a consequence, they alter the sedimentary structure of the previous floodplain configuration, causing a heterogeneous distribution of the erosion resistance to the river migration. Thus floodplain is simultaneously

formed and destroyed (Kleinhans, 2010). As a meander migrates eroding the outer bank, the point bar surface at the inner bank develops a characteristic ridge-and-swale topography (Miall, 1985), resulting in preserved scroll bars parallel to the channel axis (Nanson, 1980). Scroll bars are fundamental geomorphic building units, and potential reservoirs for water, oil and gas (van De Lageweg et al., 2014). Coarse grained sediments typically accumulate on the ridge basement, while finer sediment (silt and clay) deposits on the upper part (Nanson, 1980), yielding an heterolithic stratification of interbedded sand and mud deposits with lateral accretion surfaces (van De Lageweg et al., 2014). Sedimentation may occur in old scroll bars by decanting, consequently to the creation of crevasse-splays through the main channel levees (Gautier et al., 2007). Vegetation constitutes an important element in the formation of the ridge-and-swale configuration of point bars (Swanson et al., 2008), affecting the processes of bar-floodplain conversion (Schuurman et al., 2016; van Oorschot et al., 2016).

Oxbow lakes are typical landforms of flat floodplain environments (Gagliano and Howard, 1984) which form as a result of cutoff events in response to channel shifting processes (Gay et al., 1998; Hooke, 2004; Constantine et al., 2010; Grenfell et al., 2012). As a cutoff occurs, point bar formation and outer bank erosion stop instantaneously favouring a progressive shallowing and narrowing of the abandoned reach (Toonen et al., 2012) because of a subsequent infilling by fine grained sediments forming less erodible plugs. Production of oxbow lakes creates accommodation space for sediment storage in floodplains, important to the development of lentic sedimentary environments, landforms and ecosystems, and carbon and pollutant reservoirs (Lewin and Ashworth, 2014). The repeated cutoff events that determine the formation of oxbow lakes, removing older, well developed meanders, limit the planform complexity of the channel and, consequently, ensure the establishment of statistically stationary evolving planform configurations (Camporeale et al., 2005; Frascati and Lanzoni, 2010). Oxbow lake geometry is thus a story-holder of the river migration dynamics (Schwenk et al., 2015) and a control factor for the future evolution of the system.

The effects of floodplain heterogeneity on meandering dynamics has been addressed by various researchers, as meandering patterns throughout complex floodplain deposits differ from those typical of homogeneous floodplain deposits (Hudson and Kesel, 2000), and channel sinuosity is affected by the characteristics of the floodplain surface (Lazarus and Constantine, 2013). In their pioneering works, Howard (1996) and Sun et al. (1996)



Figure 1.2: Examples of self-formed floodplains (source: Google Earth Pro). Geomorphic features are from: (a) Darling River, Australia,  $31^{\circ} 44' S$   $143^{\circ} 15' E$ ; (b) Ob River, Russia,  $61^{\circ} 9' N$   $75^{\circ} 22' E$ ; (c) Chulym River, Russia,  $57^{\circ} 7' N$   $86^{\circ} 1' E$ ; (c) Chulym River, Russia,  $57^{\circ} 11' N$   $87^{\circ} 41' E$ ; (e) Ucayali River, Peru,  $7^{\circ} 25' S$   $75^{\circ} 0' W$ ; (f) Jurua River, Brazil,  $4^{\circ} 19' S$   $66^{\circ} 35' W$ .



used simplified models, coupling the flow field solution derived by Johannesson and Parker (1989) and the bank erosion law of Ikeda et al. (1981) to reproduce the geometric forms of individual meanders observed in natural sedimentary environments with different erodibility (point bars, floodplain, and oxbow lake deposits). More recently, (Güneralp and Rhoads, 2011) and Motta et al. (2012b) published two similar works dealing with the influence of a priori, statistically-generated heterogeneous floodplain on rates and patterns of migration of meandering streams. Both studies concluded that adopting a relatively simple flow field model, and prescribing a priori the erodibility distribution across the valley allow to generate bend complexity and planform irregularity similar to those observed in alluvial rivers, both visually and in their spectra of planform curvature. Furthermore, in the last years, the role of floodplain erodibility produced by vegetation cover has gained progressively more attention and recognition of its relevance (e.g., Perucca et al., 2006; Solari et al., 2016; van Oorschot et al., 2016; Zen et al., 2016).

Physiographic constraints, e.g. valley width (Nicoll and Hickin, 2010), and tectonic shift (Schumm, 1986) can also play an important role in determining floodplain evolution, as well as localized variations in the flow field forcing, e.g. a variation in the valley slope or the confluence of a tributary.

### 1.3 Numerical modeling

The wide variability of the time scales characterizing the changes in channel planform, floodplain morphology, and vegetation dynamics and the complexity of the additional processes that contribute to shape the terrain (climate changes influencing the hydrological and sedimentological regimes, weathering of sediment stored on floodplains, multiplicity of bank erosion processes) preclude the use of deeply detailed models able to encompass the entire bio-morphodynamic behaviour of a floodplain-river systems (Howard, 1996; Perucca et al., 2006). As a consequence, relatively simplified models have been developed by suitably selecting the physical processes to be taken into account and simplifying the relative process laws (see, among others, Howard, 1996; Sun et al., 1996; Camporeale et al., 2005; Perucca et al., 2006; Lanzoni and Seminara, 2006; Frascati and Lanzoni, 2010; Güneralp and Rhoads, 2011; Motta et al., 2012a; Frascati and Lanzoni, 2013; Zen et al., 2016).

The complex structure of the flow field within river bends has been disclosed since

the last century (Einstein, 1926). The interplay between the lateral pressure gradient associated with a lateral slope of the free surface developing in a bend because of the curved trajectories, the free vortex effect generated by an inner flow faster than the outer flow, and the topographic steering due to longitudinal fluctuations of bed elevations leads to the establishment of a three-dimensional helicoidal flow (Seminara, 2006) along the river bend. The secondary flow circulation that establishes in the cross sections drives the sediments motion through the section itself and along the reach. Erosion and deposition processes, in turn, are responsible for the dynamics of the system leading to the river migration (Figure 1.3).

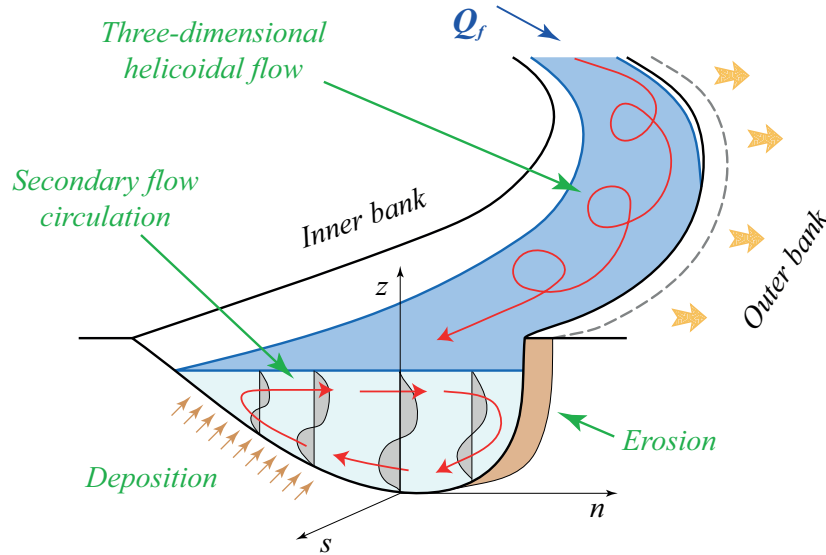


Figure 1.3: Sketch of the flow field that establishes into a river bend and of the erosion and deposition processes leading to channel migration.

However, most of the mathematical frameworks and applications concerns constant flow field properties over the entire domain, thus they introduce a relatively strong limitation in modelling a natural scenario which might include, e.g., variation in the valley slope due to a knickpoint, variation in the discharge because of a tributary confluence, backwater effects (Figure 1.4).



Figure 1.4: A Landsat detail of the confluence of Arkansas River into Mississippi River, US (source: <http://earthexplorer.usgs.gov>). Actual size of frame area is about  $65 \times 92$  km. Mississippi flows from top to bottom, while Arkansas from left to right.

## 1.4 Aims and outline of the thesis

In the present contribution the attention is focused on two particular aspects of the river-floodplain dynamics. The first concerns the role of floodplain heterogeneity on determining the planform shape of the channel, whose dynamics, in turn, contributes to build up the sedimentological structure of the floodplain itself. The second aspect is related to the role of internal localized forcing factors able to modify the flow conditions of the domain, and thus the curvature-driven secondary flow. The first topic will be referred to as self-formed floodplain, the second topic as boundary conditions internal to the flow domain. The ultimate goal is to build up a model of the floodplain-river system based on a reliable procedure broadening the domain of applicability domain of the existing mathematical models. In order to keep the lowest possible level of complexity, the present work accounts for neck cutoff meandering river, ignoring the chute-dominated cases.

The thesis is organized as follows. Chapter 2 provides the fundamental ingredients necessary to build a numerical framework able to simulate the dynamics of meandering rivers. The relevant variables are outlined, as well as the various mathematical tools required to deal with the flow field into sinuous rivers and the floodplain dynamics. Chapter 4 focuses on the interplay between river dynamics and self-formed floodplains. A test case will disclose the roles of the involved elements (floodplain, oxbow lakes, scroll bars), and statistical and spectral tools will be used to compare quantitatively planforms generated by numerical models and natural planforms. The methods of analyses are outlined in Chapter 3. Chapter 5 deals with the presence of an internal boundary condition affecting the flow field. An extension of an existing mathematical model will be developed and applied to a real case, considering different scenarios. Finally, Chapter 6 closes the thesis and provides some suggestions for future research.

## Chapter 2

# Mathematical modelling of meander dynamics

This chapter outlines the mathematical and numerical tools required to build a model able to handle the long-term migration of meandering rivers flowing above heterogeneous floodplains. The main quantities and variables involved in the problem are outlined in Section 2.1. The frame of the numerical modelling builds upon other models available in literature, e.g. Camporeale et al. (2005); Lanzoni et al. (2006); Lanzoni and Seminara (2006); Frascati and Lanzoni (2009). It consists of a migration model for the river axis (Section 2.2), a model for the floodplain structure (Section 2.3), and a morphodynamic model for the curvature-driven flow field (Section 2.4).

### 2.1 References and notations

With reference to the sketch of Figure 2.1, let  $(x^*, y^*, z^*)$  be a Cartesian reference system with  $x^*$  the longitudinal flow direction, and  $(s^*, n^*, z^*)$  a orthogonal intrinsic reference system. Hereafter the superscript  $*$  will denote dimensional quantities. Moreover,  $R^*$  is the local curvature radius of the river axis, and  $\theta$  the local angle of the axis tangent with respect to the longitudinal direction. The curvature by definition is  $\mathcal{C}^* = 1/R^*$ . As far as the channel cross section is concerned,  $2B_0^*$  and  $D_0^*$  are the width and the depth of a reference straight rectangular channel having the same flow discharge,  $2B_0^*D_0^*U_0^*$ , bed slope  $S$ , and characteristic grain size  $d_s^*$  of the considered meandering river (e.g.,  $d_{50}^*$ ), with  $U_0^*$  the cross-sectionally averaged velocity. In addition,  $\eta^*$  and  $H^*$  are the local

bed elevation and the free surface elevation with respect to a given datum, while  $D^* = H^* - \eta^*$  is the local flow depth. The local velocity components along the longitudinal, transverse and vertical direction are  $u^*$ ,  $v^*$ , and  $w^*$ , respectively.

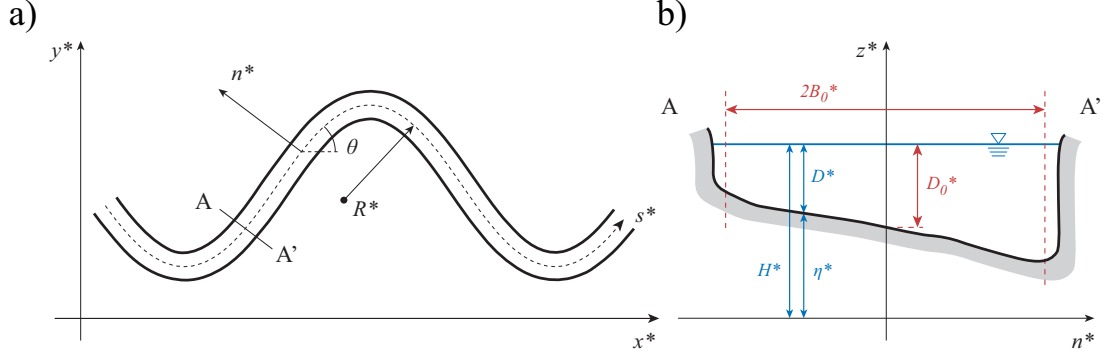


Figure 2.1: Reference systems and notation for a) the river planform and b) the cross-section.

The next step is to scale the above relevant quantities through the uniform flow parameters. Hence:

$$(x^*, y^*, s^*, n^*, R^*) = B_0^* (x, y, s, n, R) \quad (2.1a)$$

$$(z^*, \eta^*, H^*, D^*) = D_0^* (z, \eta, H, D) \quad (2.1b)$$

$$(u^*, v^*, w^*) = U_0^* (u, v, w) \quad (2.1c)$$

A curvature parameter may be defined as follows:

$$\nu_0 = \frac{B_0^*}{R_0^*} \quad (2.2)$$

where  $R_0^*$  is a reference radius of channel axis curvature, e.g. the minimum value attained along the investigated reach. The fundamental hypothesis for deriving the mathematical model is that  $\nu_0$  is a small parameter, i.e. the river planforms are made by sufficiently gentle and wide bends such that the local curvature radius is much larger than the cross section width. The dimensionless local curvature  $\mathcal{C}$  turns out to be (Frascati and Lanzoni, 2013):

$$\mathcal{C} = -\frac{1}{\nu_0} \frac{\partial \theta}{\partial s} \quad (2.3)$$

The relevant morphological parameters are the half width to depth ratio  $\beta$ , the Shields

number  $\tau_*$  and the dimensionless grain size  $d_s$ , defined as follows:

$$\beta = \frac{B_0^*}{D_0^*} \quad (2.4a)$$

$$\tau_* = \frac{C_f U_0^{*2}}{\Delta g d_s^*} \quad (2.4b)$$

$$d_s = \frac{d_s^*}{D_0^*} \quad (2.4c)$$

where  $g$  is the gravity acceleration,  $\Delta = (\rho_s - \rho)/\rho$  is the submerged specific gravity of the sediment ( $\rho_s \simeq 2650 \text{ kg / m}^3$ ,  $\rho = 1000 \text{ kg / m}^3$ ), and  $C_f$  is the friction coefficient. Velocity and depth are related together through the Froude number:

$$F_0 = \frac{U_0^*}{\sqrt{g D_0^*}} \quad (2.5)$$

Finally, the sediment motion leads to a volumetric discharge per unit width denoted as  $q_s^*$ , which may be scaled as:

$$\Phi = \frac{q_s}{R_p \nu} \quad (2.6)$$

where  $\nu \simeq 10^{-6} \text{ m}^2/\text{s}$  is the kinematic viscosity of water, and  $R_p$  is the Reynolds particle number:

$$R_p = \frac{\sqrt{g \Delta} d_s^{*3/2}}{\nu} \quad (2.7)$$

Hereafter, under dominant bedload transport  $\Phi$  is computed through the formula of Parker (1990). The particle Reynolds number, which controls the intensity of suspended load transport (see, e.g., Frascati and Lanzoni, 2010) is also considered to evaluate the threshold above which suspended load takes place (Van Rijn, 1984a). In this case the total load predictor of Engelund and Hansen (1967) is used to compute  $\Phi$ . Moreover,  $R_p$  is used to establish whether the river bed is flat or dune-covered (Van Rijn, 1984b) when computing the friction coefficient  $C_f$  through the Engelund and Hansen (1967) method.

## 2.2 The long-term migration of the river

The long-term migration of river planforms is driven by the complex interplay of the processes of erosion at the inner bank and deposition at the outer bank, possibly leading to spatial and temporal variation of the local channel width (Figure 1.3). Among others, the affecting factors may be the type of bank failure, the composition of the banks

and of the slumped block material, and the vegetation properties. The erosion and deposition processes usually occur at different times and different time scales (Asahi et al., 2013). However, many meandering rivers tend to have a near constant width as channel sinuosity evolves (Parker et al., 2011), showing a normal distribution of channel widths when the fluvial system is subjected to a steady-forcing discharge (Wickert et al., 2013). Eventually, the typical ridge-and-swale bar topography develops (van De Lageweg et al., 2014). This scenario requires an active communication between bank erosion at the outer bend, i.e. bank pull, and bank growth at the inner bend, i.e. bank push (Eke et al., 2014; van De Lageweg et al., 2014; Schuurman et al., 2016). As a consequence, a constant width of the river cross section may be assumed as a first approximation, and the river path may be described by its centerline.

Referring to the planimetric sketch of Figure 2.1, the configuration of the channel axis at a certain time  $t$  may be described by the current distribution of angles  $\theta(s^*, n^*)$  formed by the local tangent to the channel axis with the longitudinal direction. Indeed, Seminara et al. (2001) demonstrated that the planimetric evolution at the generic location  $s$  along the river axis is described by the following integro-differential equation:

$$\frac{\partial \zeta}{\partial s} = \frac{\partial \theta}{\partial t} - \frac{\partial \theta}{\partial s} \int_0^s \zeta \frac{\partial \theta}{\partial s} ds \quad (2.8)$$

where the lateral migration velocity  $\zeta$  and the time  $t$  are scaled as:

$$\zeta^* = U_0^* \zeta \quad (2.9a)$$

$$t^* = \frac{U_0^*}{B_0^*} t \quad (2.9b)$$

Equation (2.8) drives the lateral migration of the river path across the floodplain over the time, producing a local displacement  $\xi_n(s)$  normal to the channel axis:

$$\frac{d\xi_n(s)}{dt} = \zeta(s) \quad (2.10)$$

Because of the previous assumption of nearly constant cross section width, the relation proposed by Ikeda et al. (1981) to model the river migration across the valley surface may be assumed. In dimensionless form, the relation reads:

$$\zeta = E U_b \quad (2.11)$$

where  $E$  is a dimensionless long-term erosion coefficient, while  $U_b = U_b^*/U_0^*$  is the dimensionless excess near-bank velocity, i.e. the difference between the longitudinal velocity



$U|_{n=1}$  at the outer bank ( $n = n^*/B_0^* = 1$ ) and the longitudinal velocity  $U|_{n=-1}$  at the inner bank ( $n = n^*/B_0^* = -1$ ). All the involved terms are function of the coordinate  $s$  along the river centerline.

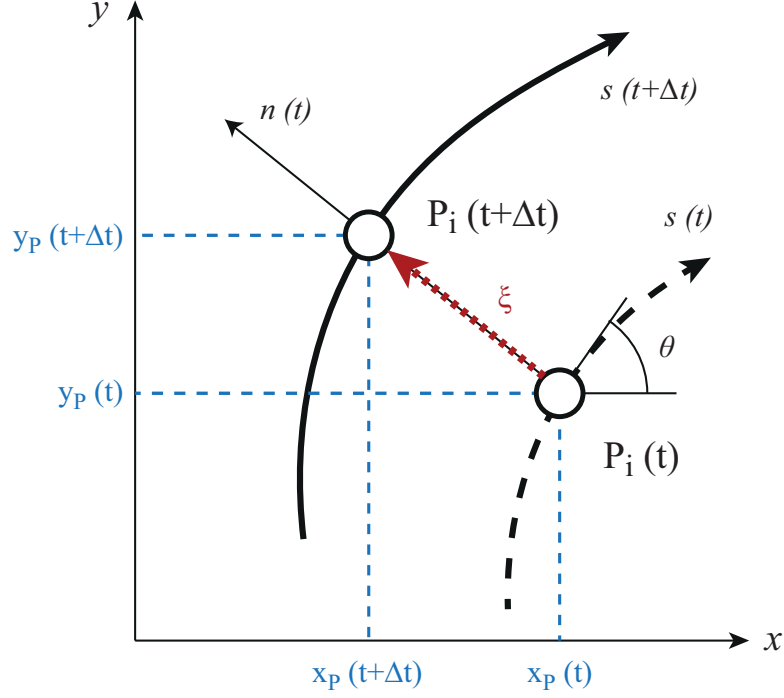


Figure 2.2: Sketch of the migration of a point  $P$  lying on the channel axis, due to the displacement from the configuration  $s(t)$  to the new configuration  $s(t + \Delta t)$ . Quantities may be either dimensional or dimensionless, the scaling factor being  $B_0^*$ .

The problem outlined so far is solved numerically by discretizing the dimensionless river centerline  $s$  through a polyline made by  $N$  points  $P_i(x_i, y_i)$ , defined with respect to the Cartesian reference system of Figure 2.1. As described by the sketch in Figure 2.2, the differential equation (2.10) is solved numerically through finite differences. At each dimensionless time step  $t^{k+1} = t^k + \Delta t^k$ , the migration of the  $i$ th node in the direction  $n$  normal to  $s$  is computed through a time marching procedure of the form (Crosato, 1990):

$$x_i^{k+1} = x_i^k - \Delta t_i^k \frac{\zeta_i^k + \zeta_i^{k-1}}{2} \sin \theta_i^k, \quad (2.12)$$

$$y_i^{k+1} = y_i^k + \Delta t_i^k \frac{\zeta_i^k + \zeta_i^{k-1}}{2} \cos \theta_i^k, \quad (2.13)$$

where  $x_i^{k+1} = x_i(t^{k+1})$ ,  $y_i^{k+1} = y_i(t^{k+1})$ , and  $\zeta_i^k = E_i^k U_{bi}^k$ . The value  $\theta_i^k$  of the local tangent angle is computed by backward and forward averaging (Lanzoni and Seminara, 2006):

$$\theta_i^k = \frac{1}{2} \left( \arctan \frac{y_{i+1}^k - y_i^k}{x_{i+1}^k - x_i^k} + \arctan \frac{y_i^k - y_{i-1}^k}{x_i^k - x_{i-1}^k} \right) \quad (2.14)$$

This angle is also used to discretize the geometrical relationship (2.3) and to determine the local value of the dimensionless curvature  $\mathcal{C}_i^k$ :

$$\mathcal{C}_i^k = -\frac{1}{\nu_0} \frac{\theta_{i+1}^k - \theta_{i-1}^k}{2\Delta s_i^k} \quad (2.15)$$

where  $\Delta s_i^k$  is the dimensionless distance between two consecutive points. The possible numerical anomalies arising from the curvature computation (Schwenk et al., 2015) are filtered out by using a Savitzky-Golay smoothing filter (Orfanidis, 1995; Motta et al., 2012a). The time step size  $\Delta t_i^k$  is controlled by requiring that:

$$\Delta t_i^k \leq \alpha \left( \frac{\Delta s_i^k}{E_i^k U_{bi}^k} \right)_{\max} \quad (2.16)$$

where  $\alpha$  is a parameter defining the threshold between stable and unstable computations, to be chosen empirically ( $\alpha \sim 10^{-2}$ ) on the basis of a balance between computational effort and accuracy of the numerical solution (Crosato, 1990; Lanzoni and Seminara, 2006).

Since the deformation experienced by the channel axis at each time step leads to continuous variations of  $\Delta s_i^k$ , the mesh is periodically re-built to maintain quasi-uniformity of the node spacings, adding or removing nodes to maintain the value of  $\Delta s_i^k$  into the range 2/3 and 4/3.

The progressive elongation of the channel axis produces neck cutoffs, whereby the upstream and downstream portions of a bend loop approach each other and eventually intersect. The meander loop is then bypassed, and the older, more sinuous reach is abandoned by the active river, forming an oxbow lake when sedimentation closes its ends. These processes may last many years (Gagliano and Howard, 1984) but, because of the long time scales characterizing the evolution of the river planform, they can be assumed to occur instantaneously in the simulation model. Following Howard and Knutson (1984) and Sun et al. (1996), the presence of potential neck cutoffs is detected by controlling the dimensionless distance between a given point  $P_i$  and the nearby points  $P_{i+r}$  located sufficiently downstream (e.g.,  $r \geq 8$ ). This control is made through the

algorithm developed by Camporeale et al. (2005) which improves the computational efficiency of the model. When the computed Cartesian distance between nodes  $P_i$  and  $P_{i+r}$  is lower than a threshold value, say  $\Delta s_r = 2.2$ , all the points  $P_{i+j}$ ,  $j = 1, r - 1$  are removed from the computational grid, defining a new oxbow lake (Figure 2.3). A few nodes upstream of  $P_i$  and downstream of  $P_{i+r}$  (e.g.,  $P_{i-q}$ ,  $P_{i+r+q}$ ,  $q = 1, 2, 3$ ) are also removed to prevent the formation of a high-curvature river reach (Frascati and Lanzoni, 2009) that, in nature, is unlikely to persist owing to the rapid smoothing action of the current and the along river propagation of the geometric disturbances generated by the cutoff even (Hooke, 1995; Camporeale et al., 2008).

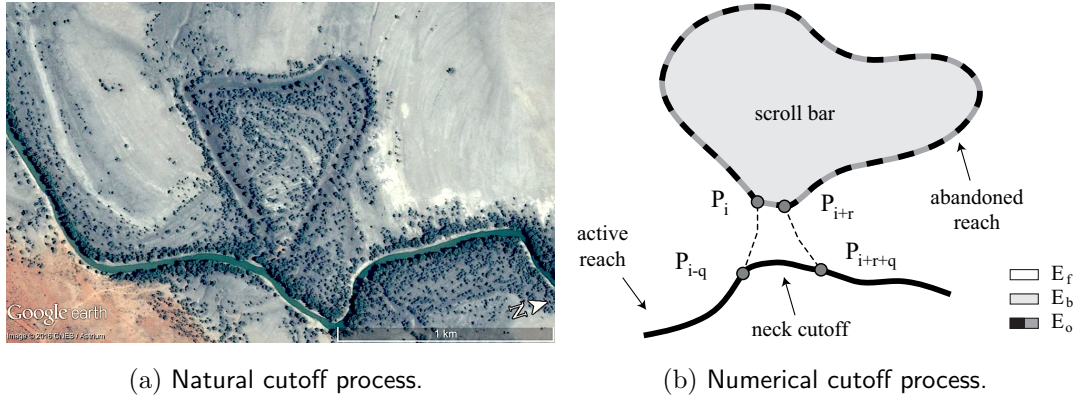


Figure 2.3: Example of (a) a natural neck cutoff process producing a different geomorphic environment inside the oxbow lake contour (Darling River, Australia,  $31^{\circ} 33' S$   $143^{\circ} 30' E$ , source: Google Earth Pro), and of (b) the numerical modelling of neck cutoff occurrence, with the formation of two new environments, namely the oxbow lake formed by the abandoned reach and the inner scroll bar bounded by the previous element. Symbols are as follows:  $r$  determines the points that are considered to check the occurrence of a incipient neck cutoff;  $q$  is the number of point removed to avoid the presence of a high-curvature river reach after a cutoff;  $E_f$ ,  $E_b$ , and  $E_o$  are the erodibility coefficients assigned to the pristine floodplain, the scroll bar environment and the oxbow lake environment, respectively.

The alternate form of cutoff, the chute cutoff, is not treated in this dissertation.

As observed above, the total length of the channel and the bed slope change over time due to the elongation driven by migration and the shortening due to cutoff occurrences. As a consequence, suitable relations must be imposed in order to keep consistent

steady flow and sediment transport conditions. Assuming a constant discharge and a temporally constant floodplain gradient, the relevant physical parameters between two time steps  $k$  and  $k + 1$  are updated as follows:

$$\frac{\beta^{k+1}}{\beta^k} = \left( \frac{C_f^k}{C_f^{k+1}} \right)^{1/3} \left( \frac{\sigma_T^k}{\sigma_T^{k+1}} \right)^{1/3} \quad (2.17)$$

$$\frac{\tau_*^{k+1}}{\tau_*^k} = \left( \frac{C_f^k}{C_f^{k+1}} \right)^{-1/3} \left( \frac{\sigma_T^k}{\sigma_T^{k+1}} \right)^{2/3} \quad (2.18)$$

$$\frac{d_s^{k+1}}{d_s^k} = \left( \frac{C_f^k}{C_f^{k+1}} \right)^{1/3} \left( \frac{\sigma_T^k}{\sigma_T^{k+1}} \right)^{1/3} \quad (2.19)$$

where  $\sigma_T$  is the river sinuosity, defined as the ratio of the dimensionless intrinsic length  $L = L^*/B_0^*$  (computed along the channel centerline) to the dimensionless Cartesian length  $l_x = l_x^*/B_0^*$  (obtained projecting the river axis on the longitudinal axis  $x$  oriented in the direction of the floodplain gradient).

## 2.3 Floodplain features

The model described so far has been found to effectively reproduce typical meander shapes observed in nature (simple bends, compound bends and multiple loops) for a constant (in time and space) floodplain erodibility (Frascati and Lanzoni, 2009). The bank erosion coefficient, however, generally depends on soil properties, deposition and consolidation processes, groundwater dynamics (Han and Endreny, 2014), and distribution of riparian vegetation (Perucca et al., 2007; Motta et al., 2012a,b; Wickert et al., 2013). To mimic these heterogeneities, the valley surface is, as a first approximation, schematized by three different geomorphic units with different local coefficients  $E$  (Figure 2.3), depending on the soil properties as well as on the vegetation cover.

The first geomorphic unit is the pristine floodplain, with coefficient  $E = E_f$ . It corresponds to the undisturbed floodplain consisting sediment deposited by repeated flooding events, not yet impacted and consequently reworked by the river migration.

The second geomorphic unit corresponds to the oxbow lake environment, with coefficient  $E = E_o$ . It mimics the fine-filled abandoned channel reach which leads to the formation of plugs that may obstruct the lateral migration of the active channel (Toonen et al., 2012). Finally, the third geomorphic unit corresponds to the scroll

bar environment, with coefficient  $E = E_b$ . It mimics the floodplain area bounded by an oxbow lake, characterized by the typical ridge-and-swale sequence. In particular, coarse-grained sediments typically accumulates on the ridge, while finer sediment (silt and clay) deposit in the upper part (Nanson, 1980) because of the temporary flow expansions (van De Lageweg et al., 2014). The structure of vegetation reflects the local topography and hydrological conditions (Zen et al., 2016) contributing to the erosional complexity of the scroll bodies.

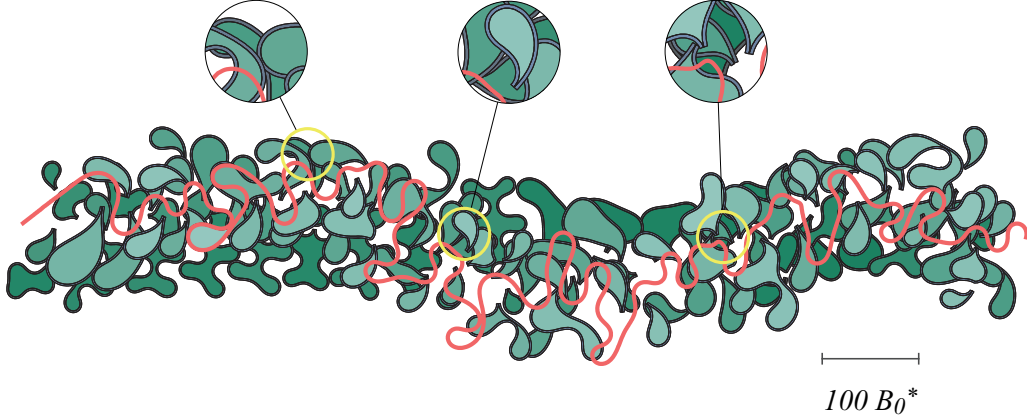


Figure 2.4: Example of a simulated planform dynamics, with the formation of scroll bars (older are dark green, younger are light green) and oxbow lakes (gray stripes bounding the previous elements, corresponding to the abandoned bends).

All the erosion coefficients are kept constant over time in order to maintain the modelling framework at the lowest possible level of complexity, thus temporal variations caused, e.g., by soil compaction and biological dynamics are not considered. Furthermore, incision, soil uplift, and subsidence are not accounted for, assuming that the floodplain surface is infinitely large and keeps its elevation constant over time. Possible changes in the hydrological regime and flow unsteadiness associated with flood waves are neglected as well.

Spatial variability ensuing from the meandering dynamics is accounted for as follows. All the progressively formed geomorphic environments (oxbow lakes and scroll bars) are saved as polygons given by the abandoned mesh nodes (Figure 2.4). As the generic node  $P_i$  of the active channel axis migrates laterally, the river may encounter three different environments during its lateral migration onto the valley. The winding number

algorithm of Hormann and Agathos (2001) is used to identify whether the current point lies within a pre-saved geomorphic unit and, hence, to choose the appropriate local erosion coefficient.

## 2.4 The flow field

This section briefly summarizes the key points of two mathematical models of channel morphodynamics adopted in this work, namely the model developed by Ikeda et al. (1981), hereafter referred to as IPS model, and the model developed by Zolezzi and Seminara (2001), hereafter referred to as ZS, similarly to the approach of Frascati (2009). Both models are based on the assumption of a secondary bidimensional flow driven by the curvature distribution and superimposed to the primary uniform flow travelling the channel.

The use of two models entailing a different level of approximation is motivated by the importance that the coupling of the flow field and the sediment balance equations has on the quantitative reproduction of observed river planforms. The former model however, assumes empirically the form of the channel cross-section.

The IPS model has been widely used (see, among the others, Perucca et al., 2005; Güneralp and Rhoads, 2011; Schuurman et al., 2016). The decoupling of the equations governing the flow field and the sediment conservation does not allow to solve for the bed configuration, thus an empirical relation is required. The dimensionless excess near-bank velocity  $U_b$  takes the type:

$$U_b = U_0^* F \left[ \nu_0, \beta, C_f, \tau_*, \mathcal{C}, \int_0^s \mathcal{C}(\xi) e^{\lambda_0(s-\xi)} d\xi \right] \quad (2.20)$$

where the characteristic exponent  $\lambda_0 = -2\beta C_f$  drives the convolution integral which accounts for the effect of the upstream curvature distribution on the downstream reach (downstream influence).

The ZS morphodynamic model solves the steady flow field in a movable bed river with variable curvature of the channel axis. It was derived by integrating over the depth the continuity equation and the Reynolds-averaged Navier-Stokes equations (RANS), written in intrinsic coordinates, and by introducing a parametrization of the secondary flow driven by the channel axis curvature (Zolezzi and Seminara, 2001). The extension of the model to cases involving width variations was developed by Frascati and Lanzoni

(2013). The resulting equations are fully coupled to the Exner sediment balance equation, also written in curvilinear coordinates, and closed by means of a suitable sediment transport law. All the relevant equations are then linearized, by expanding in terms of small parameters, taking advantage of the typically wide character of river bends (small curvature ratio  $\nu_0$ ). Eventually, the following functional relationship is found:

$$U_b = U_0^* F \left[ \nu_0, \beta, C_f, \tau_*, \mathcal{C}, \int_0^s \mathcal{C}(\xi) e^{\lambda_{mj}(s-\xi)} d\xi \right] \quad (2.21)$$

where  $\lambda_{mj}$  ( $m = 0, \infty; j = 1, 4$ ) are characteristic exponents for the  $m$ th lateral Fourier mode which are crucial to determine, through the related convolution integrals, whether flow and bed topography at a given position  $s$  are affected by the river reach located upstream (downstream influence) or downstream (upstream influence) (Zolezzi and Seminara, 2001; Lanzoni and Seminara, 2006). The four exponents are the solutions of the four-order ordinary differential equation that arises from the linearized continuity and momentum equations coupled with the sediment balance equation. Chapter 5 will show how these solutions can be particularized to satisfy internal boundary conditions. Figure 2.5 shows three examples of the trends followed by the characteristic exponents  $\lambda_{mj}$  as functions of the values of the half width to depth ratio  $\beta$ , compared with the behaviour of the characteristic exponent  $\lambda_0$  resulting from the IPS approach. It is worthwhile to note that, generally,  $\lambda_{m1}$  is real positive,  $\lambda_{m4}$  is real negative. They describe non-oscillatory spatial perturbations which decay fairly fast either downstream or upstream. The other two exponents  $\lambda_{m2}$  and  $\lambda_{m3}$  are complex conjugate, having respectively equal real parts ( $\lambda_{m2r} = \lambda_{m3r}$ ) and opposite imaginary parts  $\lambda_{m2i} = -\lambda_{m3i}$ . They describe oscillatory spatial perturbations which decay fairly slowly, spreading their influence over a considerable channel length (Lanzoni et al., 2006). Moreover,  $\lambda_{m3r}$  can be negative or positive, depending whether the aspect ratio  $\beta$  is smaller or larger than a threshold value,  $\beta_r$ . Channels characterized by aspect ratios  $\beta < \beta_r$  are defined subresonant, leading to a downstream influence, as in the IPS model. On the contrary, channels characterized by aspect ratios  $\beta > \beta_r$  are defined superresonant, leading to an upstream influence. This latter condition can not emerge when using the IPS model, as the latter is driven by a first-order ordinary differential equation because of the uncoupling of the sediment balance equation and the flow field. Subresonant meanders are typically upstream skewed and migrate downstream, while superresonant meanders are typically downstream skewed and migrate upstream (Lanzoni et al., 2006; Lanzoni and Seminara, 2006).

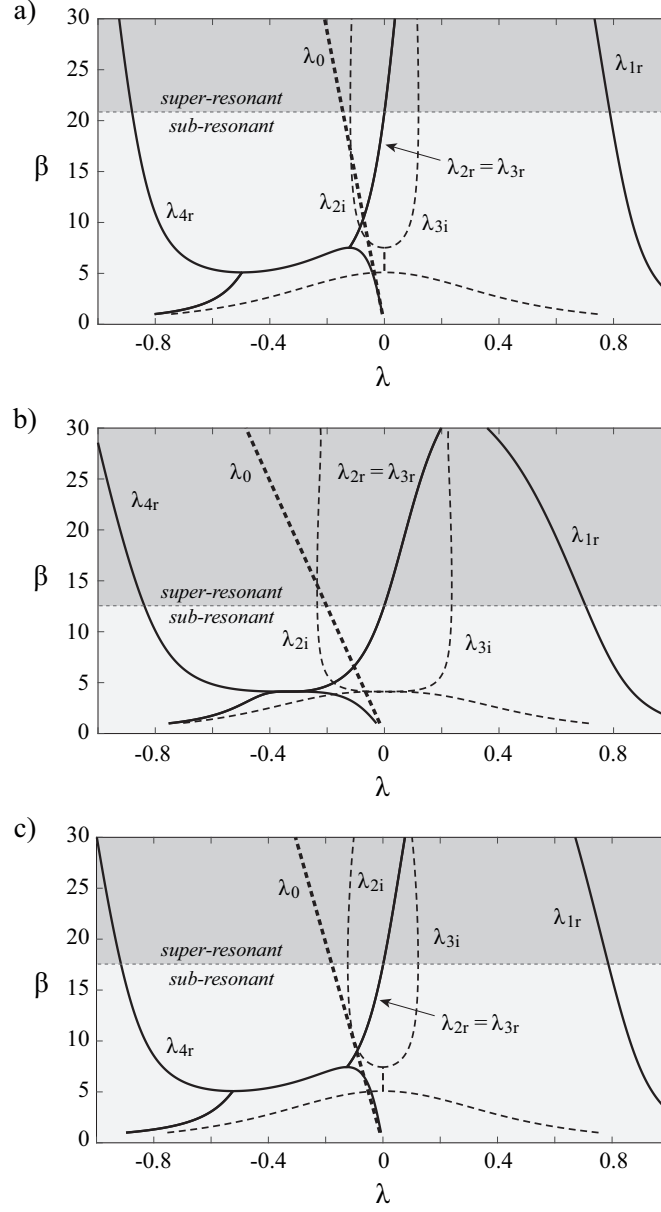


Figure 2.5: Typical behaviour of the four characteristic exponents  $\lambda_{mj}$  of the ZS approach as a function of the half width to depth ratio  $\beta$ , for three different scenarios. Continuous lines correspond to the real parts, dashed thin lines correspond to the imaginary parts, while the dashed thick line corresponds to the characteristic exponent  $\lambda_0$  of the IPS approach. The three scenarios are characterized by the following parameter sets: a)  $\tau_* = 0.1$ ,  $d_s = 0.005$ , flat bed; b)  $\tau_* = 0.3$ ,  $d_s = 0.001$ , dune-covered bed; c)  $\tau_* = 0.6$ ,  $d_s = 0.0001$ , dune-covered bed.



Further details about the derivation, performances, and limitations inherent in linearization of the flow field model may be found in Zolezzi and Seminara (2001) and Frascati and Lanzoni (2013).

In order to increase the computational efficiency in the numerical implementation, the convolution integrals appearing in the expressions for the velocity perturbation (2.20) and (2.21) are evaluated using Simpson rule, truncating the integration when the function to be integrated, that decays exponentially, is smaller than a given tolerance, say  $10^{-4}$  (Lanzoni and Seminara, 2006).



## Chapter 3

# Statistical tools

Three different statistical and spectral methodologies will be used in this thesis to analyse objectively the similarities/differences between the river planforms, namely the Fourier Analysis (FA), the Singular Spectrum Analysis (SSA), its multivariate version Multivariate Singular Spectrum Analysis (MSSA), and the Principal Component Analysis (PCA).

### 3.1 Fourier Analysis

The Fourier Analysis (FA) is a linear technique that has been widely adopted in the study of meandering planforms (Marani et al., 2002; Güneralp and Rhoads, 2011; Motta et al., 2012b). The considered time- or space-based discrete signal  $\mathbf{X}$ , formed by  $N$  equidistant samples with interval  $= 1/f_k$  (with  $f_k$  the sampling frequency), is processed using the Discrete Fourier Transform (DFT) to obtain an equivalent signal  $\mathbf{Y}$  in the domain of frequencies or wavenumbers. The  $k$ th component of the resulting vector  $\mathbf{Y}$  reads:

$$Y_k = \sum_{n=0}^{N-1} X_n e^{-ik \frac{2\pi}{N} n} \quad (3.1)$$

where  $k$  ranges from 0 to  $N - 1$ ,  $i$  is the imaginary unit. The absolute value of  $Y_k$  measures the total amount of information contained at the given frequency  $k$ . The whole distribution of absolute values of  $\mathbf{Y}$  is called power spectrum, and is used to identify the most important components, i.e., the modes or trigonometric basis functions that mostly contribute to the reproduction of the overall signal. The power spectrum is used to compare the spatial signals of the meander curvatures, both numerically generated

and observed, on the same number of modes, in order to disclose the possible affinities of their respective structure.

### 3.2 Singular Spectrum Analysis

Singular Spectrum Analysis (SSA) is a technique of time series analysis incorporating the elements of classical time series analysis, multivariate statistics, multivariate geometry, dynamical systems and signal processing. In particular, SSA gives adaptive filters associated with the dominant oscillations of the system, clarifying the characteristics of the possible noise affecting the data (Vautard and Ghil, 1989). The numerical procedure is here summarized, basing on Ghil et al. (2002). The starting point is to embed a time (space) series  $X_i$ , ( $i = 1, N$ ) into a vector space of dimension  $M$ . This corresponds to represent the behaviour of the data set by a succession of overlapping views through a sliding  $M$ -point window. The embedding procedure thus builds a sequence  $\tilde{\mathbf{X}}_j$  of  $M$ -dimensional vectors from the original data series  $\mathbf{X}_i$ , by using lagged copies of the same data:

$$\tilde{\mathbf{X}}_j = [\mathbf{X}_j, \mathbf{X}_{j+1}, \dots, \mathbf{X}_{j+M+1}] \quad (3.2)$$

where  $j = 1, N'$ , and  $N' = N - M + 1$ .

The  $M \times M$  lag-covariance matrix  $\mathbf{C}_{\mathbf{X}}$  may be estimated directly from the data as a Toeplitz matrix with constant diagonals; that is, its entries depend only on the lag  $|m - n|$  (Vautard and Ghil, 1989). The generic entry of the covariance matrix reads:

$$c_{mn} = \frac{1}{N - |m - n|} \sum_{j=1}^{N-|m-n|} X_j X_{j+|m-n|} \quad (3.3)$$

Performing a Singular Value Decomposition (SVD) of  $\mathbf{C}_{\mathbf{X}}$  gives the  $M$  eigenvalues  $\lambda_k$ , taken in decreasing order of magnitude, and the corresponding eigenvectors  $\rho_k$  ( $k = 1, M$ ). Projecting the original time series onto each eigenvector yields the corresponding principal components (PCs):

$$A_{kj} = \sum_{l=1}^M X_{j+l-1} \rho_{k,l} \quad (3.4)$$

Finally, the  $k$ th reconstructed component (RC) associated with the direction  $\rho_k$  reads:

$$R_{ki} = \frac{1}{M_i} \sum_{l=L_t}^{U_t} A_{k,i-l+1} \rho_{k,l} \quad (3.5)$$

where  $M_t$ ,  $L_t$ , and  $U_t$  differ between the central part of the signal and its end points:

$$(M_t, L_t, U_t) = \begin{cases} \left(\frac{1}{i}, 1, i\right) & \text{if } i \leq M - 1 \\ \left(\frac{1}{M}, 1, M\right) & \text{if } M \leq i \leq N' \\ \left(\frac{1}{N - i + 1}, i - N + M, M\right) & \text{if } i \geq N' + 1 \end{cases} \quad (3.6)$$

No information is lost in the reconstruction process, since the sum of all individual RCs gives back the original signal. In particular, the RCs may be arbitrary superimposed to obtain the desired signal smoothing, without necessarily respecting their order based on the eigenvalues decreasing order. The choice of the window length  $M$  is based on a trade-off between the quantity of extracted information versus the degree of statistical confidence in that information. The former requires a window as wide as possible (large  $M$ ), whereas the latter requires as many repetitions of the features of interest as possible (large  $N/M$ ).

The eigenvalues of the covariance matrix provide the information needed to filter out the real signal from noise. The generic eigenvalue  $\lambda_k$  equals the partial variance in the direction  $\rho_k$ , and the sum of all  $\lambda_k$  gives the total variance of the original time series  $\mathbf{X}_i$ . The singular values (SV) are defined as the square roots of the eigenvalues,  $\lambda_k^{1/2}$ . The singular value spectrum leads to a possible separation between fundamental components of the inspected signal and higher-order noise, thus it is an indicator of the signal complexity due to its splitting along the  $M$  components. In particular, the faster the spectrum decays, the larger is the separation between the fundamental signals and noises, and thus the less is the signal scattering. On the contrary, the larger is the spectrum mildness, the higher is the signal complexity due to the possible weight of higher-order noise. The SSA is used in two different cases. In the first, the technique investigates the intrinsic structure of the temporal trend of three geometric parameters describing the meander shapes. In the second it is used to disclose the structure of the spatial signal of the meander curvature, as well the FA.

### 3.3 Multivariate Singular Spectrum Analysis

The Multivariate Singular Spectrum Analysis (MSSA) is an extension of SSA to a multivariate input signal composed by  $L$  channels. The algorithm follows the steps described above, slightly differing for the structure of the lag-covariance matrix  $\mathbf{C}_\mathbf{X}$ ,

which now assembles the local contributions of the component-based lag-covariance matrices in order to take into account the multi-dimensionality of the signal. As a consequence,  $\mathbf{C}_{\mathbf{X}}$  has dimensions  $LM \times LM$  and  $LM$  eigenvalues. The MSSA is used for inspecting the structure of both the temporal and the spatial trends of the meander geometry.

### 3.4 Principal Component Analysis

The Principal Component Analysis (PCA) is a technique already considered in the analysis of river planforms by Frascati and Lanzoni (2009). It may be used to reduce a large set of variables to a small set that still contains most of the information embedded in the original set. In particular, PCA performs a change in the reference system by converting a  $M$ -dimensional sample of data  $\mathbf{X}$ , possibly correlated among each others, in a set  $\mathbf{Y}$  of linearly uncorrelated data through an orthogonal transformation, based on the eigenvectors of the correlation matrix  $\mathbf{C}$ , if the variances of individual variates are very different. The generic element  $c_{ij}$  of the covariance matrix corresponds to the correlation between the  $i$ th and the  $j$ th components of the given input data sample  $\mathbf{X}$  having  $N$  samples and  $M$  components (i.e.,  $i$  and  $j$  ranges from 1 to  $M$ ). As a result, the correlation matrix  $\mathbf{C}$  has dimensions  $M \times M$  and is symmetric. The eigenvectors of  $\mathbf{C}$ , sorted following the descending order of the relative eigenvalues  $\lambda_k$  (being  $k = 1, \dots, M$ ), form an orthonormal basis on which the pristine data  $\mathbf{X}$  are projected to obtain a new set of data  $\mathbf{Y}$  having the same dimensions of  $\mathbf{X}$ .

The eigenvalues are associated with the measure of the total amount of variance information carried by the eigenvector directions. Data similarity can be then effectively evaluated by looking at the variance distribution (the eigenvalues) along the principal directions (the eigenvectors). This approach facilitates the identification of the differences that contribute the most to the formation of the deviations among signals coming from the various samples. As a consequence, the new data set  $\mathbf{Y}$  allows to reduce the dimensionality of the problem while retaining as much as possible of the variance information contained in the original data set  $\mathbf{X}$ .

In the present work, PCA was used for two different purposes. The first purpose is to normalize the data that will be used by the input to MSSA through the projection along the correlation eigenvectors. No dimensions are neglected after PCA with reference to the eigenvalue spectrum, i.e. the dataset keeps the initial dimensionality  $M$ . The

second is to carry out an overall comparison between natural planforms and numerically generated paths. In the latter case,  $\mathbf{X}$  is a  $N \times M$  matrix referring to  $N$  rivers coming from different databases, such that the  $i$ th row contains the  $M$  quantities related to the  $i$ th river path, either natural or synthetically generated.





## Chapter 4

# On the floodplain heterogeneity

This Chapter concerns the interaction between the long-term dynamics of a meandering river and its self-formed floodplains. Differently from Howard (1996) and Sun et al. (1996), a more refined mathematical approach is implemented to compute the curvature-driven flow field. The widely used IPS approach is used to highlight the intrinsic limitations of the planforms resulting from its application. The long-term changes in channel dynamics are strictly related to the structure of the evolving floodplain.

The aim of this part of the thesis is twofold: i) to evaluate the mutual interaction between a self-formed heterogeneous floodplain and the meandering river which flow above it, and ii) to propose a new suite of statistical tools and metrics to analyse objectively the spatial and temporal signals generated numerically and to use these tools to compare the modelled planforms against observed geomorphic features. An extensive database of numerically generated meander planforms was created, evolving in time up to a statistically-stationary evolving state by varying the relevant parameters within physically plausible ranges. Three different statistical tools were used to evaluate quantitatively the influence of the adopted mathematical models and their accuracy in reproducing natural planforms. In particular, Singular Spectrum Analysis (SSA) and its Multivariate extension (MSSA) were used to inspect the time structure of the numerically generated signals; Fourier analysis (FA), Principal Component Analysis (PCA) as well as SSA and MSSA were used to compare numerically generated planforms with those observed in a wide range of environmental conditions.

The remaining of this Chapter is organized as follows. Section 4.1 describes a test case comparing together the planforms generated by considering in terms of different

erodibility either three geomorphic units (pristine floodplain, oxbow lakes, and scroll bars) or only two different units (pristine floodplain and scroll bars) thus turning off of the effects of the third environment (the oxbow lakes). A set of numerical runs based on different self-formed heterogeneity scenarios (Section 4.2) is then analysed with reference to their time evolution (Section 4.3). Section 4.4 compares numerically generated planforms with a set of natural planforms through the three different statistical and spectral tools mentioned above, namely the Fourier Analysis (FA), the Singular Spectrum Analysis (SSA), its Multivariate extension (MSSA), and the Principal Component Analysis (PCA). Finally, Section 4.5 discusses the effects on river dynamics of a self-formed floodplain having heterogeneous erodibility distribution.

#### 4.1 A test case: two vs. three erodibility environments

The test case considered in this section was designed to evaluate qualitatively the interactions between the long-term evolution of meanders and the floodplain heterogeneity formed by the river migration. The parameters were chosen arbitrarily.

The erosional coefficient of the pristine floodplain to be used in the migration law (2.11) was set equal to  $E = E_f = 10^{-8}$ . Referring to the sketch in Figure 2.3, six scenarios were investigated by accounting or excluding the effect of the oxbow lakes and considering three different erosional resistance  $E_b$  for the scroll bars, assumed to be either equal, larger (softening scenario), or smaller (hardening scenario) than that of the pristine floodplain. Since oxbow lakes in the long term are often filled by fine grained sediments forming less erodible plugs, they tend to contrast the river migration when the channel flows again through them. In order to maintain the lowest possible level of complexity, the oxbow lake infilling is assumed to occur instantaneous after the cutoff, and the erodibility coefficient  $E = E_o$  of the oxbow lake area is set equal to  $E_o/E_f = 1/10$ . Similarly, the scroll bar area bounded by the oxbow inner bank is assumed to switch instantaneously to the erodibility coefficient  $E_b$ .

Table 4.1 summarizes the six investigated scenarios.

The first case (hereafter referred to as HC) consists of a floodplain which, in term of erodibility, is not modified by the river evolution. In other words, the river has no memory about its own past configurations. As a consequence, all the three erosional resistances are equal  $E_f = E_o = E_b$ .

The second case (hereafter referred to as OO) considers the possible formation of

Table 4.1: Different scenarios considered for the erosional resistance of the various geomorphic units (i.e. pristine floodplain with erodibility  $E_f$ , oxbow lakes with erodibility  $E_o$ , and scroll bars with erodibility  $E_b$ ) used for the test case. The scenarios account for the presence of oxbow lakes which are less erodible than the surrounding floodplain, or exclude this effect assuming that the oxbow lakes are not distinguishable from the pristine floodplain. These two scenarios are then coupled with those assuming that the scroll bars are as erodible as the pristine floodplain (HC, OO), more erodible (SG, SGC) and less erodible (GS, GSC) than the pristine floodplain.

ID	oxbow lakes	$E_o/E_f$	scroll bars	$E_b/E_f$
HC	no	1	no	1
OO	yes	1/10	no	1
SG	no	1	softening	3
SGC	yes	1/10	softening	3
GS	no	1	hardening	1/3
GSC	yes	1/10	hardening	1/3

oxbow lakes having erosional resistance lower than the pristine floodplain. No scroll bar effects are accounted for ( $E_b = E_f$ ).

The third and the fourth cases (hereafter referred to as SG and SGC) concern the formation of scroll bars which are more erodible than the surrounding floodplain, such the river migration experiences a faster displacement throughout these areas. The erodibility coefficient is set equal to  $E_b/E_f = 3$ . These two scenarios might roughly correspond to a river which flows in a valley formed mainly by fine material and transports coarser sediment which is deposited on the inner bend point bars during floods. Thus, the effect that the coarser material layers have on the erodibility of the scroll bars dominates over the effect given by the fine layers. Alternatively, the SG and SGC scenarios may be assume to mime a river dynamics which is faster than the compaction of bar soil and the development of vegetation cover. Oxbow lakes may be excluded (SG),  $E_o = E_f$ , or included (SGC),  $E_o/E_f = 1/10$ .

The fifth and the sixth cases (hereafter referred to as GS and GSC) assume that scroll bars are less erodible than the surrounding floodplain, such the river migrates much slowly when it flows across these areas. The erodibility coefficient is set equal

to  $E_b/E_f = 1/3$ . These two scenarios might roughly correspond to a river which flows in a valley formed mainly by coarse sediment and deposits in prevalence fine sediment on the point bars. Thus, the effect on erodibility due to the finer layers of the scroll bars is stronger than that due to the coarser layers. Alternatively, the GS and GSC scenarios may mime the rapid formation of a vegetation cover that stabilizes the point bar. Again, oxbow lake effect may be excluded (GS),  $E_o = E_f$ , or included (GSC),  $E_o/E_f = 1/10$ .

All runs started from the same initial morphology consisting of a straight channel perturbed on the transverse direction with small random fluctuation normally distributed (with zero mean and standard deviation equal to  $0.01 \times B_0^*$ )

The initial dimensionless parameters in this test case are  $\beta = 20$ ,  $\tau^* = 0.7$ ,  $d_s = 0.0005$ ,  $R_p = 400$ , which correspond to  $2B_0^* = 175$  m,  $D_0^* = 4.30$  m,  $S = 5.8 \times 10^{-4}$ , and  $d_s^* = 2.1$  mm (i.e. coarse sand). Assuming a Strickler coefficient equal to  $K_s = 25$  m<sup>1/3</sup> s<sup>-1</sup>, the uniform flow velocity, the discharge and the Froude number read, respectively:

$$U_0^* = K_s D_0^{*2/3} S^{1/2} = 1.59 \text{ m/s} \quad (4.1a)$$

$$Q = 2B_0^* D_0^* U_0^* = 1190 \text{ m}^3/\text{s} \quad (4.1b)$$

$$Fr = \frac{U}{\sqrt{gD_0}} = 0.245 \quad (4.1c)$$

According to Latrubesse (2008), the considered river may be classified as a *large river*, being the discharge larger than 1000 m<sup>3</sup>/s. Several approaches have been provided in the literature to discriminate channel patterns. The discharge/slope approaches of Leopold and Wolman (1957) and Lane (1957) provide respectively  $S_{lim} = 5.8 \times 10^{-4}$  and  $S_{lim} = 1.2 \times 10^{-3}$  as threshold to discriminate between braided rivers ( $S > S_{lim}$ ) and meandering rivers ( $S < S_{lim}$ ). According to the former classification, the considered test case falls on the braided-meandering threshold, whereas it is largely in the meander domain when considering the latter classification. The approach of Parker (1976) relates the threshold slope to the Froude number, giving  $S_{lim} = 6.1 \times 10^{-3}$ . Recent approaches have been based on the stream power, which reads:

$$\omega = \frac{\gamma Q S}{2B_0^*} = 39 \text{ W/m}^2 \quad (4.2)$$

Combining the empiric formulas of Van den Berg (1995) and of Makaske et al. (2002) gives the threshold between braiding and meandering (denoted as  $\omega^{VDB}$ ) and the threshold between meandering and lateral stillness (denoted as  $\omega^{MAK}$ ) in function of

the mean grain size (Kleinhans and van den Berg, 2011). Applying the coupled approaches to the current test case confirms that the river likely lies in the domain of meandering rivers:

$$\omega_{MAK} = 7 \text{ W/m}^2 < \omega = 39 \text{ W/m}^2 < \omega_{VDB} = 68 \text{ W/m}^2 \quad (4.3)$$

Kleinhans and van den Berg (2011) proposed a new empirical relation to split the meandering domain into two subdomains, namely meandering with scroll occurrence and meandering with braiding and chute occurrence. The dataset used to develop such classification is mainly focused on large grain diameters (most of them ranges between 3 and 8 cm thus referring to rough gravel rivers), with few data about sand and, in general, fine sediment. As a consequence the classification criterion law might not be able to describe all the scenarios typical of large alluvial rivers.

The six simulations listed in Table 4.1 were run by using the ZS mathematical approach in order to compute the excess near-bank velocity.

Figure 4.1 shows the simulated migration history for the six different erodibility scenarios, after a scaled time equal to 20 times the time  $t_{fc}$  at which the first cutoff occurs. Scenarios characterized by the formation of oxbow lakes and scroll bars harder than the pristine floodplains (OO, SGC, GS, and GSC) show that the river migration influences a floodplain region of width of about  $100 B_0^*$  that exhibits a sinuous spatial trend. On the other hand, the remaining two scenarios (the homogeneous case, HC, and the softening scenario without oxbow lakes, SG) are characterized by a migration area that is nearly straight and has a width of about  $200 B_0^*$ .

In order to characterize quantitatively the simulated landforms, a suite of three geometric parameters, referred to the half meander metrics (i.e., related to reaches defined by two consecutive inflection points of the channel axis), are used here (Howard and Hemberger, 1991; Frascati and Lanzoni, 2009). They are the half meander length  $L_h$ , the half meander sinuosity  $\sigma_h$ , and the half meander asymmetry  $A_h$ . The first corresponds to the intrinsic distance between two planimetric inflection points, while the latter two are defined as follows:

$$\sigma_h = \frac{L_h}{l_h} \quad (4.4a)$$

$$A_h = \frac{L_h^u - L_h^d}{L_h} \quad (4.4b)$$

where  $l_h$  is the Cartesian length between two inflection points, while  $L_h^u$  and  $L_h^d$  are

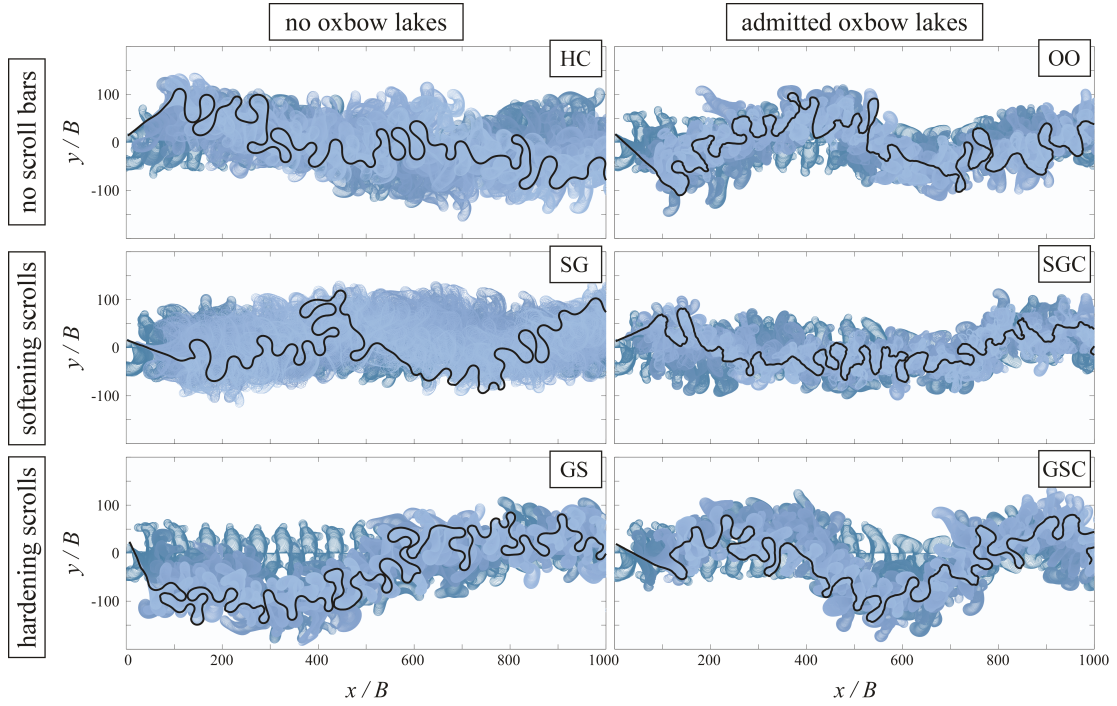


Figure 4.1: Migration history of the river planforms, simulated using the ZS approach and starting from a straight path slightly perturbed in the transverse direction. The initial dimensionless parameters read  $\beta = 20$ ,  $\tau^* = 0.7$ ,  $d_s = 0.0005$ . Darker paths are older, while lighter paths are younger. Left panels refer to runs carried out by assuming oxbow lakes as erodible as the surrounding floodplain; right panels refer to runs affected by the formation of oxbow lake less erodible than the surrounding floodplain. Row panels describe the effects of the scroll bar erodibility: in the upper panels the scroll bars are assumed as erodible as the surrounding floodplain; in the central panels the scroll bars are more erodible than the pristine floodplain (softening behaviour); in the lower panels the scroll bars are less erodible than the pristine floodplain (hardening behaviour).

the intrinsic lengths of the channel axis upstream and downstream of the point of maximum curvature  $\mathcal{C}_{\max}$  along the considered half meander. Note that  $A_h$  ranges in the interval  $(-1, 1)$  and determines whether the half meander is upstream skewed ( $A_h < 0$ ), downstream skewed ( $A_h > 0$ ), or symmetric ( $A_h = 0$ ). The metrics are averaged over the  $N_h$  half meanders forming the river path at time  $t$ . The temporal trends of these mean values are plotted in Figure 4.2.

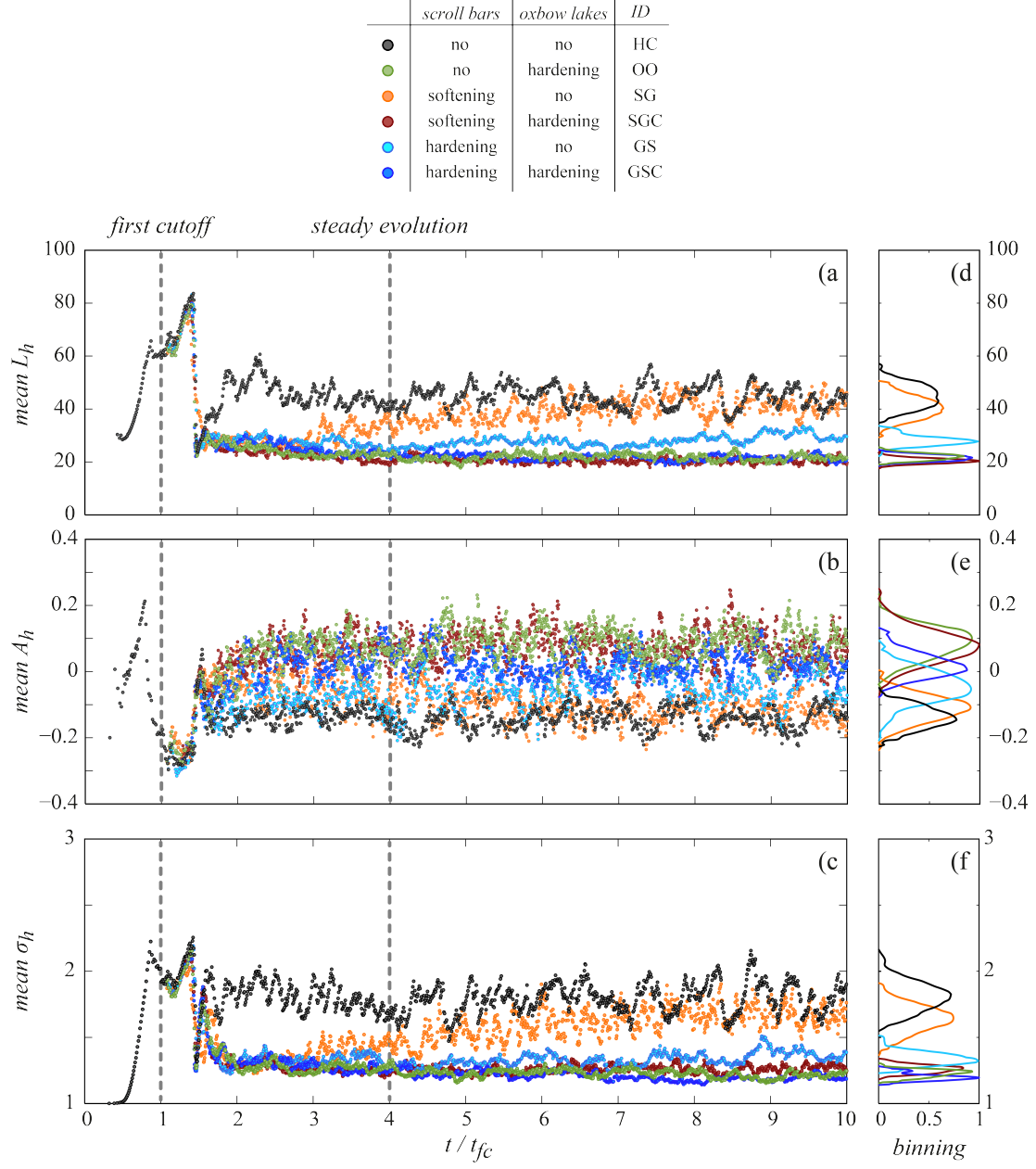


Figure 4.2: See caption at next page.

Figure 4.2: Time evolution of (a) the half meander length  $L_h$ , (b) asymmetry  $A_h$ , and (c) sinuosity  $\sigma_h$ , averaged over the river reach at each time step. Simulations were carried out by means of the ZS flow field model and by considering the six different erodibility scenarios listed in the Table 4.1. Dashed vertical lines correspond to the time  $t_{fc}$  of first cutoff occurrence and to the time  $t_{se}$  at which the planform evolution can be considered statistically stationary. The time interval  $t/t_{fc} < 1$  is characterized by growing meanders starting from an initial, slightly perturbed, straight path. The intermediate time interval  $1 < t/t_{fc} < 4$  represents a phase in which cutoffs start their filtering action, removing older bends and possibly changing the floodplain structure through the formation of oxbow lakes and scroll bars. Later on ( $t/t_{fc} > 4$ ) the planform configurations attain a statistically stationary evolution, for which the normalized frequency distributions of the observed quantities were computed (d, e, and f panels).

The river begins initially to elongate monotonically ( $t < t_{fc}$ , where  $t_{fc}$  is the time of occurrence of the first cutoff), and the floodplain area reworked by the channel migration increases as well. The initial condition (straight, slightly perturbed channel) leads to an artificial regularity of the meander trains which implies that adjacent meanders approach neck cutoffs nearly simultaneously (Frascati and Lanzoni, 2010). The second phase, starting after the first cutoff occurrence ( $t > t_{fc}$ ) shows that the possible heterogeneity introduced by the formation of oxbow lakes and point bars begins to affect the meander evolution process, as the trajectory referred to the homogeneous case (HC) strongly separates from the others affected by any floodplain heterogeneity. The separation is more remarkable in the trends of  $L_h$  and  $\sigma_h$ . At a later stage of evolution ( $t > t_{se}$ ) cutoffs remove older meanders limiting the planform geometrical complexity and leading to a statistical stationary evolution state, i.e. to time signals that oscillate about nearly constant values. This condition is attained at  $t/t_{fc}$  ranging from  $\sim 2$  for the active oxbow case to  $\sim 4$  for the SG case, thus this latter value will be considered as the starting time of stationary evolution conditions for all the scenarios. The stationary-evolving signals of  $L_h$  and  $\sigma_h$  referred to the three scenarios with active oxbow lakes (i.e. OO, SGC, GSC) are nearly superimposed, as shown by the frequency distributions. In the case of  $A_h$ , the GSC signal differs from the OO and SGC signals. In general, the presence of less erodible oxbow lakes leads to meanders which are on



average shorter and downstream skewed (i.e. positive  $A_h$ ), whereas by excluding this effect leads to upstream skewed meanders, as often observed in nature (Seminara et al., 2001). From a modelling point of view, considering the oxbow lakes less erodible rules out the effects of scroll bar units and, hence, the processes acting on them (e.g. sedimentary processes, vegetation dynamics). On the other hand, the trends of the GS signals are very close to OO, SGC and GSC signals. Thus, considering only hardening scroll bars without any oxbow lake effect could be assumed representative of generally hardening structures. Under statistically steady conditions the trends of the SG signals are close to the trends of the homogeneous cases, HC, despite the differences observed during the initial and intermediate evolution phases.

## 4.2 A synthetic database of meanders

A numerically generated database was built to cover a relatively wide range of natural-equivalent cases by considering 18 sets of initial parameters, namely  $\beta$ ,  $\tau^*$ ,  $d_s$ , and bed type (Table 4.2). Simulations were carried out using both the ZS and the IPS flow field models described in Chapter 2. All the runs started from a common initial morphology consisting of a straight channel perturbed in the transverse direction with small random fluctuations normally distributed (zero mean and standard deviation equal to 0.01).

Recalling the results of the test case described in Section 4.1:

- introducing different sets of floodplain heterogeneities formed by the river migration leads to different planform shapes both in space and in time;
- the scenario with hardening scroll bars can approximate the behaviour emerging when considering less erodible oxbow lakes.

For these reasons, and in order to limit the number of simulations, only the effect of the scroll bars is accounted for. The abandoned channel reaches were thus split in two regions delimited by the channel axis. The inner part was considered as belonging to the scroll bar because of aggradation, whereas the outer half part was considered as belonging to the surrounding floodplain. As a consequence, only three different erodibility scenarios were considered, concerning the scroll bar erodibility coefficient  $E_b$ . The first scenario, hereafter denoted as *hardening case*, prescribes that the scroll bar geomorphic units are less erodible than the pristine floodplain ( $E_b/E_f = 1/8$ ). This

Table 4.2: Sets of initial parameters used in the numerical simulations carried out by using the ZS and IPS models. Here,  $\beta$  is the half-width to depth ratio,  $\tau_*$  is the Shields number,  $d_s$  is the mean sediment size scaled by the flow depth, while initial bed configuration may be either plane or dune-covered. Moreover,  $\tau_{se} = t_{se}/t_{fc}$  is the time (scaled by the time of first cutoff occurrence) at which statistically-stationary conditions are attained. For a certain set of parameters, the largest value of  $\tau_{se}$  is considered with reference to the three erodibility scenarios here investigated.

run	$\beta$	$\tau_*$	$d_s$	bed type	$\tau_{se}^{ZS}$	$\tau_{se}^{IPS}$
1	10	0.2	0.001	dune-covered	40	10
2	10	0.2	0.01	dune-covered	5	20
3	10	0.7	0.01	plane	2.5	5
4	10	1.2	0.01	plane	4	10
5	15	0.2	0.0001	dune-covered	13	5
6	15	0.2	0.001	dune-covered	10	10
7	15	0.2	0.01	dune-covered	4	50
8	15	0.7	0.001	plane	2	2
9	15	0.7	0.01	plane	4	5
10	15	1.2	0.01	plane	2	10
11	20	0.2	0.0001	dune-covered	3	10
12	20	0.2	0.001	dune-covered	5	30
13	20	0.2	0.01	dune-covered	4	50
14	20	0.7	0.0001	plane	3	2
15	20	0.7	0.001	plane	2	3
16	20	0.7	0.01	plane	1.5	7.5
17	20	1.2	0.001	plane	2	5
18	20	1.2	0.01	plane	1.5	20

occurrence describes the prevalence of fine-grained sediment in the point bar deposits (Rowland et al., 2005). The second scenario, hereafter denoted as *homogeneous case*, consists of preserved geomorphic units that have an erosion coefficient equal to that of the pristine floodplain ( $E_b = E_f$ ), so that the river dynamics does not introduce any variation in the floodplain sedimentary structure. Finally, the third scenario, hereafter denoted as *softening case*, considers the scroll bars more erodible than the pristine floodplain ( $E_b/E_f = 8$ ), such that the lateral migration rate of the river increases when a heterogeneous environment is reworked. Differently from the test case in Section 4.1, the differences between  $E_f$  and  $E_b$  were increased to emphasize the heterogeneity effects. The three different scenarios allow to understand how intrinsic features of river planforms may vary, in order to evaluate the mutual interactions between the long-term evolution (i.e. tens-hundreds of years) of meanders and the floodplain self-formed heterogeneity.

For each simulation, the time  $t_{se}$  at which the computed planforms attained statistically stationary evolving features was determined through the trends of the three geometric quantities  $L_h$ ,  $\sigma_h$ , and  $A_h$  introduced in Section 4.1, and scaled by the time  $t_{fc}$  at which the first cutoff occurs. Table 4.2 summarizes the values of  $\tau_{se} = t_{se}/t_{fc}$  found for the 18 sets of initial parameters, for both the ZS and the IPS approaches. In fact, given an initial set of parameters, the different flow fields determined by either the ZS or the IPS models provide different migration histories, yielding different characteristic values for both  $t_{fc}$  and  $t_{se}$ . Total simulation time for all runs lasted at least twice  $t_{se}$  to ensure that the three morphometric parameters oscillate in time around a constant value, i.e. to arrive at statistically-stationary evolving planforms. It is noteworthy that the river attains the statistically-steady evolving conditions (i.e. the time  $t_{se}$ ) before having completely reworked the pristine floodplain.

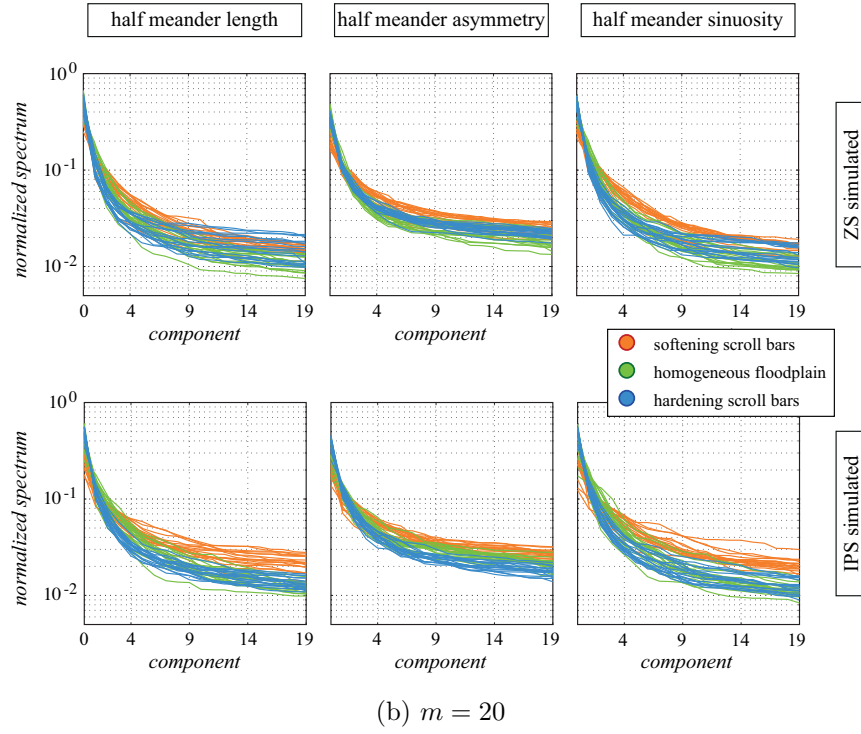
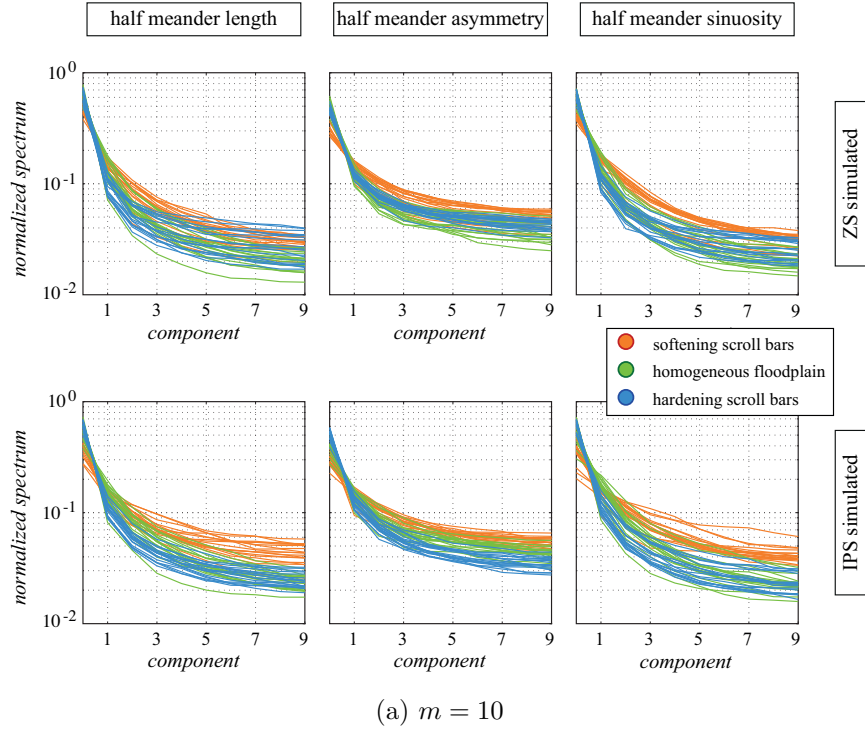
All the spectra analysed in the next sections were normalized to the total spectrum density.

### 4.3 Time analyses

Applying Singular Spectrum Analysis, SSA, and Multivariate Singular Spectrum Analysis, MSSA (see Chapter 3 for details), to the time series of the half meander metrics may help to disclose the structure and the degree of complexity embedded in the river planforms after the statistically-stationary evolving phase is attained. The various met-

rics are averaged over the entire river reach.

Figure 4.3 shows the SSA spectra computed for  $L_h$ ,  $A_h$ , and  $\sigma_h$  for three different window length, i.e.  $m = 10, 20$ , and  $30$ . In all cases, a slow decay of the Singular Values (SVs) is evident, showing that a large number of Reconstructed Components (RCs), is necessary to reproduce the signal. However, the different spectra have similar shapes and values across the tested metrics and simulated scenarios. The spectra concerning  $L_h$  and  $\sigma_h$  show a slightly larger variability of the tails and, hence, of the related noise. The fundamental SVs (related to the larger eigenvalues) for the hardening and the homogeneous cases are invariably above those of the softening case which, in turn, tends to exhibit higher-order noise components (i.e. the signals are above the others for smaller eigenvalues), distinctive of more complex signals. On average, IPS-generated channel paths show stacks better defined, whereas ZS-generated planforms exhibit almost overlapping  $L_h$  and  $\sigma_h$  stacks for the hardening and the homogeneous scenario. In addition, when adopting the ZS flow field model, the  $A_h$  spectra for the hardening case fall between those concerning the softening cases (which are above) and those concerning the homogeneous cases (which are below). On the contrary, a different trend is observed for the IPS-generated planforms; the homogeneous-case spectra, in fact, lie between the softening and the hardening spectra.



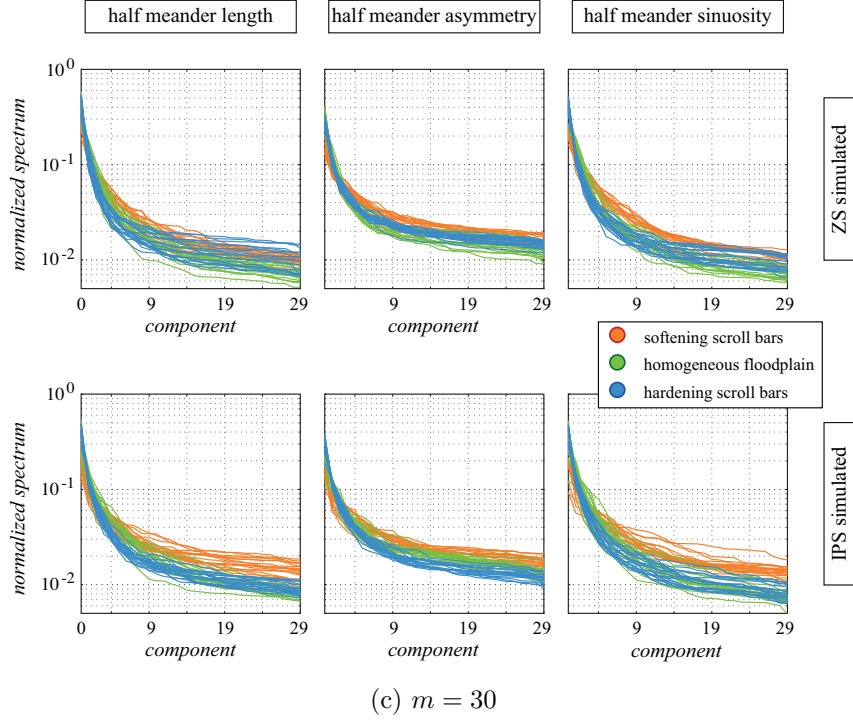


Figure 4.3: Normalized SSA spectra of half meander length  $L_h$ , half meander asymmetry  $A_h$ , and half meander sinuosity  $\sigma_h$ , averaged over the entire river reach at each time step and compared over the three different heterogeneity scenarios. The adopted window sizes are  $m = 10$  (a),  $m = 20$  (b), and  $m = 30$  (c). The time series refer to statistically-stationary evolving meander planforms. The upper panels refers to ZS flow field simulations, the lower to IPS flow field simulations.

MSSA was performed by considering, for each simulation, the time series of  $L_h$ ,  $A_h$ , and  $\sigma_h$  as a multi-dimensional signal. This three-component signal was previously normalized by PCA (see Chapter 3). The resulting spectra (Figure 4.4) show characteristics that are very similar to the corresponding SSA spectra. The largest SVs of the hardening case spectra are above, whereas the softening case spectra move to the top when considering higher-order SVs. The spectra obtained with the ZS model are almost overlapped for the hardening and the homogeneous scenarios, whereas the stacks referring to the softening case have more defined boundaries. On the other hand, the IPS model leads to a much clearer separation of the spectra for the intermediate components, while the tails tends to overlap, as for the ZS-generated series.

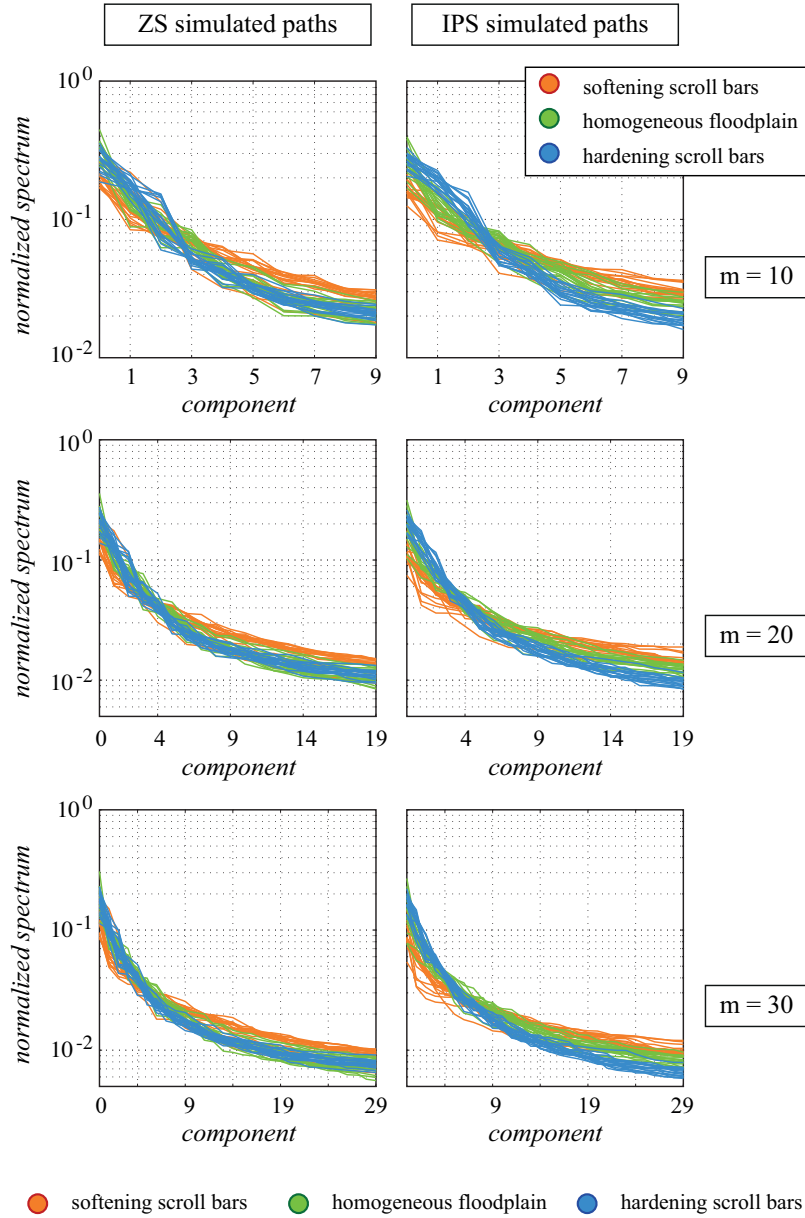


Figure 4.4: Normalized MSSA spectra of half meander multi-channel signal, composed by the length  $L_h$ , the asymmetry  $A_h$ , and the sinuosity  $\sigma_h$ , averaged over the entire reach at each time step and compared over the three different heterogeneity scenarios. The three-channel signals were previously normalized through PCA. Three different window sizes were adopted:  $m = 10$  (upper panels),  $m = 20$  (central panels), and  $m = 30$  (lower panels). The time series refer to statistically-stationary evolving meander planforms. Left panels refer to ZS flow field simulations, while right panels refer to IPS flow field simulations.

## 4.4 Spatial analyses

At the present, no general methods are available to analyse nonlinear spatio-temporal patterns (Frascati and Lanzoni, 2010). Expedients may be resorting to either spatial patterns, such as series of local curvatures (Perucca et al., 2005), or quantities which try to synthesize the overall behaviour of the system. Here the multivariate approaches followed by Howard and Hemberger (1991) and Frascati and Lanzoni (2009) is employed, in order to analyse spatial series of different metrics of meandering planforms through Fourier Analysis (FA), Singular Spectrum Analysis (SSA) and the Multivariate extension (MSSA), and Principal Component Analysis (PCA) (see Chapter 3). To this aim, three different databases were considered.

The first database consists of 52 natural planforms of meandering rivers, obtained from literature data or extracted from Landsat or Google Maps images (Table 4.3), and selected in order to include paths from different continents and environments.

Table 4.3: Database of natural river paths used for the multivariate statistical comparisons with numerically generated meanders. Data sources are as follows: 1, <http://earthexplorer.usgs.gov>; 1, <http://maps.google.com>; 2, Lancaster and Bras (2002); 3, Latrubesse (2008); 4, Stølum (1998).

River	Location	Data source
Beaver	Canada	2, 5
Birch Creek	Alaska, US	3
Chet	Russia	2
Chinchaga	Canada	2
Chulym	Russia	1
Curuca 1	Brazil	1
Curuca 2	Brazil	1
Darling	Australia	2
Dishna	Alaska, US	3
Dulgalakh	Russia	1
Envira	Brazil	1
Fly	Papua New Guinea	1, 5
Javari	Brazil, Peru	1

*River list continues on next page*



*River list continues from previous page*

River	Location	Data source
Jurua 1	Brazil	1, 4, 5
Jurua 2	Brazil	1, 4, 5
Jurua 3	Brazil	1, 4, 5
Kemchug 1	Russia	1
Kemchug 2	Russia	1
Kwango 1	Angola, Congo	1, 5
Kwango 2	Angola, Congo	1, 5
Kipo-Kulary	Russia	1
Melozitna	Alaska, US	3
Mississippi 1	US	1
Mississippi 2	US	1
Murray 1	Australia	1
Murray 2	Australia	1
Murray 3	Australia	1
North Fork Kuskokwim 1	Alaska, US	1
North Fork Kuskokwim 2	Alaska, US	1
Nan	Thailandia	5
Okavango	Angola	2
Orthon	Bolivia	2
Porcupine	Alaska, US	1
Preacher	Alaska, US	3
Purus 1	Brazil	1, 5
Purus 2	Brazil	1, 5
Ramu	Papua New Guinea	1
Rio Bravo	Mexico, US	2
Rio Madre De Dios	Peru	1
Sittang	Myanmar	2
Takotna	Alaska, US	3
Tarauaca 1	Brazil	1
Tarauaca 2	Brazil	1

*River list continues on next page*

*River list continues from previous page*

River	Location	Data source
Tarauaca 3	Brazil	1
Teklanika	Alaska, US	3
Tym 1	Russia	1
Tym 2	Russia	1
Tym 3	Russia	1
Tym 4	Russia	1
Tym 5	Russia	1
Vakh	Russia	1
Yana	Russia	1

*End of river list*

The second database groups the 18 ZS-generated configurations corresponding to the 3 scenarios assumed for the erosional resistance of the scroll bar environments (hardening, homogeneous, and softening). Thus it consists of  $18 \times 3$  planforms extracted randomly from the statistically-stationary configurations resulting from the runs listed in Table 4.2. Similarly, the third database concerns the IPS-generated paths ( $18 \times 3$ ).

Four groups of post-processing analyses were performed on these databases: binning and MSSA of half meander metrics, FA and SSA of full meander curvature, and a PCA which aims to globally compare the different planforms (i.e. natural or numerically generated) through a suite of statistical parameters describing the spatial distribution of the geometrical features.

### Half meander metrics

Figure 4.5 shows the binning of the three half meander metrics, either  $L_h$ ,  $A_h$ , and  $\sigma_h$ , computed for the various channel paths, natural or synthetic. Means and standard deviations of the binned values are reported in figure 4.6

The frequency of  $L_h$  in natural rivers decreases with the increasing values, with the maximum close to 100 (times  $B_o^*$ ). A similar trend is shown by ZS-generated paths related to the hardening scenario, even if some values are larger than 100. The softening and the homogeneous ZS planforms are characterized by more scattered binned values

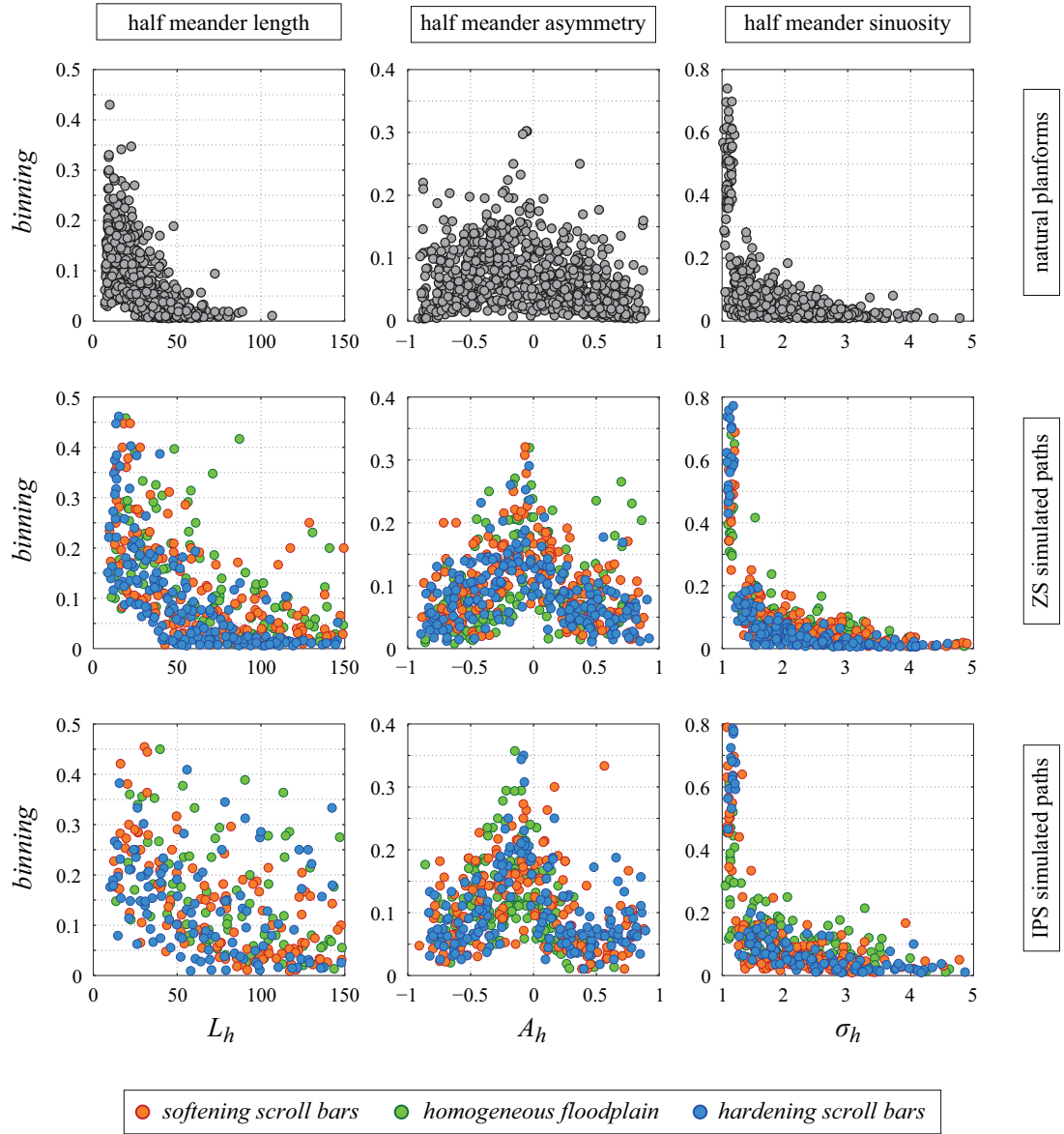


Figure 4.5: Binning of the spatial series of the three half meander metrics: the length  $L_h$  (left panels), the asymmetry  $A_h$  (central panels), and the sinuosity  $\sigma_h$  (right panels). The first row (gray markers) refers to the natural planforms, while the second and the third rows (coloured markers) refer to the ZS-simulated paths and to the IPS-simulated paths, respectively. The plot of  $L_h$  for the IPS simulations (bottom left) shows a lower number of points because some values exceed the maximum limit of the  $x$ -axis.

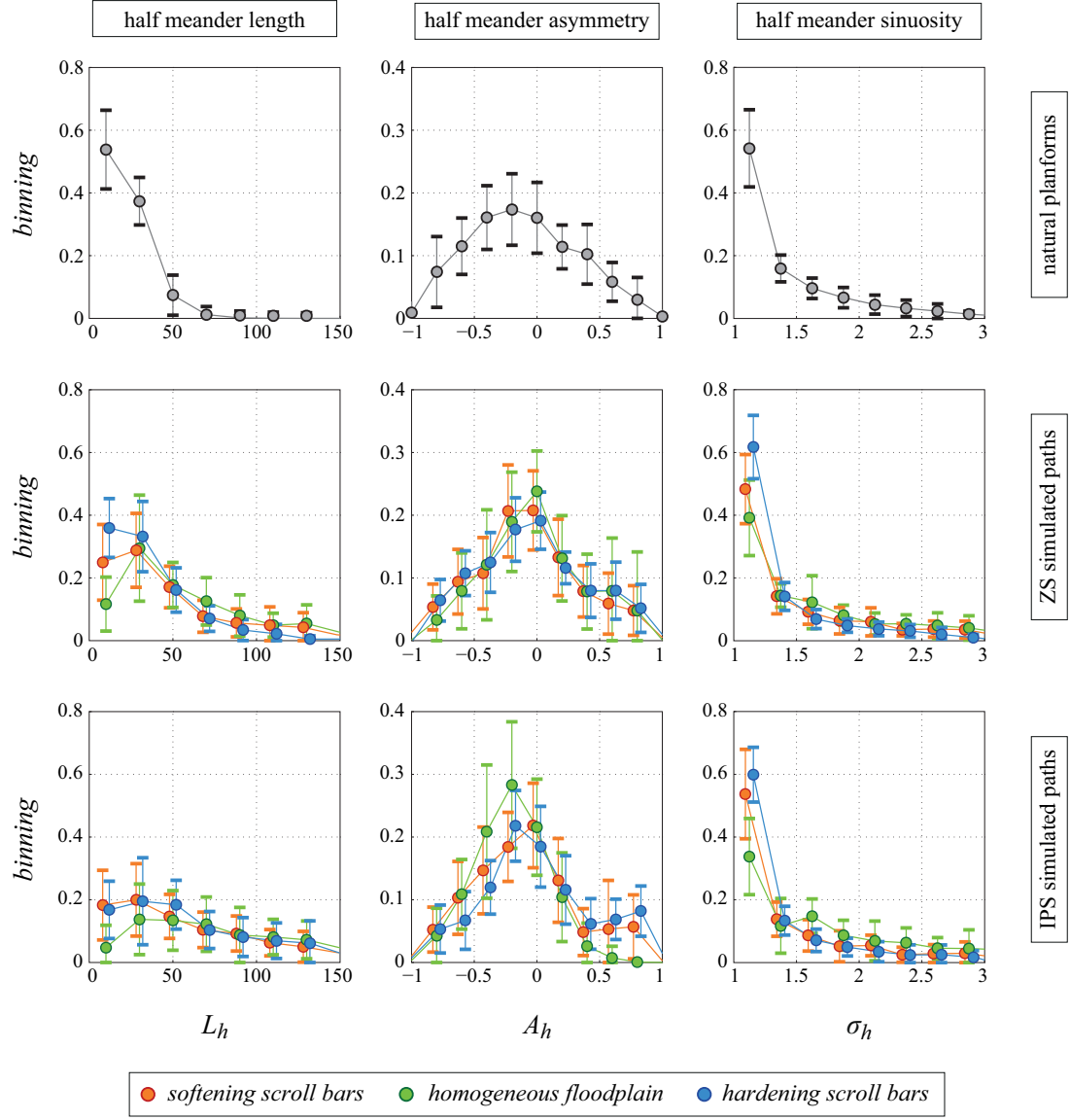


Figure 4.6: Means and standard deviations of the binned spatial series of the three half meander metrics: the length  $L_h$  (left panels), the asymmetry  $A_h$  (central panels), and the sinuosity  $\sigma_h$  (right panels). The first row (gray markers) refers to the natural planforms, while the second and the third rows (coloured markers) refer to the ZS-simulated paths and to the IPS-simulated paths, respectively.

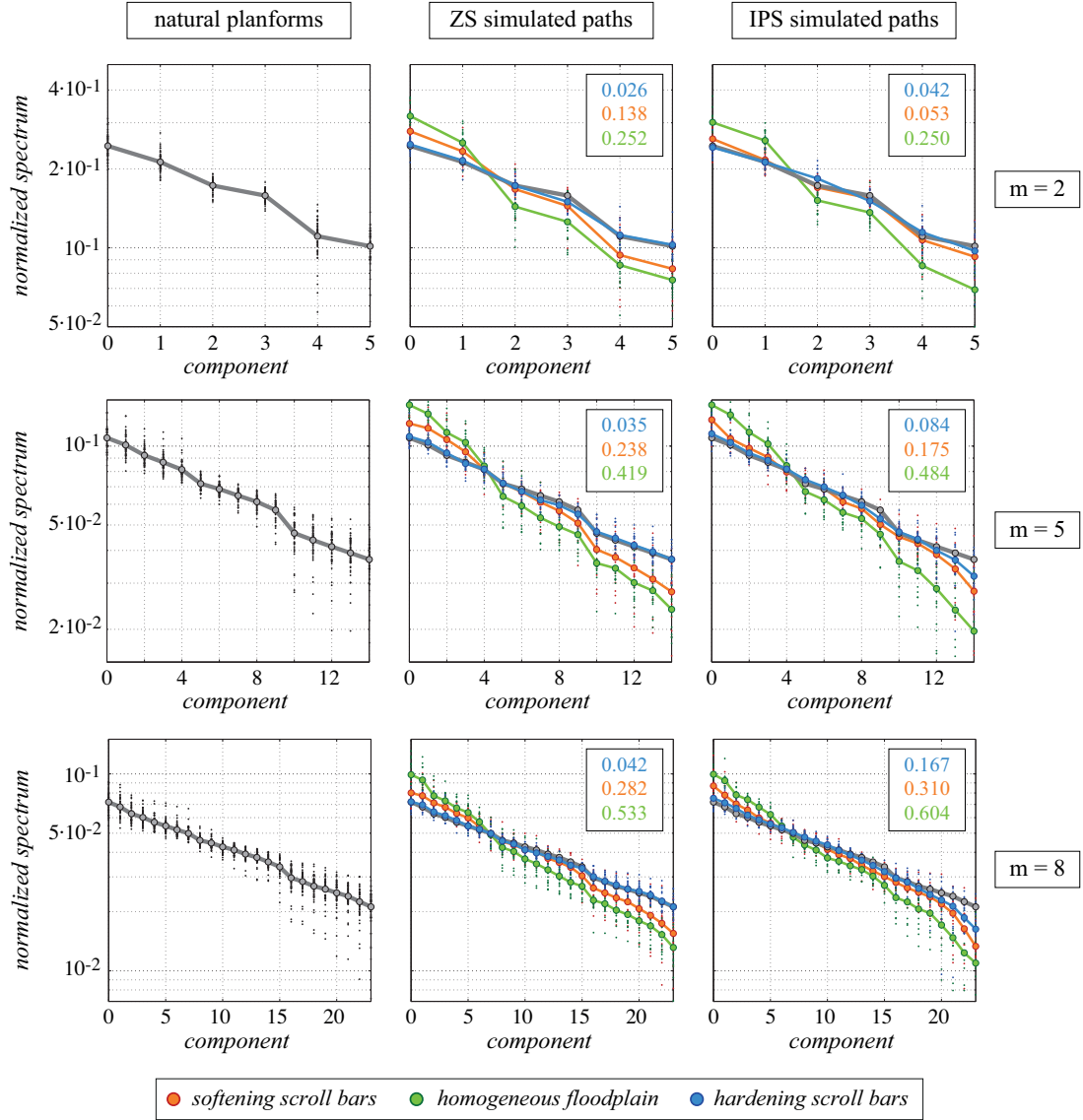


Figure 4.7: Normalized MSSA spectra of the spatial three-channel signals composed by the half meander length  $L_h$ , half meander asymmetry  $A_h$ , and half meander sinuosity  $\sigma_h$  for natural planforms (left panels) and synthetic paths generated by using the ZS (central panels) and the IPS (right panels) flow field models. Three different window sizes were adopted:  $m = 2$  (upper panels),  $m = 5$  (central panels), and  $m = 8$  (lower panels). The multivariate signals were pre-processed by PCA. Thick lines link the average values for each spectral component. The coloured number are the RSS (residual sum of squares) between the simulated average trends and the average trends of natural planforms, which are repeated for comparison purposes in the simulated path panels.

of  $L_h$ , which, similarly to the IPS-generated paths, do not show any kind of clustering. Analogous conclusions may be derived from the  $\sigma_h$  binning, even though differences are less pronounced and clustering is stronger. Binning plots of  $A_h$  reveal that both natural and simulated half meanders exhibit a wide range of skewness. Nevertheless, numerically generated planforms (especially IPS ones) are characterized by a slightly higher frequency of upstream skewed meanders.

In summary, the heterogeneity produces variability in terms of half meander length and sinuosity, whereas the asymmetry does not show any predominant common behaviour.

MSSA applied to the spatial distribution of  $L_h$ ,  $A_h$ , and  $\sigma_h$  involves a three-channel matrix for each planform, either natural or simulated, previously normalized via PCA. Figure 4.7 illustrates the MSSA spectra, and their average values for each component, referred to the different erodibility scenarios. Three windows size were employed to investigate the interplay among adjacent half meanders ( $m = 2$ ) and longer features ( $m = 5$  and  $m = 8$ ), leading to a lag-covariance matrix of rank  $m \times 3 = 6, 15$  and  $18$  respectively. The trends suggest qualitatively similar behaviours for all the tested window sizes. The steepness of the spectra, on average, is higher for the homogeneous cases while the hardening case exhibits the mildest spectrum steepness, independently on the considered flow field model. As a consequence, the hardening scenario is characterized by a more spatially structured geometry signal, and, in term of MSSA spectral behaviour, a closer similarity with the average trends associated with natural geometries, especially when using the ZS model.

### Full meander curvature

The distribution of the curvature of the full meanders (i.e. the channel reaches composed by two consecutive half meanders and, hence, containing three consecutive inflection points of the axis) is here inspected through Fourier Analysis (FA) and Singular Spectrum Analysis (SSA). Both techniques split the input signal in a set of primitive components, but FA approximates the signal with a series of sinusoidal functions, whereas SSA embeds the input signal in a vector space of given dimension  $m$ . Since both natural and simulated full meanders are discretized by polylines, the local curvature  $\mathcal{C}_i$  is defined at the  $i$ th node of the channel axis, yielding discrete signals.

Figure 4.8 shows the power spectra, normalized to the power density, of all the

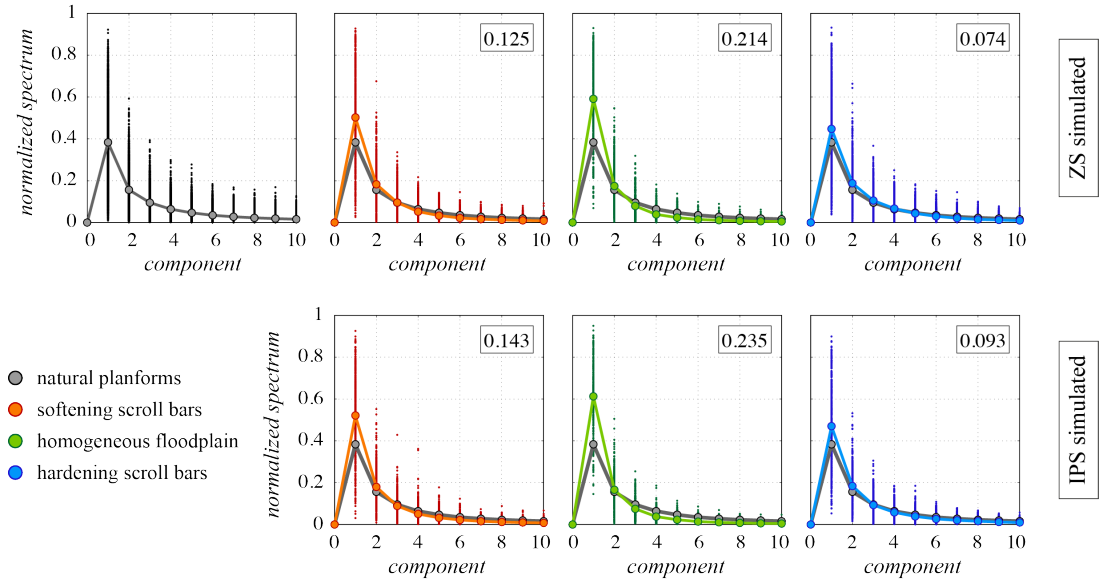


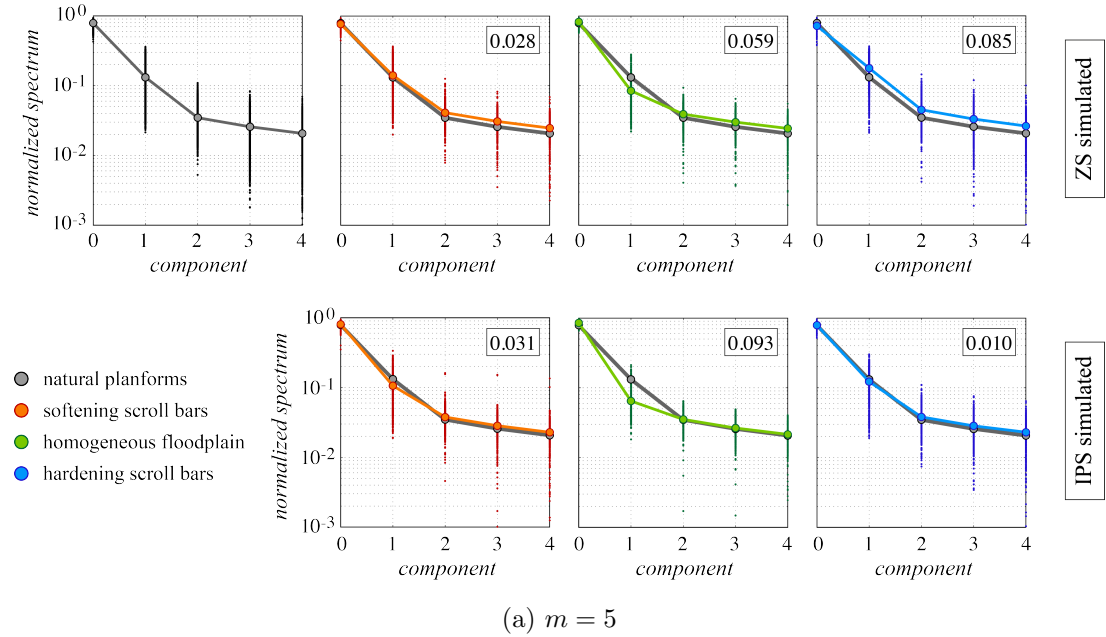
Figure 4.8: Power spectra of the distributions of full meander curvature, normalized to the total power density, for natural planforms (left panel), ZS-simulated paths (upper row), and IPS-simulated paths (lower row). Solid lines connect the average value per harmonic. The numbers correspond to the RSS (residual sum of squares) between the simulated average trends and the average trend of natural planforms, which is repeated for comparison purposes in the simulated path panels.

considered meanders. Signals were previously detrended, thus the zero harmonics vanish. The first component of the binned spectra invariably exhibit the highest power, and then the following harmonics decreases monotonically. The average trend most similar to that of natural rivers is attained for hardening scroll bar scenarios, which slightly overestimates the first and second harmonics and overlaps to the natural trend for the higher harmonics. The average trend of the softening scenarios shows a larger overestimation of the first harmonic, whereas in the homogeneous case differences with respect to the natural case emerge also in correspondence of the spectrum tails. The two flow field models do not produce significant variations between them and the natural database. In other words, the FA analysis of channel axis curvature appears to poorly discriminate between different signals.

The SSA spectra of the meander curvature distribution carried out with three different window size ( $m = 5, 10$ , and  $15$ ) are reported in Figure 4.9. The general behaviour

of the average trends consists of an exponential decay with a slope break after a number of components roughly equal to half of the considered window length  $m$ . Unlike the Fourier analysis, differences occur when using different flow field models, and for the various heterogeneity scenarios. In particular, the major differences between the natural and the simulated paths are observed for the homogeneous scenarios, where the second-third components are generally lower with respect to the natural case, especially for the IPS-simulated paths. In the presence of heterogeneity, ZS-generated meanders disclose a diffuse shift of the mean trend with respect to the natural paths. The strongest agreement is observed for the IPS-generated meanders and on hardening behaviour of the scroll bars.

In summary, FA and SSA analyses prove that introducing any kind of self-formed heterogeneity on the valley surface leads to variation in the distribution of the local curvature of the channel axis, even though the differences in the mean spectrum trend with respect to natural patterns are in general relatively limited. The analyses of channel axis curvature thus seems to poorly discriminate between different planforms.





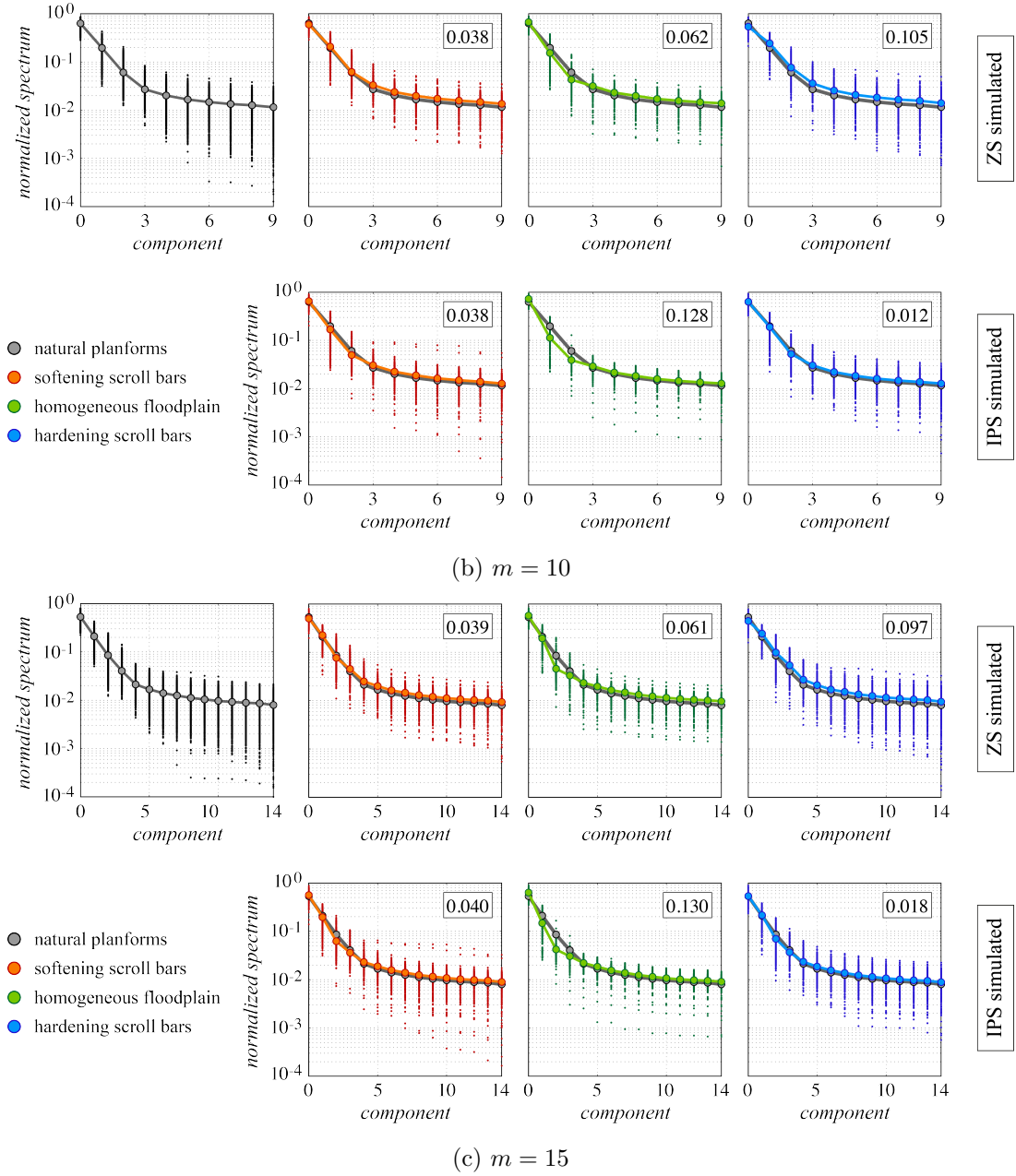


Figure 4.9: Normalized SSA spectra of the distributions of the full meander curvature, for natural planforms (left panels), ZS-simulated paths (upper rows), and IPS-simulated paths (lower row). Three different window sizes were adopted:  $m = 5$  (panels a),  $m = 10$  (panels b), and  $m = 15$  (panels c). Solid lines connect the average value per component. The numbers correspond to the RSS (residual sum of squares) between the simulated average trends and the average trends of natural planforms, which are repeated for comparison purposes in the simulated path panels.

## Overall spatial comparison

Following the approach of Frascati and Lanzoni (2009), a suite of 16 morphometric variables was introduced to characterize through Principal Component Analysis (PCA) the complexity embedded in meandering geometries and to emphasize the subtle differences which may emerge between apparently similar configurations. The set includes quantities related to three different scales: half meander, full meander and whole reach. Regarding the half meander scale (denoted with the subscript  $h$ ), the considered quantities are four statistics of the length  $L_h$ , the asymmetry  $A_h$  and the sinuosity  $\sigma_h$ , namely the mean, the variance, the skewness and the kurtosis of their spatial distribution along the channels. The full meander scale (denoted with the subscript  $f$ ) is represented by the mean sinuosity, defined as:

$$\sigma_{f,mean} = \frac{1}{N_f} \sum_{i=1}^{N_f} \frac{L_{fi}}{l_{fi}} \quad (4.5)$$

where  $L_f$  and  $l_f$  are the intrinsic and the Cartesian lengths of the full meander, respectively, while  $N_f$  is the number of full meanders forming the reach. Further quantities referred to the full meander scale (e.g. asymmetry) are redundant with respect to the half meander quantities. Finally, the reach scale (denoted with the subscript  $t$ ) is analysed in terms of variance and kurtosis of the distribution of the local curvature, and the reach sinuosity:

$$\sigma_t = \frac{L_t}{l_t} \quad (4.6)$$

where  $L_t$  and  $l_t$  are the intrinsic and the Cartesian lengths of the reach, respectively. The suite of considered parameters is summarized in Table 4.4.

The PCA is performed on the matrix that results by assembling the row vectors containing the above defined 16 statistical variables for each path, either natural or simulated. The aim is to convert the original data set in an equivalent data set with a lower dimensionality, but ensuring a relatively small loss of information.

The closer affinity with the natural planforms displayed by the synthetic meanders in the hardening scenario is confirmed by the PCA results shown in Figure 4.10. The scatter plot of the first three components,  $a_1$ ,  $a_2$ , and  $a_3$ , relative to the three largest eigenvalues, is shown, with the two-dimensional projections of the resulting combinations of pairs.

The three components account for about the 55 % of the total variance. The spatial

Table 4.4: Suite of morphometric parameters considered to characterize the meander planforms, either natural or numerically generated, and to compare them through PCA.

Characteristic scale	Variable	Description
Half meander	$L_{h,mean}$	average half meander length
	$L_{h,var}$	variance of the half meander length
	$L_{h,skew}$	skewness of the half meander length
	$L_{h,kurt}$	kurtosis of the half meander length
	$A_{h,mean}$	average half meander asymmetry
	$A_{h,var}$	variance of the half meander asymmetry
	$A_{h,skew}$	skewness of the half meander asymmetry
	$A_{h,kurt}$	kurtosis of the half meander asymmetry
	$\sigma_{h,mean}$	average half meander sinuosity
	$\sigma_{h,var}$	variance of the half meander sinuosity
	$\sigma_{h,skew}$	skewness of the half meander sinuosity
	$\sigma_{h,kurt}$	kurtosis of the half meander sinuosity
Full meander	$\sigma_{f,mean}$	average half meander length
Whole reach	$\sigma_t$	sinuosity of the reach
	$\mathcal{C}_{t,var}$	variance of the curvature distribution
	$\mathcal{C}_{t,kurt}$	kurtosis of the curvature distribution

distribution is relatively significant, with a clear separation of the markers related to the homogeneous case, which are more spread (in particular the IPS-simulated paths), and the markers related to the natural planforms, which are very close among each other. Softening case and hardening case markers lie between the previous two sets, with the latter partially overlapping the natural path cluster, in particular the ZS-simulated paths. The first two components,  $a_1$  and  $a_2$ , account for about the 45 % of the total variance. The clustering of the softening scenario markers is evident, as well as the proximity of the hardening scenario markers to those characterizing the natural paths, which are mainly concentrated in the quadrant where  $a_1$  is positive and  $a_2$  is negative. The markers corresponding to the homogeneous case are very spread, and mainly localized in the negative  $a_1$  half plane, thus showing an opposite behaviour with respect to the natural path cluster. The degree of clustering decreases with the order of

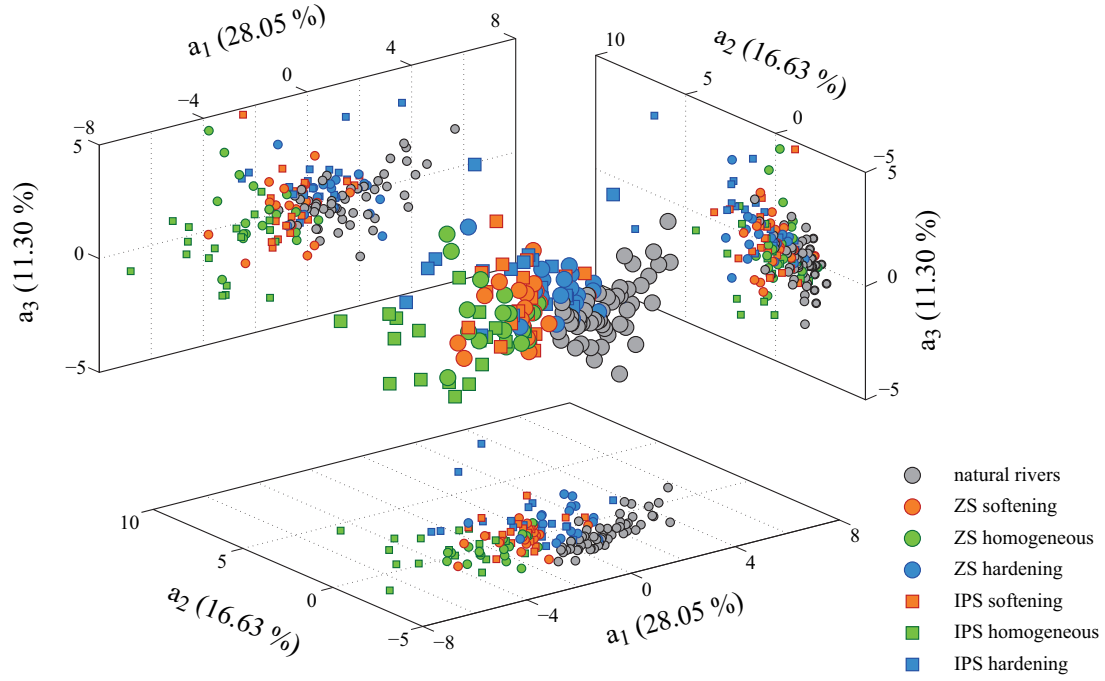


Figure 4.10: Three-dimensional scatter plot of the first three components of morphometric data of natural rivers and simulated paths processed by Principal Component Analysis (PCA), coupled with the projections in orthogonal two-dimensional reference systems (lateral panels). Each axis is labelled with the respective percentage of variance.

the components, as the total variance accounted for the components and the difference in variance between two consecutive components progressively decrease. Indeed, while in the  $a_1 - a_3$  plane the clustering clearly emerges, in the  $a_2 - a_3$  plane only the natural path cluster remains nearly clear.

Analogously to SSA, MSSA and FA, the normalized spectrum of PCA is an indicator of the splitting of information along the Principal Components. (Figure 4.11).

The spectrum decays nearly exponentially (i.e. linearly in the semi-log plot), with the successive 13 out of 16 eigenvalues carrying the residual variance (about 45 %), not described by the first three components, up to small values of the order of  $10^{-3}$ . As a consequence, the application of PCA to the selected set of morphometric parameters allows to reduce the dimensionality of the problem through a basis transformation, without dropping a significant amount of information.

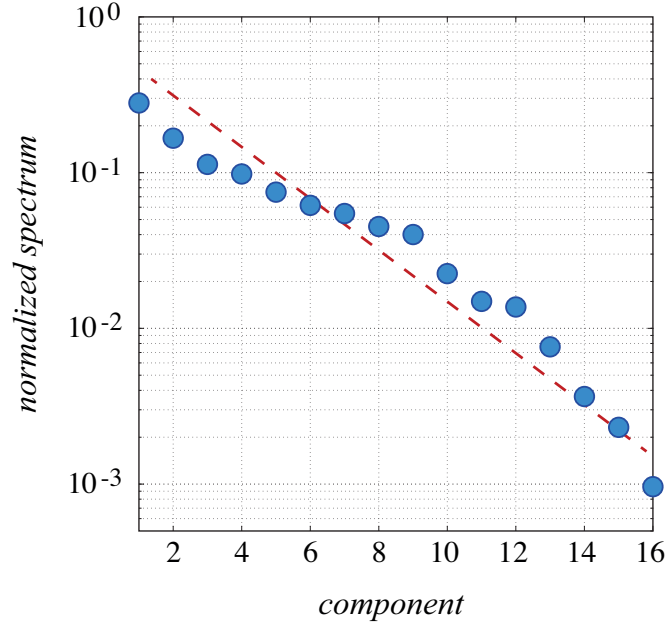


Figure 4.11: Normalized eigenvalue spectrum of the correlation matrix of the Principal Component Analysis (PCA).

## 4.5 Discussion

River migration, point bar deposits and oxbow lake formation concur together to shape the lowland floodplain environment. On one hand, oxbow lakes are the inevitable product of the reworking action of the meandering process, whereby the continuous elongation of bends driven by erosion at the outer bank and deposition at the inner bank is eventually limited by cutoff occurrence. On the other hand, they contribute, together with point bar complexes, to alter the sedimentological structure of the floodplain and, consequently, exert a strong control on meander evolution by varying the soil erodibility of an otherwise homogeneous floodplain.

Soil heterogeneities caused by oxbow lakes depend on the type and amount of sediment filling (Constantine et al., 2010). Neck cutoffs, as those considered in the simulations, tend to produce oxbow lakes with relatively large diversion angles that favour aggradation of the entrances of the abandoned channel. The oxbow lake then become quickly disconnected from the river, and the resulting accommodation space is mainly filled by wash load delivered during floods. In some cases, sediment-laden flow can be conveyed from the main river by tie channels that develop as oxbow lakes become iso-

lated (Rowland et al., 2005). The filling process may last for many decades, depending on the rate of sediment supply, and eventually leads to the formation of sediment plugs that slow meander migration (Hudson and Kesel, 2000). The sedimentary structure associated to point bars may have a significant impact on floodplain erodibility. Mud-dominant inclined heterolithic strata typical of scroll bars can form as a consequence of the bank pull-bar push dynamics related to lateral channel migration (van De Lageweg et al., 2014). Additional erosion-resistant barrier to lateral channel migration are associated to the fine-grained deposits forming on the most distal parts of point bars (the counter point bars defined by Smith et al. (2009)).

The hardening scenario of the present simulations can then be considered as representative of erosion resistant oxbow fill and counter point bar deposit in rivers with high enough sediment loads, possibly reinforced by the vegetation growth. Conversely, the softening scenario could be related to the case of sandy point bars deposits and oxbow lakes that either exist as open water bodies for many decades, owing to a relatively low supply of sediment, or are intercepted soon after their formation in highly active rivers, with rapid migration and large cutoff rates.

Present results show that the heterogeneity in floodplain composition associated with the formation of preserved geomorphic units, together with the choice of a reliable flow field model to drive channel migration, are two fundamental ingredients for reproducing correctly the long-term morphodynamics of alluvial meanders (Schuurman et al., 2016). The model should be able to account for the whole range of morphodynamic conditions (subresonant and superresonant) and, hence, to reproduce the wide variety of bends (upstream-skewed, downstream-skewed, compound, multiple loops) observed in nature, without invoking spatial heterogeneities of the bank resistance to erosion.

The spectral analyses of Section 4.3 applied to the temporal evolution of half meander metrics showed that the simulated meander geometry is strongly affected by the self-formed heterogeneity of the floodplain. In particular, SSA and MSSA showed that the planforms obtained for the softening scenario invariably have a more complex structure with respect to the homogeneous and the hardening case. In other words, the river paths obtained for the the hardening cases have a shorter memory of their past states, which reflects in a relatively more elementary structure of the temporal distribution of half meander metrics.

Similarly, the spatial analyses of Section 4.4 showed that floodplain heterogeneities

associated with scroll bar units produced by the migration process itself add a further degree of complexity to the channel patterns. From a purely geometrical point of view, all morphological analyses of spatial features concur to establish that patterns generated by assuming scroll bars less erodible than the surrounding floodplain are more akin to natural meander shapes. Moreover, even in the presence of river-induced floodplain heterogeneities, ZS-created patterns are still those that better resemble natural landforms. Differently from the results of the time analysis of half meander metrics, the analysis of the meander geometry showed that the spatial trends related to the hardening scenarios have a more complex structure with respect to the softening and the homogeneous cases. Simulating the river migration with the assumption that scroll bars are less erodible than the surrounding floodplain leads to planforms which are relatively highly correlated in space and less correlated in time, if compared to the case of more erodible scroll bars or a homogeneous floodplain.

Clearly, other processes can affect the distribution of heterogeneities across a floodplain, and deserve attention in future research. Oxbow lakes created by chute cutoffs (non treated in the simulations) generally have lower diversion angles than neck cutoffs. The enhanced delivery of coarse sediment from the active channel thus tends to slow the closure of the abandoned reach (Constantine et al., 2010), with a consequently modified (likely smaller) resistance to erosion when the active meandering river migrates again into the oxbow. Geological constraint (e.g., rock outcrops), land use and vegetation patterns matter as well. In many cases, woodland species are densest along the boundaries of the active river and oxbow lakes, while grassland species prevail on the remaining floodplain. The high density of large roots in cutbanks thus decreases bank erodibility (Allmendinger et al., 2005). Nevertheless, when vegetation is confined to the tops of tall cutbanks, the erosion at the toe of the bank eventually undermines even root-reinforced slopes (Constantine et al., 2009). These eco-morphodynamic processes still need to be inserted in long-term models of alluvial river evolution.





## Chapter 5

# On the floodplain singularities

This Chapter concerns the numerical modelling of the dynamics of meandering rivers affected by an internal boundary condition which introduces localized changes in the flow field, e.g. a variation in the discharge or in the valley slope. The goal is to extend the applicability of the existing morphodynamic model described in Chapter 2 to a wider range of scenarios, relaxing the hypothesis of a unique uniform flow determining the river behaviour.

The Chapter is organized as follows. Section 5.1 concerns the extension of the mathematical framework introduced in Section 2.4 in order to handle internal boundary conditions depending on the resonance conditions (subresonance or superresonance). Section 5.2 describes the application of the model extension to a real case, namely a treat of the Lower Mississippi River affected by the confluence with the Arkansas River. Four different scenarios are considered, and the results of simulations are outlined in Section 5.3. Finally, Section 5.4 discusses the effects of a boundary condition within the domain, and the possible applications of the developed framework.

### 5.1 Mathematical framework

The widely used mathematical models for the flow field in a meandering river, e.g. the IPS model of Ikeda et al. (1981) and the ZS model of Zolezzi and Seminara (2001) (see Chapters 2 and 4), are based on the assumption that the flow field may be split in two components. The first is relative to the main, uniform flow that establishes throughout the river reach; the second describes the secondary flow driven by the curvature distri-

bution. However, the hypothesis of uniform flow narrows the potential applicability of the mathematical frameworks, since natural rivers seldom exhibit geometric properties (i.e., slope, cross section) that keep constant for sufficiently long distances. The usual way to proceed is to assume average properties, if their variance is relatively small and uniformly distributed in space. On the other hand, the averaging does not work if variations are localized or slowly growing/diminishing. For example, localized variations are determined by the discharge input due to a tributary or by a change in the valley slope. In both cases, flow conditions changes between upstream and downstream due to the singularity, and also a transition channel reach occurs. A typical slowly varying condition concerns the backwater effect that arises in the proximity to the river mouth, where depth progressively increases and velocity decreases. As a first approximation, this setting can be reduced to the previous case by assuming a series of subreaches with progressively different flow conditions.

The problem may be outlined through the sketch in Figure 5.1. The meandering channel is characterized by the presence of a singular section where one or more changes in the main flow field are introduced. As a consequence, also the secondary flow field driven by the channel axis curvatures is affected by these changes. Labelling the intrinsic coordinate of the singular section as  $s = L_0$ , the part of the channel in the range  $0 \leq s \leq L_0$  is hereafter defined as upstream subreach  $u$ , while the part in the range  $L_0 \leq s \leq L_1$  is hereafter defined as downstream subreach  $d$ .

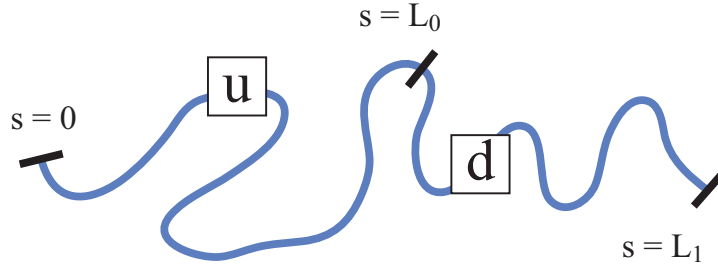


Figure 5.1: Sketch of a meandering river affected by a singular section ( $s = L_0$ ) which introduces variations in the main flow and in the curvature-driven secondary circulation. The reach is split in a upstream subreach  $u$  ( $0 \leq s \leq L_0$ ) and in a downstream subreach  $d$  ( $L_0 \leq s \leq L_1$ ).

At the leading order of approximation (the main, uniform flow), the required conditions are the conservation of the liquid flux  $Q_w$  and of the sediment flux  $Q_s$  upstream

(superscript  $u$ ) and downstream (superscript  $d$ ) of the singular section (superscript  $s$ ):

$$\begin{bmatrix} Q_w \\ Q_s \end{bmatrix}_{s=L_0}^u + \begin{bmatrix} \Delta Q_w \\ \Delta Q_s \end{bmatrix}^s = \begin{bmatrix} Q_w \\ Q_s \end{bmatrix}_{s=L_0}^d \quad (5.1)$$

where  $\Delta Q_w$  and  $\Delta Q_s$  are the possible flux variations in the correspondence of the singular section  $s = L_0$ . As shown in Chapter 2, the relevant parameters within a reach are the cross section width  $2B_0^*$ , the bed slope  $S$ , the characteristic grain size  $d_s^*$ , and one among the water discharge  $Q_w^*$ , the stream velocity  $U_0^*$ , and the flow depth  $D_0^*$ . Thus four dimensional parameters (superscript  $*$ ) can be defined for each subreach. Since (5.1) is a system of two equations, the problem has six degrees of freedom: six of the eight dimensional quantities listed above (four per each channel subreach) need to be assigned a priori, whereas the remaining two are given by the constraint imposed by equations (5.1). A discontinuity of the cross section geometry in correspondence of the singular section thus occurs in terms of uniform conditions. If the changes in uniform conditions between the two subreaches are not very different, they may be treated as concentrated into the singular section  $s = L_0$ .

Analogous conditions are required for the curvature-driven secondary flow. Hence the coupling between the curvature-driven flow of the upstream subreach in correspondence of its downstream end, i.e. the singular section  $s = L_0$ , and the analogous curvature-driven flow of the downstream subreach in correspondence of its upstream end, i.e. again the singular section  $s = L_0$ , has to be considered.

The IPS model (Ikeda et al., 1981) can not be used to satisfy the continuity requirements. Indeed, it accounts only for the upstream influence of the curvature distribution (Lanzoni et al., 2006; Lanzoni and Seminara, 2006), and the information can propagate only downstream. Any perturbation localized in the singular section could not influence the upstream part. On the other hand, the ZS model (Zolezzi and Seminara, 2001) is characterized by four particular solutions that, combined together, can be used to satisfy the continuity requirements. This particularity of the ZS model is strictly linked to its ability to handle both sub- and super-resonance conditions or, in other words, the upstream and the downstream influence. In the following the ZS model will be extended in order to treat coupled meandering domains.

### The solution of Zolezzi and Seminara (2001)

Following the notation of Chapter 2, the dimensionless solution of the fully coupled morphodynamic framework of Zolezzi and Seminara (2001) reads:

$$\begin{bmatrix} U \\ V \\ D \\ H \end{bmatrix} = \begin{bmatrix} 1 \\ 0 \\ 1 \\ 1 \end{bmatrix} + \nu_0 \begin{bmatrix} u \\ v \\ d \\ h \end{bmatrix} + O(\nu_0^2) \quad (5.2)$$

where  $(U, V) = (U^*, V^*)/U_0^*$  are the dimensionless velocity components while  $(D, H) = (D^*, H^*)/D_0^*$  are the dimensionless flow depth and the free surface elevation, given by the sum of the uniform flow components and of the dimensionless perturbations  $(u, v) = (u^*, v^*)/U_0^*$ ,  $(d, h) = (d^*, h^*)/D_0^*$  driven by the curvature distribution. The latter are then decomposed as follows:

$$\begin{bmatrix} u \\ v \\ d \\ h \end{bmatrix} = \begin{bmatrix} 0 \\ 0 \\ \bar{d}_1 \mathcal{C} + \bar{d}_2 \mathcal{C}' + \bar{d}_3 \mathcal{C}'' \\ \bar{h}_1 \mathcal{C} + \bar{h}_2 \mathcal{C}' + \bar{h}_3 \mathcal{C}'' \end{bmatrix} n + \sum_{m=0}^{\infty} \begin{bmatrix} u_m \sin(Mn) \\ v_m \cos(Mn) \\ d_m \sin(Mn) \\ h_m \sin(Mn) \end{bmatrix} \quad (5.3)$$

where  $\bar{h}_i$  and  $\bar{d}_i$  ( $i = 1, 2, 3$ ) are coefficients depending on the aspect ratio  $\beta$ , the Shields number  $\tau_*$ , the friction coefficient  $C_f$  and the sediment transport intensity  $\Phi$ . In addition,  $\mathcal{C}$  is the local curvature having first- and second-order derivatives  $\mathcal{C}'$  and  $\mathcal{C}''$ , respectively. Finally  $n$  is the dimensionless transverse coordinate, which ranges from -1 to +1, while  $M = (2m + 1)\pi/2$  emerges from the Fourier series decomposition.

The vectorial form of the solution for the terms in the Fourier expansion reads:

$$\mathcal{Q}_m(s) = \hat{A}_m \sum_{j=1}^4 \mathcal{T}_{mj} g_{j0} \int_{s_0}^s e^{\lambda_{mj}(s-t)} \mathcal{C}(t) dt + \sum_{j=1}^4 \mathcal{T}_{mj} c_{mj} e^{\lambda_{mj}(s-s_0)} + \hat{A}_m \sum_{j=1}^4 \mathcal{L}_{mj}(s) \quad (5.4)$$

where:

$$\mathcal{Q}_m(s) = \begin{bmatrix} u_m \\ v_m \\ d_m \\ h_m \end{bmatrix} \quad \mathcal{T}_{mj} = \begin{bmatrix} 1 \\ \phi_{mj} \\ \delta_{mj} \\ \xi_{mj} \end{bmatrix} \quad \mathcal{L}_{mj}(s) = \begin{bmatrix} g_{j1}\mathcal{C} \\ \sum_{k=1}^9 \phi_{mjk}\mathcal{C}^{k-1} \\ \sum_{k=1}^9 \delta_{mjk}\mathcal{C}^{k-1} \\ \sum_{k=1}^9 \xi_{mjk}\mathcal{C}^{k-1} \end{bmatrix} \quad (5.5)$$

The terms  $\phi_{mj}$ ,  $\delta_{mj}$ ,  $\xi_{mj}$ ,  $\phi_{mjk}$ ,  $\delta_{mjk}$ , and  $\xi_{mjk}$  are functions of  $\beta$ ,  $\tau_*$ ,  $C_f$ ,  $\Phi$ , while  $g_{j0}$  and  $g_{j1}$  depend on the vertical decomposition of the flow field (Zolezzi and Seminara, 2001). Moreover,  $\hat{A}_m = 2(-1)^2/M^2$ , while the four coefficients  $c_{mj}$  are associated with the particular solutions of the mathematical problem for each Fourier mode  $m$ . They are determined through the boundary conditions imposed at the upstream and downstream ends of the considered reach (Lanzoni and Seminara, 2006). Hereafter, for the sake of simplicity, the following compact notations will replace the extended convolution integrals appearing in (5.4):

$$\mathcal{I}(\lambda, s, s_0) = \int_{s_0}^s e^{\lambda_m(s-t)} \mathcal{C}(t) dt \quad (5.6)$$

$$\mathcal{I}(-\lambda, s, s_0 + L) = \int_s^{s_0+L} e^{-\lambda_m(t-s)} \mathcal{C}(t) dt \quad (5.7)$$

Two situations can occur, depending on the values of the characteristic exponents  $\lambda_{mj}$ , namely the subresonant conditions or the superresonant conditions.

In the subresonant conditions, one of the eigenvalues is real and positive (i.e.  $\lambda_{m1} > 0$ ), two eigenvalues are complex conjugate with negative real part (i.e.  $\lambda_{m2}^r = \lambda_{m3}^r < 0$ ,  $\lambda_{m2}^i = -\lambda_{m3}^i$ ), and the fourth eigenvalue is real and negative (i.e.  $\lambda_{m4} < 0$ ). The solution may be rewritten as follows:

$$\begin{aligned} \mathcal{Q}_m(s) = & -\hat{A}_m \mathcal{T}_{m1} g_{10} \mathcal{I}(-\lambda_{m1}, s, s_0 + L) + \hat{A}_m \sum_{j=2}^4 \mathcal{T}_{mj} g_{j0} \mathcal{I}(\lambda_{mj}, s_0, s) + \\ & + \mathcal{T}_{m1} c_{m1} e^{-\lambda_{m1}(s_0+L-s)} + \sum_{j=2}^4 \mathcal{T}_{mj} c_{mj} e^{\lambda_{mj}(s-s_0)} + \hat{A}_m \sum_{j=1}^4 \mathcal{L}_{mj}(s) \end{aligned} \quad (5.8)$$

where  $L$  is the value attained by the intrinsic coordinate  $s$  at the downstream end of the investigated reach.

In the superresonant conditions, one of the eigenvalues is real and positive (i.e.  $\lambda_{m1} > 0$ ), two eigenvalues are complex conjugate with positive real part (i.e.  $\lambda_{m2}^r = \lambda_{m3}^r > 0$ ,  $\lambda_{m2}^i = -\lambda_{m3}^i$ ), and the fourth eigenvalue is real and negative (i.e.  $\lambda_{m4} < 0$ ). The solution may be rewritten as follows:

$$\begin{aligned} \mathcal{Q}_m(s) = & -\hat{A}_m \sum_{j=1}^3 \mathcal{T}_{mj} g_{j0} \mathcal{I}(-\lambda_{mj}, s, s_0 + L) + \hat{A}_m \mathcal{T}_{m4} g_{40} \mathcal{I}(\lambda_{m4}, s_0, s) + \\ & + \sum_{j=1}^3 \mathcal{T}_{mj} c_{mj} e^{-\lambda_{mj}(s_0+L-s)} + \mathcal{T}_{m4} c_{m4} e^{\lambda_{m4}(s-s_0)} + \hat{A}_m \sum_{j=1}^4 \mathcal{L}_{mj}(s) \end{aligned} \quad (5.9)$$

Each of the 4 components ( $u_m$ ,  $v_m$ ,  $d_m$ ,  $h_m$ ) of the flow field is composed by 5 terms: the contribution given by the downstream distribution of the curvature propagating upstream, the contribution given by the upstream distribution of the curvature propagating downstream, the effects of the downstream boundary conditions extending upstream, the effect of the the upstream boundary conditions extending downstream, and the contribution given by the local curvature and its derivatives. For each mode  $m$ , the subresonant scenario requires three boundary conditions assigned at the upstream reach end while the remaining one must be assigned at the downstream reach end. Conversely, the superresonant scenario requires only one boundary condition at the upstream reach end and the remaining three must be assigned at the downstream reach end.

As discussed above, the goal is to couple the curvature-driven perturbations across the singular sections  $S = L_0$ . Hence:

$$\begin{bmatrix} u \\ v \\ d \\ h \end{bmatrix}_{s=L_0}^u = \begin{bmatrix} u \\ v \\ d \\ h \end{bmatrix}_{s=L_0}^d \quad (5.10)$$

In order to limit the mathematical and numerical efforts, the hypothesis is to assume, as a first approximation, that the  $\bar{h}_i$  and  $\bar{d}_i$  ( $i = 1, 2, 3$ ) referred to the upstream and the downstream subreaches are very similar. As a consequence, equation (5.10) simplifies

as follows with (5.3):

$$\sum_{m=0}^{\infty} \begin{bmatrix} u_m \sin(Mn) \\ v_m \cos(Mn) \\ d_m \sin(Mn) \\ h_m \sin(Mn) \end{bmatrix}_{s=L_0}^u = \sum_{m=0}^{\infty} \begin{bmatrix} u_m \sin(Mn) \\ v_m \cos(Mn) \\ d_m \sin(Mn) \\ h_m \sin(Mn) \end{bmatrix}_{s=L_0}^d \quad (5.11)$$

The problem hence simplifies in forcing the perturbations to be equal at each Fourier mode  $m = 0, \infty$ :

$$\begin{bmatrix} u_m \\ v_m \\ d_m \\ h_m \end{bmatrix}_{s=L_0}^u = \begin{bmatrix} u_m \\ v_m \\ d_m \\ h_m \end{bmatrix}_{s=L_0}^d \quad (5.12)$$

The unknowns are 8 (i.e. 4 coefficients  $c_{mj}^u$  for the upstream part and 4 coefficients  $c_{mj}^d$  for the downstream part, for each mode  $m$ ) thus further 4 conditions should apparently be introduced in addition to the requirement (5.12). In practice, however, some terms can be neglected because of their exponential decaying character (Figure 5.2).

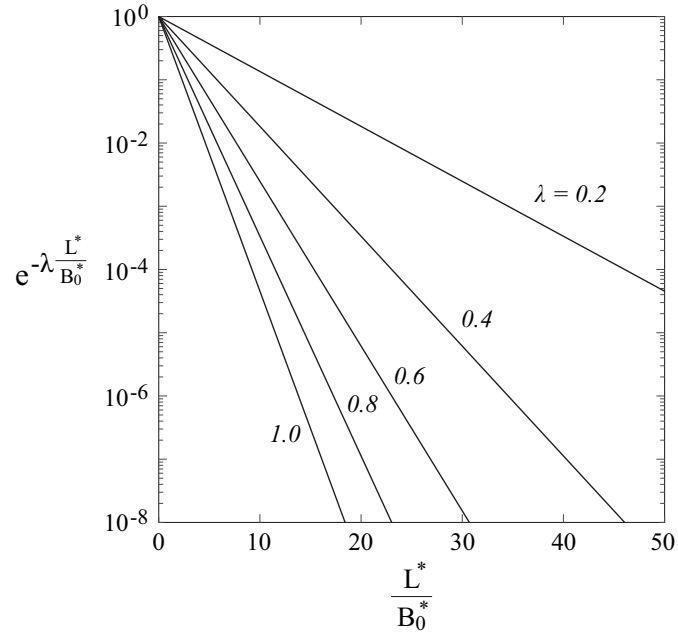


Figure 5.2: Typical behaviour of the exponential terms appearing in the solution of the ZS model for five values of the characteristic exponent  $\lambda_{mj}$ .

Moreover, the possible resonance conditions of the two subreaches must be coupled. The feasible combinations read:

- subresonant upstream subreach, subresonant downstream subreach (SUB-SUB);
- superresonant upstream subreach, superresonant downstream subreach (SUPER-SUPER);
- subresonant upstream subreach, superresonant downstream subreach (SUB-SUPER);
- superresonant upstream subreach, subresonant downstream subreach (SUPER-SUB);

Hereafter the four possible cases will be analysed in order to obtain a solution for the values of  $c_{mj}^u$  and  $c_{mj}^d$ .

### **SUB-SUB case**

The scenario in which both the upstream and the downstream subreaches are subresonant is here considered. Both subreaches require 3 boundary conditions at their respective upstream end, and the remaining one at their downstream end. Since the upstream subreach shares its downstream end with the upstream end of the downstream subreach, the following conditions occur:

- 3 boundary conditions ( $v_m|_0$ ,  $d_m|_0$ ,  $h_m|_0$ ) at the upstream end of the upstream subreach;
- 4 internal conditions (eq. 5.12) at the singular section required by the continuity of the perturbed flow;
- 1 boundary condition ( $u_m|_{L_1}$ ) at the downstream end of the upstream subreach.



The curvature-driven flow field for the upstream and the downstream subreaches then reads:

$$\begin{aligned}\mathcal{Q}^u(s) = & -\hat{A}_m \mathcal{T}_{m1}^u g_{10}^u \mathcal{I}(-\lambda_{m1}^u, s, L_0) + \hat{A}_m \sum_{j=2}^4 \mathcal{T}_{mj}^u g_{j0}^u \mathcal{I}(\lambda_{mj}^u, 0, s) + \\ & + \mathcal{T}_{m1}^u c_{m1}^u e^{-\lambda_{m1}^u(L_0-s)} + \sum_{j=2}^4 \mathcal{T}_{mj}^u c_{mj}^u e^{\lambda_{mj}^u s} + \hat{A}_m \sum_{j=1}^4 \mathcal{L}_{mj}^u(s)\end{aligned}\quad (5.13)$$

$$\begin{aligned}\mathcal{Q}^d(s) = & -\hat{A}_m \mathcal{T}_{m1}^d g_{10}^d \mathcal{I}(-\lambda_{m1}^d, s, L_1) + \hat{A}_m \sum_{j=2}^4 \mathcal{T}_{mj}^d g_{j0}^d \mathcal{I}(\lambda_{mj}^d, L_0, s) + \\ & + \mathcal{T}_{m1}^d c_{m1}^d e^{-\lambda_{m1}^d(L_1-s)} + \sum_{j=2}^4 \mathcal{T}_{mj}^d c_{mj}^d e^{\lambda_{mj}^d(s-L_0)} + \hat{A}_m \sum_{j=1}^4 \mathcal{L}_{mj}^d(s)\end{aligned}\quad (5.14)$$

Evaluating the previous equations at  $s = L_0$ :

$$\begin{aligned}\mathcal{Q}^u(L_0) = & -\hat{A}_m \mathcal{T}_{m1}^u g_{10}^u \mathcal{I}(-\lambda_{m1}^u, L_0, L_0) + \hat{A}_m \sum_{j=2}^4 \mathcal{T}_{mj}^u g_{j0}^u \mathcal{I}(\lambda_{mj}^u, 0, L_0) + \\ & + \mathcal{T}_{m1}^u c_{m1}^u e^{-\lambda_{m1}^u(L_0-L_0)} + \sum_{j=2}^4 \mathcal{T}_{mj}^u c_{mj}^u e^{\lambda_{mj}^u L_0} + \hat{A}_m \sum_{j=1}^4 \mathcal{L}_{mj}^u(L_0)\end{aligned}\quad (5.15)$$

$$\begin{aligned}\mathcal{Q}^d(L_0) = & -\hat{A}_m \mathcal{T}_{m1}^d g_{10}^d \mathcal{I}(-\lambda_{m1}^d, L_0, L_1) + \hat{A}_m \sum_{j=2}^4 \mathcal{T}_{mj}^d g_{j0}^d \mathcal{I}(\lambda_{mj}^d, L_0, L_0) + \\ & + \mathcal{T}_{m1}^d c_{m1}^d e^{-\lambda_{m1}^d(L_1-L_0)} + \sum_{j=2}^4 \mathcal{T}_{mj}^d c_{mj}^d e^{\lambda_{mj}^d(L_0-L_0)} + \hat{A}_m \sum_{j=1}^4 \mathcal{L}_{mj}^d(L_0)\end{aligned}\quad (5.16)$$

and, removing the terms equal to zero:

$$\begin{aligned}\mathcal{Q}^u(L_0) = & \hat{A}_m \sum_{j=2}^4 \mathcal{T}_{mj}^u g_{j0}^u \mathcal{I}(\lambda_{mj}^u, 0, L_0) + \\ & + \mathcal{T}_{m1}^u c_{m1}^u + \sum_{j=2}^4 \mathcal{T}_{mj}^u c_{mj}^u e^{\lambda_{mj}^u L_0} + \hat{A}_m \sum_{j=1}^4 \mathcal{L}_{mj}^u(L_0)\end{aligned}\quad (5.17)$$

$$\begin{aligned}\mathcal{Q}^d(L_0) = & -\hat{A}_m \mathcal{T}_{m1}^d g_{10}^d \mathcal{I}(-\lambda_{m1}^d, L_0, L_1) + \\ & + \mathcal{T}_{m1}^d c_{m1}^d e^{-\lambda_{m1}^d(L_1-L_0)} + \sum_{j=2}^4 \mathcal{T}_{mj}^d c_{mj}^d + \hat{A}_m \sum_{j=1}^4 \mathcal{L}_{mj}^d(L_0)\end{aligned}\quad (5.18)$$

Assuming that  $L_0$  and  $L_1 - L_0$  are sufficiently large leads to a rapid decay of the exponential terms such that they may be neglected (Figure 5.2). Subtracting these

relations and rearranging in order to obtain the explicit relations to be applied at the singularity, the resulting equation reads:

$$\begin{aligned}
& \mathcal{T}_{m1}^u c_{m1}^u - \mathcal{T}_{m2}^d c_{m2}^d - \mathcal{T}_{m3}^d c_{m3}^d - \mathcal{T}_{m4}^d c_{m4}^d = \\
& = -\hat{A}_m \left\{ \sum_{j=2}^4 \mathcal{T}_{mj}^u g_{j0}^u \mathcal{I}(\lambda_{mj}^u, 0, L_0) + \mathcal{T}_{m1}^d g_{10}^d \mathcal{I}(-\lambda_{m1}^d, L_0, L_1) + \right. \\
& \quad \left. + \sum_{j=1}^4 [\mathcal{L}_{mj}^u(L_0) - \mathcal{L}_{mj}^d(L_0)] \right\}
\end{aligned} \tag{5.19}$$

This equation provides a linear system of 4 equations in the 4 variables  $c_{m1}^u$ ,  $c_{m2}^d$ ,  $c_{m3}^d$ , and  $c_{m4}^d$  that, in matrix form, reads  $Ac = B$ , where:

$$A = \frac{1}{\hat{A}_m} \begin{bmatrix} 1 & -1 & -1 & -1 \\ \phi_{m1}^u & -\phi_{m2}^d & -\phi_{m3}^d & -\phi_{m4}^d \\ \delta_{m1}^u & -\delta_{m2}^d & -\delta_{m3}^d & -\delta_{m4}^d \\ \xi_{m1}^u & -\xi_{m2}^d & -\xi_{m3}^d & -\xi_{m4}^d \end{bmatrix} \quad c = \begin{bmatrix} c_{m1}^u \\ c_{m2}^d \\ c_{m3}^d \\ c_{m4}^d \end{bmatrix} \tag{5.20}$$

$$B = \begin{bmatrix} -\sum_{j=2}^4 g_{j0}^u \mathcal{I}(\lambda_{mj}^u, 0, L_0) - g_{10}^d \mathcal{I}(-\lambda_{m1}^d, L_0, L_1) - \sum_{j=1}^4 [\mathcal{L}_{u,mj}^u(L_0) - \mathcal{L}_{u,mj}^d(L_0)] \\ -\sum_{j=2}^4 \phi_{mj}^u g_{j0}^u \mathcal{I}(\lambda_{mj}^u, 0, L_0) - \phi_{m1}^d g_{10}^d \mathcal{I}(-\lambda_{m1}^d, L_0, L_1) - \sum_{j=1}^4 [\mathcal{L}_{v,mj}^u(L_0) - \mathcal{L}_{v,mj}^d(L_0)] \\ -\sum_{j=2}^4 \delta_{mj}^u g_{j0}^u \mathcal{I}(\lambda_{mj}^u, 0, L_0) - \delta_{m1}^d g_{10}^d \mathcal{I}(-\lambda_{m1}^d, L_0, L_1) - \sum_{j=1}^4 [\mathcal{L}_{d,mj}^u(L_0) - \mathcal{L}_{d,mj}^d(L_0)] \\ -\sum_{j=2}^4 \xi_{mj}^u g_{j0}^u \mathcal{I}(\lambda_{mj}^u, 0, L_0) - \xi_{m1}^d g_{10}^d \mathcal{I}(-\lambda_{m1}^d, L_0, L_1) - \sum_{j=1}^4 [\mathcal{L}_{h,mj}^u(L_0) - \mathcal{L}_{h,mj}^d(L_0)] \end{bmatrix} \tag{5.21}$$

The complete solution requires 4 additional relations concerning  $c_{m2}^u$ ,  $c_{m3}^u$ ,  $c_{m4}^u$ , and  $c_{m1}^d$  (e.g. free meandering conditions at the extremes, thus they are all zero).

### SUPER-SUPER case

The scenario in which both the upstream and the downstream subreaches are super-resonant is here considered. Both subreaches require 3 boundary conditions at their

downstream ends, while the remaining one is applied at their upstream end. Since the upstream subreach shares its downstream end with the upstream end of the downstream subreach, the following conditions occur:

- 1 boundary conditions ( $u_m|_0$ ) at the upstream end of the upstream subreach;
- 4 internal conditions (eq. 5.12) at the singular section required by the continuity of the perturbed flow;
- 3 boundary conditions ( $v_m|_{L_1}$ ,  $d_m|_{L_1}$ ,  $h_m|_{L_1}$ ) at the downstream end of the upstream subreach.

The curvature-driven flow field for the upstream and the downstream subreaches then reads:

$$\begin{aligned} \mathcal{Q}^u(s) = & -\hat{A}_m \sum_{j=1}^3 \mathcal{T}_{mj}^u g_{j0}^u \mathcal{I}(-\lambda_{mj}^u, s, L_0) + \hat{A}_m \mathcal{T}_{m4}^u g_{40}^u \mathcal{I}(\lambda_{m4}^u, 0, s) + \\ & + \sum_{j=1}^3 \mathcal{T}_{mj}^u c_{mj}^u e^{-\lambda_{mj}^u(L_0-s)} + \mathcal{T}_{m4}^u c_{m4}^u e^{\lambda_{m4}^u s} + \hat{A}_m \sum_{j=1}^4 \mathcal{L}_{mj}^u(s) \end{aligned} \quad (5.22)$$

$$\begin{aligned} \mathcal{Q}^d(s) = & -\hat{A}_m \sum_{j=1}^3 \mathcal{T}_{mj}^d g_{j0}^d \mathcal{I}(-\lambda_{mj}^d, s, L_1) + \hat{A}_m \mathcal{T}_{m4}^d g_{40}^d \mathcal{I}(\lambda_{m4}^d, L_0, s) + \\ & + \sum_{j=1}^3 \mathcal{T}_{mj}^d c_{mj}^d e^{-\lambda_{mj}^d(L_1-s)} + \mathcal{T}_{m4}^d c_{m4}^d e^{\lambda_{m4}^d(s-L_0)} + \hat{A}_m \sum_{j=1}^4 \mathcal{L}_{mj}^d(s) \end{aligned} \quad (5.23)$$

Evaluating the previous equations at  $s = L_0$ :

$$\begin{aligned} \mathcal{Q}^u(L_0) = & -\hat{A}_m \sum_{j=1}^3 \mathcal{T}_{mj}^u g_{j0}^u \mathcal{I}(-\lambda_{mj}^u, L_0, L_0) + \hat{A}_m \mathcal{T}_{m4}^u g_{40}^u \mathcal{I}(\lambda_{m4}^u, 0, L_0) + \\ & + \sum_{j=1}^3 \mathcal{T}_{mj}^u c_{mj}^u e^{-\lambda_{mj}^u(L_0-L_0)} + \mathcal{T}_{m4}^u c_{m4}^u e^{\lambda_{m4}^u L_0} + \hat{A}_m \sum_{j=1}^4 \mathcal{L}_{mj}^u(L_0) \end{aligned} \quad (5.24)$$

$$\begin{aligned} \mathcal{Q}^d(L_0) = & -\hat{A}_m \sum_{j=1}^3 \mathcal{T}_{mj}^d g_{j0}^d \mathcal{I}(-\lambda_{mj}^d, L_0, L_1) + \hat{A}_m \mathcal{T}_{m4}^d g_{40}^d \mathcal{I}(\lambda_{m4}^d, L_0, L_0) + \\ & + \sum_{j=1}^3 \mathcal{T}_{mj}^d c_{mj}^d e^{-\lambda_{mj}^d(L_1-L_0)} + \mathcal{T}_{m4}^d c_{m4}^d e^{\lambda_{m4}^d(L_0-L_0)} + \hat{A}_m \sum_{j=1}^4 \mathcal{L}_{mj}^d(L_0) \end{aligned} \quad (5.25)$$

and, removing the terms equal to zero:

$$\begin{aligned}\mathcal{Q}^u(L_0) &= \hat{A}_m \mathcal{T}_{m4}^u g_{40}^u \mathcal{I}(\lambda_{m4}^u, 0, L_0) + \\ &+ \sum_{j=1}^3 \mathcal{T}_{mj}^u c_{mj}^u + \mathcal{T}_{m4}^u c_{m4}^u e^{\lambda_{m4}^u L_0} + \hat{A}_m \sum_{j=1}^4 \mathcal{L}_{mj}^u(L_0)\end{aligned}\quad (5.26)$$

$$\begin{aligned}\mathcal{Q}^d(L_0) &= -\hat{A}_m \sum_{j=1}^3 \mathcal{T}_{mj}^d g_{j0}^d \mathcal{I}(-\lambda_{mj}^d, L_0, L_1) + \\ &+ \sum_{j=1}^3 \mathcal{T}_{mj}^d c_{mj}^d e^{-\lambda_{mj}^d(L_1-L_0)} + \mathcal{T}_{m4}^d c_{m4}^d + \hat{A}_m \sum_{j=1}^4 \mathcal{L}_{mj}^d(L_0)\end{aligned}\quad (5.27)$$

Assuming that  $L_0$  and  $L_1 - L_0$  are sufficiently large leads to a rapid decay of the exponential terms such that they may be neglected (Figure 5.2). Subtracting these relations and rearranging in order to obtain the explicit relations to be applied at the singularity, the resulting equation reads:

$$\begin{aligned}&\mathcal{T}_{m1}^u c_{m1}^u + \mathcal{T}_{m2}^u c_{m2}^u + \mathcal{T}_{m3}^u c_{m3}^u - \mathcal{T}_{m4}^d c_{m4}^d = \\ &= -\hat{A}_m \left\{ \mathcal{T}_{m4}^u g_{40}^u \mathcal{I}(\lambda_{m4}^u, 0, L_0) + \sum_{j=1}^3 \mathcal{T}_{mj}^d g_{j0}^d \mathcal{I}(-\lambda_{mj}^d, L_0, L_1) + \right. \\ &\quad \left. + \sum_{j=1}^4 [\mathcal{L}_{mj}^u(L_0) - \mathcal{L}_{mj}^d(L_0)] \right\}\end{aligned}\quad (5.28)$$

This equation provides a linear system of 4 equations in the 4 variables  $c_{m1}^u, c_{m2}^u, c_{m3}^u$  that, in matrix form, reads  $Ac = B$ , where:

$$A = \frac{1}{\hat{A}_m} \begin{bmatrix} 1 & 1 & 1 & -1 \\ \phi_{m1}^u & \phi_{m2}^u & \phi_{m3}^u & -\phi_{m4}^d \\ \delta_{m1}^u & \delta_{m2}^u & \delta_{m3}^u & -\delta_{m4}^d \\ \xi_{m1}^u & \xi_{m2}^u & \xi_{m3}^u & -\xi_{m4}^d \end{bmatrix} \quad c = \begin{bmatrix} c_{m1}^u \\ c_{m2}^u \\ c_{m3}^u \\ c_{m4}^d \end{bmatrix} \quad (5.29)$$

$$B = \begin{bmatrix} -g_{40}^u \mathcal{I}(\lambda_{m4}^u, 0, L_0) - \sum_{j=1}^3 g_{j0}^d \mathcal{I}(-\lambda_{mj}^d, L_0, L_1) - \sum_{j=1}^4 [\mathcal{L}_{u,mj}^u(L_0) - \mathcal{L}_{u,mj}^d(L_0)] \\ -\phi_{m4}^u g_{40}^u \mathcal{I}(\lambda_{m4}^u, 0, L_0) - \sum_{j=1}^3 \phi_{mj}^d g_{j0}^d \mathcal{I}(-\lambda_{mj}^d, L_0, L_1) - \sum_{j=1}^4 [\mathcal{L}_{v,mj}^u(L_0) - \mathcal{L}_{v,mj}^d(L_0)] \\ -\delta_{m4}^u g_{40}^u \mathcal{I}(\lambda_{m4}^u, 0, L_0) - \sum_{j=1}^3 \delta_{mj}^d g_{j0}^d \mathcal{I}(-\lambda_{mj}^d, L_0, L_1) - \sum_{j=1}^4 [\mathcal{L}_{d,mj}^u(L_0) - \mathcal{L}_{d,mj}^d(L_0)] \\ -\xi_{m4}^u g_{40}^u \mathcal{I}(\lambda_{m4}^u, 0, L_0) - \sum_{j=1}^3 \xi_{mj}^d g_{j0}^d \mathcal{I}(-\lambda_{mj}^d, L_0, L_1) - \sum_{j=1}^4 [\mathcal{L}_{h,mj}^u(L_0) - \mathcal{L}_{h,mj}^d(L_0)] \end{bmatrix} \quad (5.30)$$

The complete solution requires 4 additional relations concerning  $c_{m2}^d$ ,  $c_{m3}^d$ ,  $c_{m4}^d$ , and  $c_{m4}^u$ .

### SUB-SUPER case

The scenario in which the upstream subreach is subresonant while the downstream subreach is superresonant is here considered. The first requires 3 boundary conditions at its upstream end and the remaining one at its downstream end, while the latter requires one boundary condition at its upstream end and the remaining 3 at its downstream end. Since the upstream subreach shares its downstream end with the upstream end of the downstream subreach, the following conditions occur:

- 3 boundary conditions ( $v_m|_0$ ,  $d_m|_0$ ,  $h_m|_0$ ) at the upstream end of the upstream subreach;
- 2 internal conditions (eq. 5.12) at the singular section required by the continuity of the perturbed flow;
- 3 boundary conditions ( $v_m|_{L_1}$ ,  $d_m|_{L_1}$ ,  $h_m|_{L_1}$ ) at the downstream end of the upstream subreach.

The two required conditions at the shared point  $s = L_0$  are given by the continuity of two out of four perturbation components, namely arbitrarily the longitudinal perturbation velocity and the continuity of the transverse perturbation velocity.

Hence, referring to the subresonant upstream subreach:

$$\begin{aligned}
u_m^u(L_0) &= -\hat{A}_m g_{10}^u \mathcal{I}(-\lambda_{m1}, L_0, L_0) + \hat{A}_m \sum_{j=2}^4 g_{j0}^u \mathcal{I}(\lambda_{mj}^u, 0, L_0) + \\
&\quad + c_{m1}^u + \sum_{j=2}^4 c_{mj}^u e^{\lambda_{mj}^u L_0} + \hat{A}_m \sum_{j=1}^4 \mathcal{L}_{u,mj}^u(L_0)
\end{aligned} \tag{5.31}$$

$$\begin{aligned}
v_m^u(L_0) &= -\hat{A}_m g_{10}^u \phi_{m1}^u \mathcal{I}(-\lambda_{m1}, L_0, L_0) + \hat{A}_m \sum_{j=2}^4 g_{j0}^u \phi_{mj}^u \mathcal{I}(\lambda_{mj}^u, 0, L_0) + \\
&\quad + \phi_{m1}^u c_{m1}^u + \sum_{j=2}^4 \phi_{mj}^u c_{mj}^u e^{\lambda_{mj}^u L_0} + \hat{A}_m \sum_{j=1}^4 \mathcal{L}_{u,mj}^u(L_0)
\end{aligned} \tag{5.32}$$

Referring to the superresonant downstream subreach:

$$\begin{aligned}
u_m^d(L_0) &= -\hat{A}_m \sum_{j=1}^3 g_{j0}^d \mathcal{I}(-\lambda_{mj}, L_0, L_1) + \hat{A}_m g_{40}^d \mathcal{I}(\lambda_{m4}, L_0, L_0) + \\
&\quad + \sum_{j=1}^3 c_{mj}^d e^{-\lambda_{mj}^d (L_1 - L_0)} + c_{m4}^d + \hat{A}_m \sum_{j=1}^4 \mathcal{L}_{u,mj}^d(L_0)
\end{aligned} \tag{5.33}$$

$$\begin{aligned}
v_m^d(L_0) &= -\hat{A}_m \sum_{j=1}^3 g_{j0}^d \phi_{mj}^d \mathcal{I}(-\lambda_{mj}, L_0, L_1) + \hat{A}_m g_{40}^d \phi_{m4}^d \mathcal{I}(\lambda_{m4}, L_0, L_0) + \\
&\quad + \sum_{j=1}^3 \phi_{mj}^d c_{mj}^d e^{-\lambda_{mj}^d (L_1 - L_0)} + \phi_{m4}^d c_{m4}^d + \hat{A}_m \sum_{j=1}^4 \mathcal{L}_{u,mj}^d(L_0)
\end{aligned} \tag{5.34}$$

Assuming that  $L_0$  and  $L_1 - L_0$  are sufficiently large leads to a rapid decay of the exponential terms such that they may be neglected (Figure 5.2). As a consequence, the problem simplifies as follows:

$$u_m^u(L_0) = \hat{A}_m \sum_{j=2}^4 g_{j0}^u \mathcal{I}(\lambda_{mj}^u, 0, L_0) + c_{m1}^u + \hat{A}_m \sum_{j=1}^4 \mathcal{L}_{u,mj}^u(L_0) \tag{5.35}$$

$$v_m^u(L_0) = \hat{A}_m \sum_{j=2}^4 g_{j0}^u \phi_{mj}^u \mathcal{I}(\lambda_{mj}^u, 0, L_0) + \phi_{m1}^u c_{m1}^u + \hat{A}_m \sum_{j=1}^4 \mathcal{L}_{u,mj}^u(L_0) \tag{5.36}$$

$$u_m^d(L_0) = -\hat{A}_m \sum_{j=1}^3 g_{j0}^d \mathcal{I}(-\lambda_{mj}, L_0, L_1) + c_{m4}^d + \hat{A}_m \sum_{j=1}^4 \mathcal{L}_{u,mj}^d(L_0) \tag{5.37}$$

$$v_m^d(L_0) = -\hat{A}_m \sum_{j=1}^3 g_{j0}^d \phi_{mj}^d \mathcal{I}(-\lambda_{mj}, L_0, L_1) + \phi_{m4}^d c_{m4}^d + \hat{A}_m \sum_{j=1}^4 \mathcal{L}_{u,mj}^d(L_0) \tag{5.38}$$

Finally, matching the two velocity components:

$$\begin{aligned}
c_{m1}^u - c_{m4}^d &= -\hat{A}_m \sum_{j=2}^4 g_{j0}^u \mathcal{I}(\lambda_{mj}^u, 0, L_0) - \hat{A}_m \sum_{j=1}^3 g_{j0}^d \mathcal{I}(-\lambda_{mj}, L_0, L_1) + \\
&\quad -\hat{A}_m \sum_{j=1}^4 \left[ \mathcal{L}_{u,mj}^u(L_0) - \mathcal{L}_{u,mj}^d(L_0) \right]
\end{aligned} \tag{5.39}$$

$$\begin{aligned}
\phi_{m1}^u c_{m1}^u - \phi_{m4}^d c_{m4}^d &= -\hat{A}_m \sum_{j=2}^4 g_{j0}^u \phi_{mj}^u \mathcal{I}(\lambda_{mj}^u, 0, L_0) - \hat{A}_m \sum_{j=1}^3 g_{j0}^d \phi_{mj}^d \mathcal{I}(-\lambda_{mj}, L_0, L_1) + \\
&\quad -\hat{A}_m \sum_{j=1}^4 \left[ \mathcal{L}_{u,mj}^u(L_0) - \mathcal{L}_{u,mj}^d(L_0) \right]
\end{aligned} \tag{5.40}$$

The previous equation constitutes a linear system of 2 equations in the 2 variables  $c_{m1}^u$  and  $c_{m4}^d$ , that, in matrix form, reads  $Ac = B$ , where:

$$A = \frac{1}{\hat{A}_m} \begin{bmatrix} 1 & -1 \\ \phi_{m1}^u & -\phi_{m4}^d \end{bmatrix} \quad c = \begin{bmatrix} c_{m1}^u \\ c_{m4}^d \end{bmatrix} \tag{5.41}$$

$$B = \begin{bmatrix} -\sum_{j=2}^4 g_{j0}^u \mathcal{I}(\lambda_{mj}^u, 0, L_0) - \sum_{j=1}^3 g_{j0}^d \mathcal{I}(-\lambda_{mj}, L_0, L_1) + \\ \quad -\sum_{j=1}^4 \left[ \mathcal{L}_{u,mj}^u(L_0) - \mathcal{L}_{u,mj}^d(L_0) \right] \\ -\sum_{j=2}^4 g_{j0}^u \phi_{mj}^u \mathcal{I}(\lambda_{mj}^u, 0, L_0) - \sum_{j=1}^3 g_{j0}^d \phi_{mj}^d \mathcal{I}(-\lambda_{mj}, L_0, L_1) + \\ \quad -\sum_{j=1}^4 \left[ \mathcal{L}_{u,mj}^u(L_0) - \mathcal{L}_{u,mj}^d(L_0) \right] \end{bmatrix} \tag{5.42}$$

### **SUPER-SUB case**

The scenario in which the upstream subreach is superresonant while the downstream subreach is subresonant is here considered. The first requires one boundary condition at its upstream end and the remaining 3 at its downstream end, while the latter requires 3 boundary conditions at its upstream end and the remaining one at its downstream end. Since the upstream subreach shares its downstream end with the upstream end of the downstream subreach, the following conditions may be considered:

- 1 boundary conditions ( $u_m|_0$ ) at the upstream end of the upstream subreach ;
- 6 internal conditions (eq. 5.12) at the singular section required by the continuity of the perturbed flow;
- 1 boundary condition ( $u_m|_{L_1}$ ) at the downstream end of the upstream subreach.

Referring to (5.9) for the curvature-driven flow field in the upstream subreach and to (5.8) for the curvature-driven flow field in the downstream subreach, respectively:

$$\begin{aligned} \mathcal{Q}^u(s) = & -\hat{A}_m \sum_{j=1}^3 \mathcal{T}_{mj} \mathcal{I}(-\lambda_{mj}, s, L_0) + \hat{A}_m \mathcal{T}_{m4} \mathcal{I}(\lambda_{m4}, 0, s) + \\ & + \sum_{j=1}^3 \mathcal{T}_{mj} c_{mj} e^{-\lambda_{mj}(L_0-s)} + \mathcal{T}_{m4} c_{m4} e^{\lambda_{m4}s} + \hat{A}_m \sum_{j=1}^4 \mathcal{L}_{mj}(s) \end{aligned} \quad (5.43)$$

$$\begin{aligned} \mathcal{Q}^d(s) = & -\hat{A}_m \mathcal{T}_{m1} \mathcal{I}(-\lambda_{m1}, s, L_1) + \hat{A}_m \sum_{j=2}^4 \mathcal{T}_{mj} \mathcal{I}(\lambda_{mj}, L_0, s) + \\ & + \mathcal{T}_{m1} c_{m1} e^{-\lambda_{m1}(L_1-s)} + \sum_{j=2}^4 \mathcal{T}_{mj} c_{mj} e^{\lambda_{mj}(s-L_0)} + \hat{A}_m \sum_{j=1}^4 \mathcal{L}_{mj}(s) \end{aligned} \quad (5.44)$$

Evaluating the previous equations at  $s = L_0$ :

$$\begin{aligned} \mathcal{Q}^u(L_0) = & -\hat{A}_m \sum_{j=1}^3 \mathcal{T}_{mj}^u \mathcal{I}(-\lambda_{mj}^u, L_0, L_0) + \hat{A}_m \mathcal{T}_{m4}^u \mathcal{I}(\lambda_{m4}^u, 0, L_0) + \\ & + \sum_{j=1}^3 \mathcal{T}_{mj}^u c_{mj}^u e^{-\lambda_{mj}^u(L_0-L_0)} + \mathcal{T}_{m4}^u c_{m4}^u e^{\lambda_{m4}^u L_0} + \hat{A}_m \sum_{j=1}^4 \mathcal{L}_{mj}^u(L_0) \end{aligned} \quad (5.45)$$

$$\begin{aligned} \mathcal{Q}^d(L_0) = & -\hat{A}_m \mathcal{T}_{m1}^d \mathcal{I}(-\lambda_{m1}^d, L_0, L_1) + \hat{A}_m \sum_{j=2}^4 \mathcal{T}_{mj}^d \mathcal{I}(\lambda_{mj}^d, L_0, L_0) + \\ & + \mathcal{T}_{m1}^d c_{m1}^d e^{-\lambda_{m1}^d(L_1-L_0)} + \sum_{j=2}^4 \mathcal{T}_{mj}^d c_{mj}^d e^{\lambda_{mj}^d(L_0-L_0)} + \hat{A}_m \sum_{j=1}^4 \mathcal{L}_{mj}^d(L_0) \end{aligned} \quad (5.46)$$



Removing the terms equal to zero:

$$\begin{aligned}\mathcal{Q}^u(L_0) &= \hat{A}_m \hat{A}_m \mathcal{T}_{m4}^u \mathcal{I}(\lambda_{m4}^u, 0, L_0) + \sum_{j=1}^3 \mathcal{T}_{mj}^u c_{mj}^u + \mathcal{T}_{m4}^u c_{m4}^u e^{\lambda_{m4}^u L_0} + \\ &\quad + \hat{A}_m \sum_{j=1}^4 \mathcal{L}_{mj}^u(L_0)\end{aligned}\quad (5.47)$$

$$\begin{aligned}\mathcal{Q}^d(L_0) &= -\hat{A}_m \mathcal{T}_{m1}^d \mathcal{I}(-\lambda_{m1}^d, L_0, L_1) + \mathcal{T}_{m1}^d c_{m1}^d e^{-\lambda_{m1}^d(L_1-L_0)} + \sum_{j=2}^4 \mathcal{T}_{mj}^d c_{mj}^d + \\ &\quad + \hat{A}_m \sum_{j=1}^4 \mathcal{L}_{mj}^d(L_0)\end{aligned}\quad (5.48)$$

Assuming that  $L_0$  and  $L_1 - L_0$  are sufficiently large leads to a rapid decay of the exponential terms such that they may be neglected (Figure 5.2). As a consequence, the problem simplifies as follows:

$$\begin{aligned}\mathcal{T}_{m1}^u c_{m1}^u + \mathcal{T}_{m2}^u c_{m2}^u + \mathcal{T}_{m3}^u c_{m3}^u - \mathcal{T}_{m2}^d c_{m2}^d - \mathcal{T}_{m3}^d c_{m3}^d - \mathcal{T}_{m4}^d c_{m4}^d &= \\ &= -\hat{A}_m \mathcal{T}_{m4}^u \mathcal{I}(\lambda_{m4}^u, 0, L_0) - \hat{A}_m \mathcal{T}_{m1}^d \mathcal{I}(-\lambda_{m1}^d, L_0, L_1) + \\ &\quad - \hat{A}_m \sum_{j=1}^4 \left[ \mathcal{L}_{mj}^u(L_0) - \mathcal{L}_{mj}^d(L_0) \right]\end{aligned}\quad (5.49)$$

The previous equation constitutes a linear system of 4 equations in the 6 variables  $c_{m1}^u$ ,  $c_{m2}^u$ ,  $c_{m3}^u$ ,  $c_{m2}^d$ ,  $c_{m3}^d$ , and  $c_{m4}^d$ . In order to overcome the indefiniteness, the assumption of the upstream and downstream most contributing coefficients, in terms of their respective eigenvalues, are assumed equal to zero, i.e.  $c_{m1}^u = 0$  and  $c_{m4}^d = 0$ . The matrix form reads  $Ac = B$ , where:

$$A = \frac{1}{\hat{A}_m} \begin{bmatrix} 1 & 1 & -1 & -1 \\ \phi_{m2}^u & \phi_{m3}^u & -\phi_{m2}^d & -\phi_{m3}^d \\ \delta_{m2}^u & \delta_{m3}^u & -\delta_{m2}^d & -\delta_{m3}^d \\ \xi_{m2}^u & \xi_{m3}^u & -\xi_{m2}^d & -\xi_{m3}^d \end{bmatrix} \quad c = \begin{bmatrix} c_{m2}^u \\ c_{m3}^u \\ c_{m2}^d \\ c_{m3}^d \end{bmatrix} \quad (5.50)$$

$$B = \begin{bmatrix} -\mathcal{I}(\lambda_{m4}^u, 0, L_0) - \mathcal{I}(-\lambda_{m1}^d, L_0, L_1) - \sum_{j=1}^4 [\mathcal{L}_{u,mj}^u(L_0) - \mathcal{L}_{u,mj}^d(L_0)] \\ -\phi_{m4}^u \mathcal{I}(\lambda_{m4}^u, 0, L_0) - \phi_{m1}^d \mathcal{I}(-\lambda_{m1}^d, L_0, L_1) - \sum_{j=1}^4 [\mathcal{L}_{v,mj}^u(L_0) - \mathcal{L}_{v,mj}^d(L_0)] \\ -\delta_{m4}^u \mathcal{I}(\lambda_{m4}^u, 0, L_0) - \delta_{m1}^d \mathcal{I}(-\lambda_{m1}^d, L_0, L_1) - \sum_{j=1}^4 [\mathcal{L}_{d,mj}^u(L_0) - \mathcal{L}_{d,mj}^d(L_0)] \\ -\xi_{m4}^u \mathcal{I}(\lambda_{m4}^u, 0, L_0) - \xi_{m1}^d \mathcal{I}(-\lambda_{m1}^d, L_0, L_1) - \sum_{j=1}^4 [\mathcal{L}_{h,mj}^u(L_0) - \mathcal{L}_{h,mj}^d(L_0)] \end{bmatrix} \quad (5.51)$$

The complete solution requires 2 additional relations concerning  $c_{m4}^u$  and  $c_{m1}^d$  (e.g. full free-meandering conditions), beyond the assumption a priori that  $c_{m1}^u = 0$  and  $c_{m4}^d = 0$ .

## Summary

The Figure 5.3 shows a framework of the four different resonance cases rising from the coupling of two meandering subreaches and mathematically debated above. Each subreach (i.e. upstream of downstream with respect to the internal boundary condition) is affected by four terms related to the boundary conditions, either internal or external.

The first case, i.e. SUB-SUB case, corresponds to the coupling of two subreaches which are both subresonant. As a consequence, the internal boundary conditions determines one term affecting the upstream subreach and three terms affecting the downstream subreach. The remaining terms must be externally imposed. On the contrary, the SUPER-SUPER case considers two superresonant subreaches, thus the internal boundary conditions determines three terms in the upstream subreach and one term in the downstream subreach. The mixed cases sets either one or two terms per subreach, respectively in the SUB-SUPER case and in the SUPER-SUB case. In general, the combination of the two resonance conditions leads to which and how many coefficients  $c_{mj}^i$  (where  $i$  may be  $u$  if they are related to the upstream subreach or  $d$  if they are related to the downstream subreach) are driven by the singular section.

It is noteworthy that the effect of the boundary conditions driven by  $c_{mj}^i$  decays exponentially (Figure 5.2) with the distance computed from the reach end where they establish, either an external end or the internal boundary conditions. As mentioned above, if  $\lambda_{mj} < 0$  the boundary condition applies in the upstream end of the considered subreach and propagates downstream, whereas if  $\lambda_{mj} > 0$  the exponent of the expo-

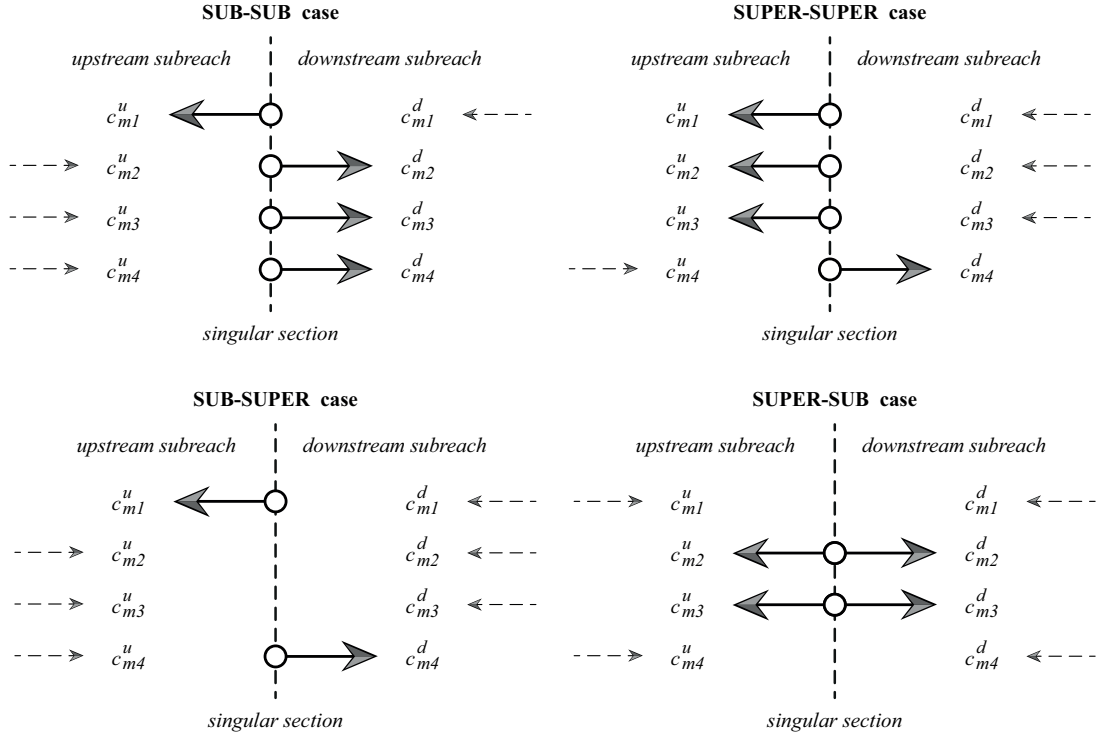


Figure 5.3: Framework of the four different resonance cases which rise from the coupling of two subdomains: SUB-SUB case (top left panel), SUPER-SUPER case (top right panel), SUB-SUPER case (bottom left panel), and SUPER-SUB case (bottom right panel). Each of the four coefficients related to either the upstream or the downstream subreach is marked by an arrow showing the direction of propagation of its information. A solid arrow originating from white circle means that the related coefficient  $c_{m,j}^i$  is determined by the internal boundary condition. On the contrary, a dashed arrow means that the related coefficient must be externally imposed in the end which is not the singular section.

nential term is considered anyway negative and the boundary condition moves from the downstream end toward upstream. In general, assuming a numerical tolerance  $\varepsilon$  below which the the exponential term may be considered as negligible, the threshold equation for the generic coefficient  $c_{mj}^i$  is as follows:

$$e^{-|\lambda_{mj}|L} = \varepsilon \quad (5.52)$$

Thus, the maximum dimensionless distance  $L = L^*/B_0^*$  (i.e. scaled by the half width  $B_0^*$ ) along the reach affected by a certain boundary condition and computed from the end where the boundary condition is applied reads:

$$L = \frac{L^*}{B_0^*} = -\frac{\ln \varepsilon}{|\lambda_{mj}|} \quad (5.53)$$

The length of the effect of the boundary conditions, either internal or external, depends on the values of the respective characteristic exponent  $\lambda_{mj}$  and on the adopted numerical tolerance  $\varepsilon$ .

## 5.2 Application to the Mississippi River

The Mississippi River has the third largest drainage area of all world rivers, extending over 12 % of North America and 45 % of the contiguous United States (Nitttrouer et al., 2011). For the purposes of this work, the part of the Mississippi comprised from Memphis (Tennessee, US) to Natchez (Mississippi, US) is considered. The goal is to examine the effect given by the confluence of the Arkansas River in correspondence to Arkansas Post, at the border between Arkansas and Mississippi, US (Figure 5.4).

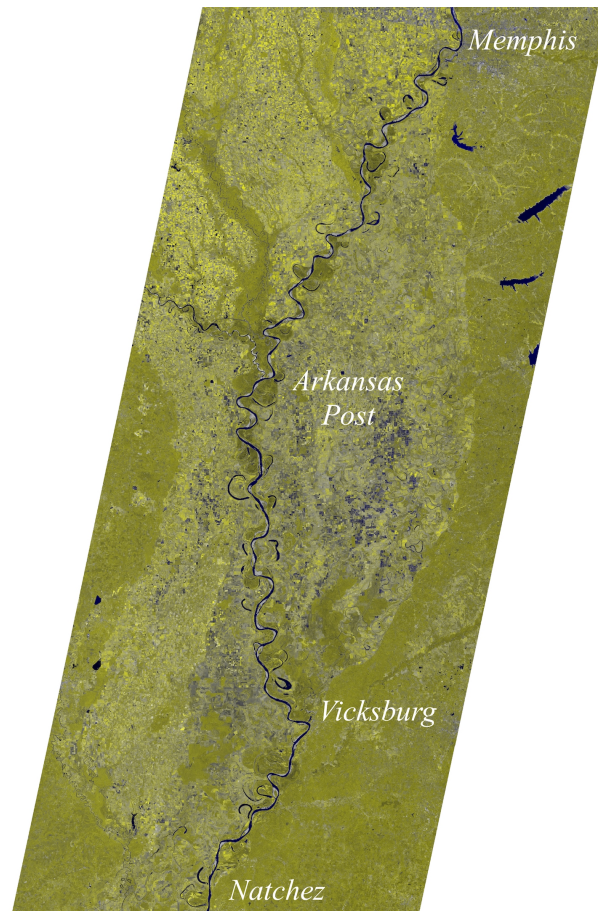


Figure 5.4: Composition of Landsat images of the Mississippi River between Memphis, Tennessee (US) and Natchez, Mississippi (US) (source: <http://earthexplorer.usgs.gov>). Cartesian distance between the upstream and the downstream end is about 410 km, while the intrinsic length is about 600 km. River flows from the top to the bottom of the image.

The intrinsic length of the upstream Mississippi subreach up to the tributary confluence is about 250 km, while the intrinsic length of the downstream subreach from the tributary confluence to the downstream end is about 350 km. The total length of the investigated river planform turns out to be about 600 km. Through the Ruler Tools of the software Google Earth Pro, which handle both planimetric lengths and local elevations of the terrain, the mean bed slope of the Mississippi is evaluated to be  $S \simeq 10^{-4}$  for both the upstream and the downstream subreaches. On the basis of Landsat images (source: <http://earthexplorer.usgs.gov>), the average widths of the two subreaches are  $2B_0^{*u} = 1000$  m and  $2B_0^{*d} = 950$  m respectively. Moreover, the width distribution lies in the range  $0.30 < (B^*/B_0^*)^u < 2.20$  in the upstream subreach, while in the range  $0.40 < (B^*/B_0^*)^d < 2.15$  in the downstream subreach.

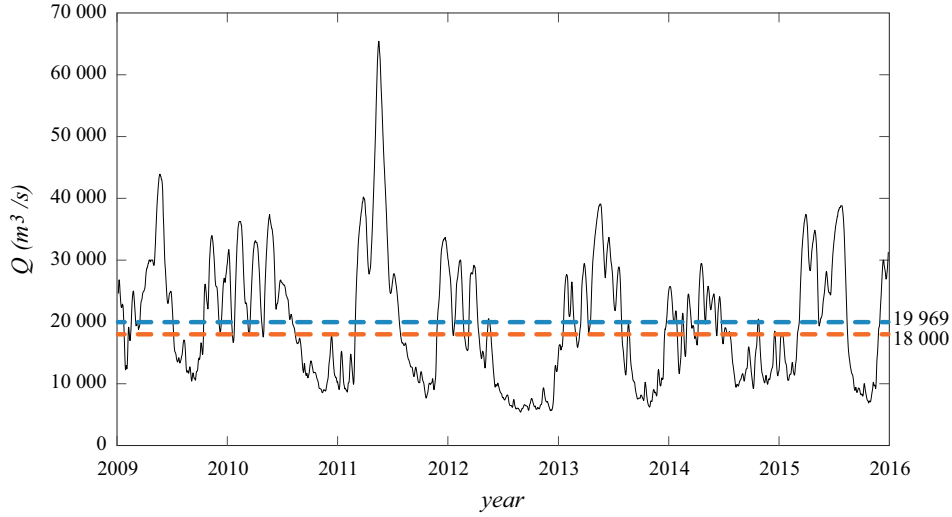


Figure 5.5: Average daily discharge of Mississippi River at Vicksburg gauge station (USGS 07289000), from 2009 to 2015. The blue dashed line represents the average value, i.e.  $\sim 20000$  m<sup>3</sup>/s, while the orange dashed line represents a value corresponding to the 90 % of the average value, i.e.  $\sim 18000$  m<sup>3</sup>/s.

The mean daily discharge of the Mississippi River is available from the gauge station USGS 07289000 at Vicksburg, Mississippi, US, located about 250 km downstream of the Arkansas River confluence. The temporal series from 2009 to 2015 is represented in Figure 5.5. The trend shows a general concentration of floods in the first half of each year, followed by a reduction of discharge in the second parts. The average value reads  $\sim 20000$  m<sup>3</sup>/s, however a 10 % reduced value will be considered as reference, i.e.

$Q^d \sim 18000 \text{ m}^3/\text{s}$ . This choice ensures that the daily discharges are generally above this threshold in winter and spring and below this threshold in summer and fall. Thus, discharge is considered constant for the entire year and equal to the diminished value.

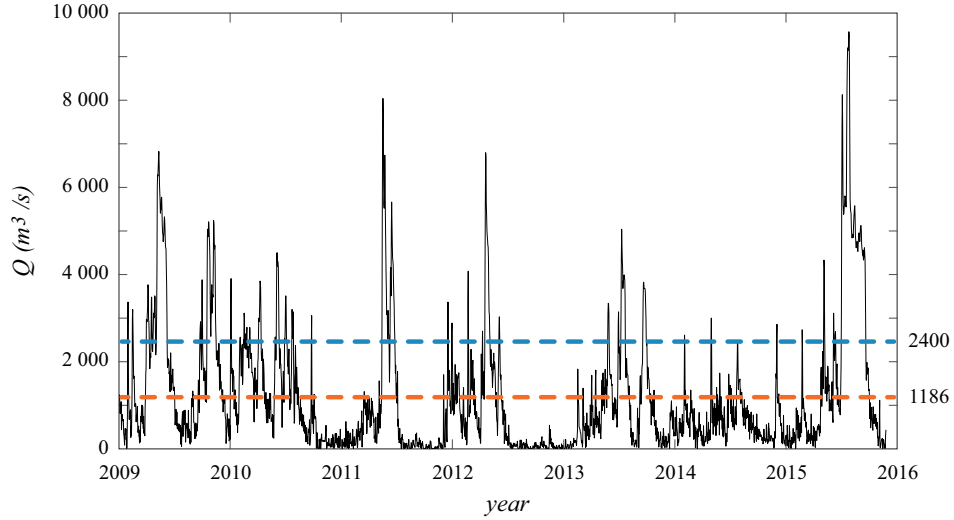


Figure 5.6: Average daily discharge of Arkansas River at Murray Dam gauge station near Little Rock (USGS 07263450), from 2009 to 2015. The blue dashed line represents the average value, i.e.  $\sim 1200 \text{ m}^3/\text{s}$ , while the orange dashed represents a value corresponding to the double of the average value, i.e.  $\sim 2400 \text{ m}^3/\text{s}$ .

The mean daily discharge of the Arkansas River is available from the gauge station USGS 07263450 at Murray Dam near Little Rock, Arkansas, US, located about 100 km upstream of the confluence into the Mississippi River. The temporal series from 2009 to 2015 is represented in Figure 5.6. The trend shows a relatively large variability, with some distinguishable peaks in the summer periods. The average value reads  $\Delta Q \sim 1200 \text{ m}^3/\text{s}$ .

The discharge in the subreach of Mississippi River upstream of the confluence with the Arkansas River thus reads  $Q^u = Q^d - \Delta Q = 16800 \text{ m}^3/\text{s}$ , as given by the first of conditions (5.1). Assuming a Strickler coefficient  $K_s = 30 \text{ m}^{1/3}/\text{s}$  for both subreaches, the flow depths turn out to read  $D_0^{*u} = 11.20 \text{ m}$  and  $D_0^{*d} = 12.00 \text{ m}$  for the upstream and the downstream subreaches, respectively.

Finally, the characteristic grain size of the sediment forming the river bed is required in order to complete the information of the set of governing equations. The grain size distribution is available for both the subreaches from the measurement campaign

carried out by Nordin and Queen (1992). In the upstream subreach, the major part of the sediment ranges from medium to medium-coarse sand, thus a characteristic mean diameter  $d_s^{*u} = 0.5$  mm is assigned; in the downstream subreach a characteristic mean diameter  $d_s^{*d} = 0.4$  mm is assigned, as the major part of the sediment lies in the medium sand range.

The above described scenario, with the assumption of uniform flow, is hereafter referred to as RUN-0 and considered as the reference scenario.

Two additional possible scenarios are now introduced, namely RUN-1 and RUN-2. The first additional scenario is characterized by a discharge  $\Delta Q = 2400$  m<sup>3</sup>/s within the Arkansas River, doubled with respect to the reference case (Figure 5.6). As a consequence, the discharge in the downstream subreach of the Mississippi reads  $Q^d = 19200$  m<sup>3</sup>/s, and the depth  $D_0^{*d} = 12.50$  m. The second additional scenario considers the Arkansas River as not bringing any discharge, i.e.  $\Delta Q = 0$  m<sup>3</sup>/s, therefore the discharge in the downstream Mississippi subreach turns out to be  $Q^d = 16800$  m<sup>3</sup>/s, and the depth  $D_0^{*d} = 11.55$  m.

Finally, a third further scenario, hereafter referred to as RUN-3, assumes a stronger downstream sediment fining in the River Mississippi. As confirmed by the measurements of Nordin and Queen (1992), the distribution of the grain sizes tends toward finer and finer sediment sizes moving downstream subreach, because of the typical concavity of the longitudinal profile of sand-bed rivers which decreases the suspended load (Wright and Parker, 2005; Frings, 2008). Hence, a characteristic grain size  $d_s^{*d} = 0.2$  mm is assumed in the downstream subreach, keeping all of the other quantities equal to the ones related to RUN-0.

The various sets of input parameters are summarized in the Table 5.1.

The implemented numerical model follows the framework outlined in Chapter 2, suitably modified by inserting the mathematical extension derived in Section 5.1 in order to deal with the coupling of two meandering subdomain. The friction coefficient is derived from the assumed Strickler coefficient  $K_s$  as:

$$C_f = \frac{g}{K_s^2 D_0^{*1/3}} \quad (5.54)$$

where  $g$  is the gravity acceleration, and  $D_0^*$  is the uniform flow depth of the considered subreach, either upstream or downstream of the confluence with Arkansas River. The sediment transport intensity is computed through the total load predictor of Engelund and Hansen (1967).



Table 5.1: Sets of input parameters considered for the simulation of the Mississippi River migration in the presence of the confluence with the Arkansas River confluence. The upstream ( $u$ ) and downstream ( $d$ ) subreaches are explicitly accounted for. Symbols are as follows:  $Q$  is the discharge,  $2B_0^*$  is the cross section width,  $D_0^*$  the flow depth,  $S$  is the bed slope, and  $d_s^*$  is the characteristic grain size. Moreover,  $\beta = B_0^*/D_0^*$  is the aspect ratio,  $\tau_* = D_0^*S/\Delta d_s^*$  is the Shields number (with  $\Delta \simeq 1.65$  the submerged specific gravity of the sediment), and  $d_s = d_s^*/D_0^*$  is the dimensionless grain size.

Simulation	RUN-0		RUN-1		RUN-2		RUN-3	
Subreach	$u$	$d$	$u$	$d$	$u$	$d$	$u$	$d$
$Q$ (m <sup>3</sup> /s)	16800	18000	16800	19200	16800	16800	16800	18000
$2B_0^*$ (m)	1000	950	1000	950	1000	950	1000	950
$D_0^*$ (m)	11.20	12.00	11.20	12.50	11.20	11.55	11.20	12.00
$S$	$10^{-4}$	$10^{-4}$	$10^{-4}$	$10^{-4}$	$10^{-4}$	$10^{-4}$	$10^{-4}$	$10^{-4}$
$d_s^*$ (mm)	0.5	0.4	0.5	0.4	0.5	0.4	0.5	0.2
$\beta$	44.67	39.48	44.67	37.99	44.67	41.15	44.67	39.45
$\tau_*$	1.36	1.82	1.36	1.90	1.36	1.75	1.36	3.65
$d_s$ ( $\times 10^{-5}$ )	4.47	3.47	4.47	3.47	4.47	3.47	4.47	1.66

Simulation period is 300 years, with a time step assumed constant and equal to 2 years. The current configuration of the Mississippi is scaled by the mean of the two half widths, i.e.  $B_0^{*avg} = (B_0^{*u} + B_0^{*d})/2 = 488$  m and discretized through a polyline. The default point spacing is  $\Delta s/B_0^{*avg} = 1$ , and the mesh is periodically regridded during the simulation in order to keep the spacing in the range  $4/5 < \Delta s/B_0^{*avg} < 6/5$ .

The average migration rate of bends in the Lower Mississippi River is about 40 m/year in the upstream subreach and 60 m/year in the downstream subreach (Hudson and Kesel, 2000). For the sake of simplicity, here an average migration rate equal to  $\zeta^* = 50$  m/year is assumed, which corresponds to about  $\zeta_{day}^* = 13$  cm/day. Thus, the erodibility coefficient  $E$  of the dimensionless migration law (2.11) is chosen such that:

$$\frac{1}{L^*} \int_0^{L^*} \zeta^*(s) ds = \zeta_{day}^* \quad (5.55)$$

where  $L^*$  is the total length of the investigated reach. Since the river axis is discretized

through a polyline of  $N$  points nearly equispaced, the condition becomes:

$$\frac{1}{N} \sum_{i=1}^N E U_0^* U_{bi} = \zeta_{day}^* \quad (5.56)$$

where  $U_0^* = Q/(2B_0^* D_0^*)$  is the uniform flow velocity, evaluated as the average between the uniform flow velocities of the two subreaches, and  $U_{bi}$  is the dimensionless excess near-bank velocity, computed at the  $i$ th point of the axis. Finally, the erodibility coefficient to be used for the migration law (2.11) reads:

$$E = N \frac{\zeta_{day}^*}{U_0^*} \left( \sum_{i=1}^N U_{bi} \right)^{-1} \quad (5.57)$$

A constant erodibility coefficient is thus assigned to the floodplain at each time step, by using the latter equation. In addition, the floodplain is assumed to be homogeneous, thus neglecting the possible effects given by the progressive occurrence of oxbow lakes and scroll bars.

### 5.3 Results

Figure 5.7 reports an overall summary of the simulations, showing the characteristic discharge input and the simulated planform dynamics, over a time of 300 years. Differences in the migration history are qualitatively visible. All the simulated dynamics show a progressive lateral growth of the bends, with the formation of both upstream- and downstream-skewed meanders and of neck cutoffs. RUN-0 exhibits a lower number of cutoffs in the downstream subreach if compared to the other scenarios. The downstream subreach near  $y^*/B_0^* \simeq 400$  is similar for all the runs with the current sediment grain size (i.e. RUN-0, RUN-1, and RUN-2), whereas it is characterized by a faster dynamics, with the formation of a pair of oxbow lakes, when a finer sediment is taken (RUN-4). Similarly, the last part of the downstream subreach ( $y^*/B_0^* \simeq 200$ ) is more active in RUN-3 and RUN-4. On the other hand, the behaviour of the upstream subreach is somehow similar for all the simulations, leading to compound bends and some cutoffs. In particular, the planforms close to  $y^*/B_0^* \simeq 800$  are almost equal. RUN-0, however, shows generally a more twisted path, with a faster migration in the very upstream subreach ( $y^*/B_0^* \simeq 1000$ ), as well as RUN-4.

A quantitative comparison is given by the temporal trend of the half meander metrics introduced in Section 4.1, namely the length  $L_h$ , the asymmetry  $A_h$  and the sinuosity

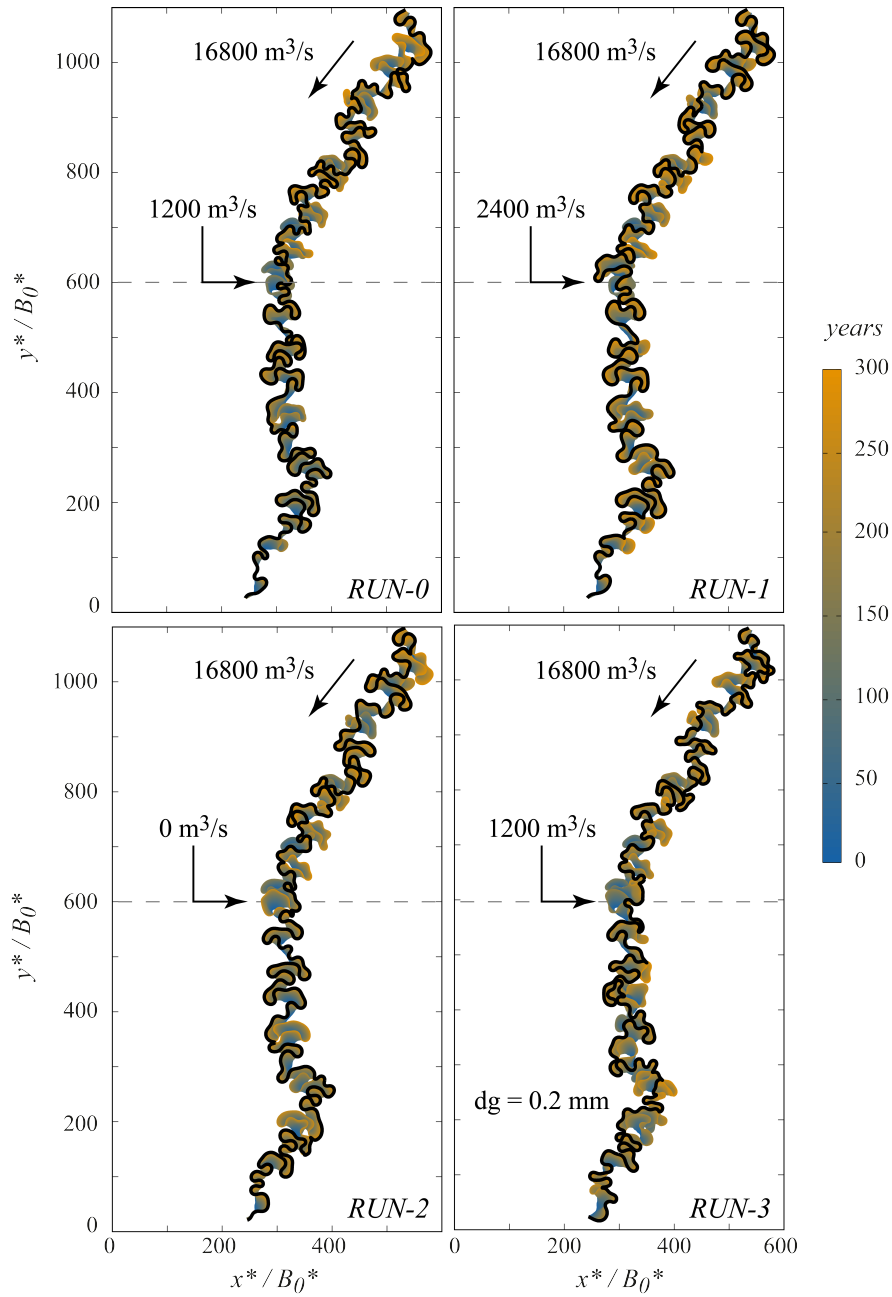


Figure 5.7: Simulated planform dynamics of the Mississippi River considering four different flow discharge scenarios. *RUN-0* corresponds to the actual mean flow discharge flowing in the Mississippi and Arkansas River, *RUN-1* and *RUN-2* have, respectively, a doubled and a zero discharge flowing in the Arkansas River; *RUN-4* assumes a stronger downstream fining in the Mississippi (see Table 5.1). Arkansas River confluence is marked with the dashed line. The Mississippi River flows from top to bottom.



Figure 5.8: Time evolution of the simulated half meander length  $L_h$ , asymmetry  $A_h$ , and sinuosity  $\sigma_h$  averaged over the upstream (left panels) and the downstream (right panels) subreaches of the Mississippi River, determined with respect to the confluence with the Arkansas River. RUN-0 corresponds to the actual scenario; RUN-1 and RUN-2 are characterized by a doubled and a zero discharge flowing from the Arkansas River; RUN-4 assumes a stronger downstream fining in the downstream Mississippi subreach (see Table 5.1).

$\sigma_h$ . All the parameters are spatially averaged over a given entire subreach at each time step (Figure 5.8). The trends relative to the upstream subreach show differences among them significantly smaller than those observed for the downstream subreach. In particular, the most visible difference is in the  $L_h$  trends, starting from a time  $t = 200$  years, when the trajectories associated with RUN-1 and RUN-2 diverge from those of RUN-0 and RUN-3. Average asymmetries and sinuosities have more similar trends, with  $A_h$  starting from slightly negative values (implying upstream-skewed meanders on average), getting slightly positive and then approaching zero with some oscillations. Sinuosity generally increases from 1.2 to about 1.7, with RUN-3 trend characterized by the larger fluctuations.

Time evolution of  $L_h$  in the downstream subreach are significantly different among each other, ranging from 20 to 35 times the characteristic half width  $B_0^{*avg}$ . Similarly to what happens in the upstream subreach,  $A_h$  changes from initially negative values to positive ones (superresonant behaviour on average), while the sinuosities get slightly larger values with respect to the upstream subreach. In general, the most *different* time evolution is that observed in RUN-3, i.e. the downstream fining scenario. The variation of discharge in the Arkansas River also induces some variations in the planform geometry. These differences in the half meander metrics are triggered by the internal boundary given by the presence of the Arkansas River confluence that induces localized, short-time variations, e.g. a faster or slower migrating meander, and anticipated or postponed cutoff occurrence.

## 5.4 Discussion

Currently most of the models used to simulate the evolution of meandering rivers implements governing equations based on relatively simplified assumptions, such as those of constant width, constant depth and uniform energy gradient. The first was recently relaxed by (Frascati and Lanzoni, 2013). Here the goal was to relax the assumption that at the leading order of approximation uniform flow conditions establish along the considered river reach. Thus the possible presence of two river subreaches, defined on the basis of hydrological factors (e.g., a tributary confluence), geological factors (e.g., variation in the valley slope), or geographic factors (e.g., localized narrowing of the valley) is here considered. All of these changes may be assumed as acting over a short length of the river such that, as a first approximation, the variations can be assumed to be

concentrated in a singular section splitting the domain in two subreaches characterized by uniform flow conditions.

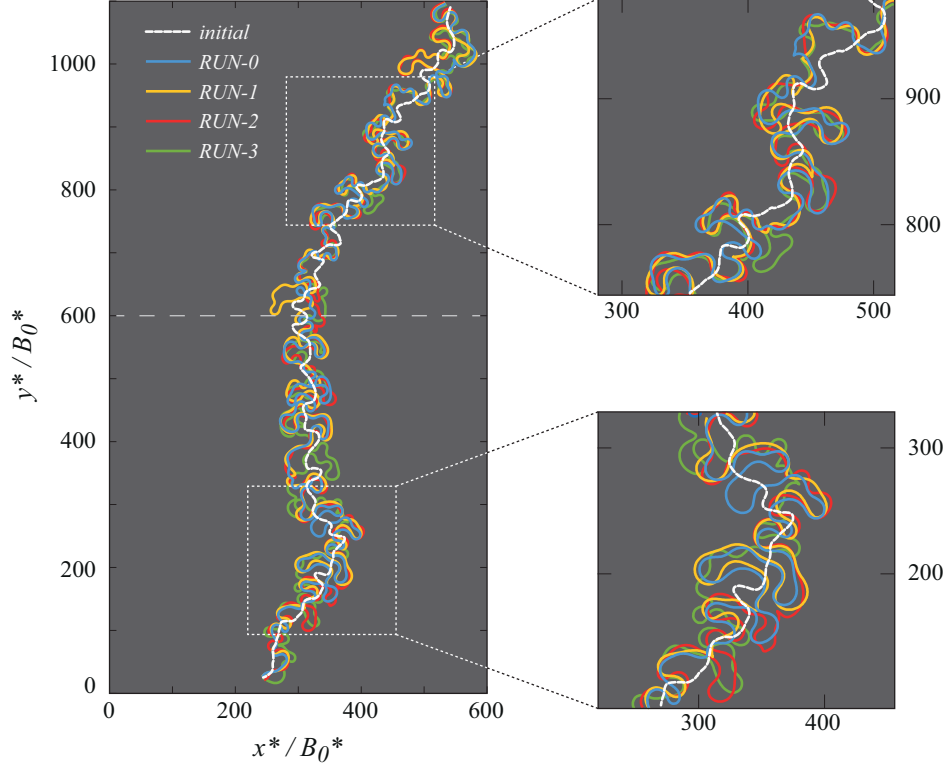


Figure 5.9: Comparison among simulated paths of the Mississippi River according to the four considered scenarios, after a simulation time of 300 year (see Table 5.1). Arkansas River confluence, i.e. the singular section which splits the domain in two subreaches, is marked with the dashed line. River flows from top to bottom.

The ZS model, owing to the presence of four particular solutions, ensures the coupling between the main uniform flow and the curvature-driven secondary flow that take place in the two subreaches. The resulting modelling framework was used to study the effects of the confluence of the Arkansas River in the Lower Mississippi River. Four different scenarios were considered by assuming the actual conditions as a reference case, and by varying the discharge delivered by the Arkansas River and the sedimentological characteristics of the downstream subreach. Simulations shows that the different effects triggered by the singular section are relatively localized and, rather than producing strong variation in the overall river dynamics (Figure 5.9), determine variations

at the meander scale and in the short term ( $\sim 50 - 100$  years). The localized effects associated with the internal boundary conditions become clear by considering the exponential decaying of the terms controlling the boundary conditions, i.e. those containing the coefficients  $c_{mj}^i$ . The river reach directly involved by the presence of the internal discontinuity is relatively short. However, the effects propagate as a chain reaction because of the river migration, up to involving the entire reach.

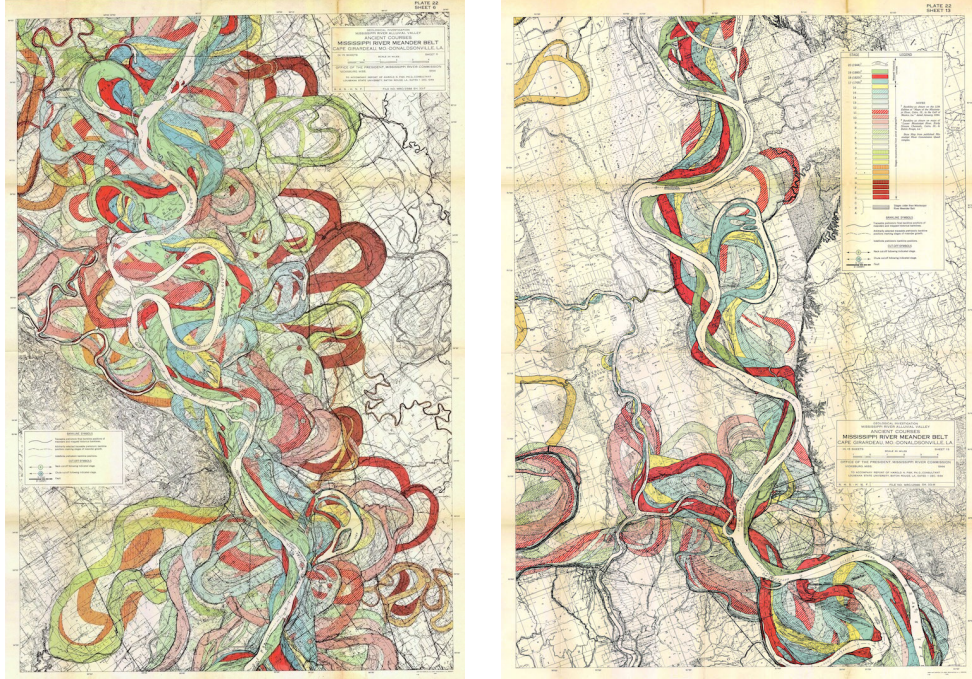


Figure 5.10: Historical maps developed by the Mississippi River Commission in 1944, showing the planform dynamics of a reach of the Mississippi River, starting from 1765.

Mississippi River constitutes a highly dynamic system (Figure 5.10), owing to the presence of many forcing factors acting within his huge catchment. As a consequence, more refined simulations should include forcing factors like the presence of confluences, the structure of the catchment, and the flood variability (Gutierrez et al., 2014). However, the low complexity model developed in this thesis provides a first robust attempt to treat spatially varying flow conditions as a sequence of uniform flows that establish in different subreaches, affecting the secondary flow fields responsible for channel migration. Including an internal boundary condition rather than considering a unique

uniform flow turns out to be crucial in the accuracy of short term simulations of meander evolution.

The developed framework may be extended to more complex scenarios by splitting the main domain in more than two subreaches coupled together through the shared singular sections. In this way, this generalized mathematical framework can be used to analyse a wider range of scenarios that exclude the presence of a single uniform flow throughout the investigated river reach, e.g. in addition of the above considered examples (tributary confluences, backwater effect), the presence of knickpoints into the domains of highly dynamics systems (Finnegan and Dietrich, 2011; Sylvester and Covault, 2016), or anthropogenic effects on fluvial systems (Edwards et al., 2016).



## Chapter 6

# Conclusions and future developments

The aim of this thesis was twofold: i) to investigate how a self-formed floodplain, produced by the migration of river bends and the cutoff of mature meanders, can affect the river dynamics itself; ii) to consider the presence of a boundary condition internal to the investigated river reach, able to affect the main flow field and thus the curvature-driven secondary flow.

The first aim requires to account for the presence of heterogeneous floodplain features due to the occurrence of cutoffs (oxbow lakes) and bend migration (scroll bars) that modify the superficial structure of the floodplain through which the river flows. From a numerical point of view, the role of oxbow lakes (leading to the formation of clay plugs that slow down the river migration) can be included together with that of other geomorphic units (ridge-and-swale topography of the scroll bars, vegetation cover) which contribute to generate heterogeneities in terms of floodplain erodibility.

Statistical and spectral analyses (SSA, MSSA, PCA and FA) proved to be useful tools for a quantitative description of the complex meander shapes.

The role of the self-formed floodplain heterogeneities is crucial since they drive the long-term migration of meandering rivers, affecting the temporal evolution and the spatial distribution of half meander metrics, eventually leading to a closer statistical similarity between simulated and natural planform shapes. The difference in erodibility between floodplain, oxbow lakes and points bars thus results a crucial ingredient for the numerical simulations of meander dynamics. Indeed, it is able to affects the migration

history in addition to the well known effects of bank erosion due to by the curvature-driven flow field.

The presence of boundary conditions internal to the flow field is another ingredient that can play a significant role in meander dynamics. It can be handled mathematically by splitting the domain in two subreaches, which need to be suitably coupled at the internal boundary section. The presence of an internal forcing generates perturbations which can propagate either upstream or downstream. Localized internal flow variations may derive from a change in discharge (because of a tributary confluence), bed slope (because of a knickpoint), bed sediment composition or cross section geometry. The mathematical framework may be easily extended to domains which contain more than one internal boundary. The application of the methodology developed in the present thesis to a real case, namely a reach of the Lower Mississippi close to the confluence with the Arkansas River, revealed that variations in the tributary discharge or bed sediment composition lead to short-term variations at the meander scale in terms of planform dynamics, rather than long-term, reach scale effects. The present mathematical framework may be extended to more complex scenarios by splitting the domain in more than two parts. For example, a gradually-varying flow can be treated as a sequence of local uniform flow and coupled together by internal boundary conditions, instead of considering a unique uniform mean flow.

The ultimate goal is to provide robust and reliable tools for the study of river dynamics, widening the range of applicability of existing mathematical frameworks possibly within an interdisciplinary perspective, including geological, geomorphological, and biological factors. To this aim, various hypotheses about river morphodynamics and floodplain features imposed in this thesis still need to be relaxed. Variations in cross-sectional geometry, resulting for example from the bank pull-bar push interplay and leading to channel width modulations, as well temporally varying boundary conditions (e.g., fluctuations in formative discharge and sediment supply) surely has to be considered. Temporal gradients in point bar erodibility (due, for example, to vegetation dynamics) and in the accommodation space over the floodplain (due to either uplift or subsidence) are additional physical processes acting at different temporal scales that should be accounted for when dealing with long term evolution of alluvial rivers. Similarly, periodic climatic variations associated with glaciations and droughts, affecting the flooding frequency of the floodplain, are other issues that needs to be tackled. Fi-

nally, a probabilistic approach, driven by data assimilation techniques would possibly be required to fully reproduce the complexity of alluvial river systems.



# List of Tables

4.1	Different scenarios considered for the erosional resistance of the various geomorphic units (i.e. pristine floodplain, oxbow lakes, scroll bars) used for the test case . . . . .	39
4.2	Sets of initial parameter used in the numerical simulations to build a database of synthetic planforms. . . . .	46
4.3	Database of natural river paths used for the multivariate statistical comparison with numerically generated meanders . . . . .	52
4.4	Suite of morphometric parameters considered to characterize and to compare the meander planforms through PCA. . . . .	63
5.1	Sets of input parameters considered for the simulation of the Mississippi River migration in the presence of the confluence with the Arkansas River confluence. . . . .	93



# List of Figures

1.1	A Landsat detail of Jurua River floodplain, Brazil. . . . .	10
1.2	Examples of self-formed floodplains. . . . .	12
1.3	Sketch of the flow field that establishes into a river bend and of the erosion and deposition processes leading to channel migration. . . . .	14
1.4	A Landsat detail of the confluence of Arkansas River into Mississippi River	15
2.1	Reference systems and notation for the river planform and cross-section.	18
2.2	Sketch of the migration of a point lying on the channel axis. . . . .	21
2.3	Natural and numerical neck cutoff process, with the formation of two new environments, namely the oxbow lake and the inner scroll bar. . . .	23
2.4	Example of a simulated planform dynamics, with the formation of scroll bars and oxbow lakes. . . . .	25
2.5	Typical behaviours of the four characteristic exponents $\lambda_{mj}$ of the ZS approach as a function of the half width to depth ratio $\beta$ , compared to the characteristic exponent $\lambda_0$ of the IPS approach. . . . .	28
4.1	Migration history of the river planforms, simulated using the ZS approach and starting from a straight path slightly perturbed in the transverse direction. . . . .	42
4.2	Time evolution of the mean length, the mean asymmetry and the mean sinuosity of the simulated half meanders, for different sets of erodibility environments. . . . .	44
4.3	Normalized SSA spectra of the time signals of half meander geometries generated by the ZS- and the IPS-flow field models, compared over three different heterogeneity scenarios. . . . .	50

4.4	Normalized MSSA spectra of the time signals of half meander geometries generated by the ZS- and the IPS-flow field models, compared over three different heterogeneity scenarios. . . . .	51
4.5	Binning of the spatial series of the half meander metrics (length, asymmetry, sinuosity) with comparison between natural planforms and numerically generated planforms (ZS and IPS approaches), considering three different erodibility scenarios of the floodplain: softening scroll bars, homogeneous valley, hardening scroll bars. . . . .	55
4.6	Statistics of the binned spatial series of the half meander metrics (length, asymmetry, sinuosity) with comparison between natural planforms and numerically generated planforms (ZS and IPS approaches), considering three different erodibility scenarios of the floodplain: softening scroll bars, homogeneous valley, hardening scroll bars. . . . .	56
4.7	Normalized MSSA spectra of the spatial multivariate signals referred to the half meander geometry. . . . .	57
4.8	Normalized power spectra of the distributions of full meander curvature.	59
4.9	Normalized SSA of the distributions of the full meander curvature. . . .	61
4.10	Three-dimensional scatter plot of the first three components of morphometric data of natural rivers and simulated paths processed by Principal Component Analysis (PCA). . . . .	64
4.11	Normalized eigenvalue spectrum of the correlation matrix of the Principal Component Analysis (PCA). . . . .	65
5.1	Sketch of a meandering river affected by a singular section which introduces variation in the main flow and in the curvature-driven secondary circulation. . . . .	70
5.2	Typical behaviour of the exponential terms appearing in the solution of the ZS model for five values of the characteristic exponent $\lambda_{mj}$ . . . . .	75
5.3	Historical maps showing the planform dynamics of a reach of the Mississippi River, from 1765 to 1944. . . . .	87
5.4	Composition of Landsat images of the Mississippi River between Memphis, Tennessee (US), and Natchez, Mississippi (US). . . . .	89
5.5	Average daily discharge of Mississippi River at Vicksburg gauge station, from 2009 to 2015. . . . .	90



5.6	Average daily discharge of Arkansas River at Murray Dam gauge station near Little Rock, from 2009 to 2015. . . . .	91
5.7	Simulated planform dynamics of the Mississippi River considering four different scenarios of discharge flowing in Arkansas River and sediment distribution. . . . .	95
5.8	Time evolution of the simulated half meander metrics, averaged over the upstream and the downstream subreaches of the Mississippi River, determined with respect to the confluence with the Arkansas River. . . .	96
5.9	Comparison among simulated paths of the Mississippi River according to the four considered scenarios, after a simulation of 300 years. . . . .	98
5.10	Historical maps showing the planform dynamics of a reach of the Mississippi River, from 1765 to 1944. . . . .	99



# Bibliography

- Aalto, R. E., Lauer, J. W., and Dietrich, W. E. (2008). Spatial and temporal dynamics of sediment accumulation and exchange along Strickland River floodplains (Papua New Guinea) over decadal-to-centennial timescales. *Journal of Geophysical Research*, 113(F1):F01S04.
- Alin, S. R., Aalto, R. E., Goni, M. A., Richey, J. E., and Dietrich, W. E. (2008). Biogeochemical characterization of carbon sources in the Strickland and Fly rivers, Papua New Guinea. *Journal of Geophysical Research: Earth Surface*, 113(1):1–21.
- Allmendinger, N. E., Pizzuto, J. E., Potter, N., Johnson, T. E., and Hession, W. C. (2005). The influence of riparian vegetation on stream width, eastern Pennsylvania, USA. *Bulletin of the Geological Society of America*, 117(1-2):229–243.
- Asahi, K., Shimizu, Y., Nelson, J., and Parker, G. (2013). Numerical simulation of river meandering with self-evolving banks. *Journal of Geophysical Research: Earth Surface*, 118:2208–2229.
- Camporeale, C., Perona, P., Porporato, A., and Ridolfi, L. (2005). On the long-term behavior of meandering rivers. *Water Resources Research*, 41(12):1–13.
- Camporeale, C., Perucca, E., and Ridolfi, L. (2008). Significance of cutoff in meandering river dynamics. *Journal of Geophysical Research: Earth Surface*, 113(1):1–11.
- Constantine, C. R., Dunne, T., and Hanson, G. J. (2009). Examining the physical meaning of the bank erosion coefficient used in meander migration modeling. *Geomorphology*, 106(3-4):242–252.
- Constantine, J. A., Dunne, T., Piégay, H., and Mathias Kondolf, G. (2010). Controls

- on the alluviation of oxbow lakes by bed-material load along the Sacramento river, California. *Sedimentology*, 57(2):389–407.
- Crosato, A. (1990). Simulation of meandering river process. Technical Report 3, Delft university of Tecnology, Delft (NL), Delft.
- David, S. R., Edmonds, D. A., and Letsinger, S. L. (2016). Controls on the occurrence and prevalence of floodplain channels in meandering rivers. *Earth Surface Processes and Landforms*.
- Day, G., Dietrich, W. E., Rowland, J. C., and Marshall, A. (2008). The depositional web on the floodplain of the Fly River, Papua New Guinea. *Journal of Geophysical Research: Earth Surface*, 113(F1).
- Dunne, T., Mertes, L., Meade, R., Richey, J. E., and Forsberg, B. (1998). Exchanges of sediment between the floodplain and channel of the Amazon River in Brazil. *Geological Society of America Bulletin*, 110(4):450–467.
- Edwards, B. L., Keim, R. F., Johnson, E. L., Hupp, C. R., Marre, S., and King, S. L. (2016). Geomorphic adjustment to hydrologic modifications along a meandering river: Implications for surface flooding on a floodplain. *Geomorphology*, 269:149–159.
- Einstein, A. (1926). The cause of the formation of meanders in the courses of rivers and of the so-called baers law. *Die Naturwissenschaften*, 14(11):223–224.
- Eke, E. C., Parker, G., and Shimizu, Y. (2014). Numerical modeling of erosional and depositional bank processes in migrating river bends with self-formed width: morphodynamics of barp ush and bank pull. *Journal of Geophysical Research: Earth Surface*, 119(2):1–29.
- Engelund, F. and Hansen, E. (1967). A monograph on sediment transport in alluvial stream. Technical report, Technical University of Denmark, Copenhagen.
- Finnegan, N. J. and Dietrich, W. E. (2011). Episodic bedrock strath terrace formation due to meander migration and cutoff. *Geology*, 39(2):143–146.
- Frascati, A. (2009). *Morphodynamic regime and long-term modelling of meandering rivers*. PhD thesis.

- Frascati, A. and Lanzoni, S. (2009). Morphodynamic regime and long-term evolution of meandering rivers. *Journal of Geophysical Research: Earth Surface*, 114(2):1–12.
- Frascati, A. and Lanzoni, S. (2010). Long-term river meandering as a part of chaotic dynamics? A contribution from mathematical modelling. *Earth Surface Processes and Landforms*, 35(7):791–802.
- Frascati, A. and Lanzoni, S. (2013). A mathematical model for meandering rivers with varying width. *Journal of Geophysical Research: Earth Surface*, 118(3):1641–1657.
- Frings, R. M. (2008). Downstream fining in large sand-bed rivers. *Earth-Science Reviews*, 87(1):39–60.
- Gagliano, S. M. and Howard, P. C. (1984). The neck cutoff oxbow lake cycle along the Lower Mississippi River. In CM, E., editor, *River Meandering, Proceedings of the Conference Rivers 1983*, pages 147–158. ASCE. New Orleans.
- Gautier, E., Brunstein, D., Vauchel, P., Rouler, M., Fuertes, O., Guyot, L., Darozzes, J., and Bourrel, L. (2007). Temporal relation between meander deformation, water discharge and sediment fluxes in the floodplain of the Rio Beni (Bolivian Amazonia). *Earth Surface Processes and Landforms*, 32:230–248.
- Gay, G. R., Gay, H. H., Gay, W. H., Martinson, H. A., Meade, R. H., and Moody, J. A. (1998). Evolution of cutoffs across meander necks in Powder River, Montana, USA. *Earth Surface Processes and Landforms*, 23:651–662.
- Ghil, M., Allen, M. R., Dettinger, M. D., Ide, K., Kondrashov, D., Mann, M. E., Robertson, A. W., Saunders, A., Tian, Y., Varadi, F., and Yiou, P. (2002). Advanced spectral methods for climate time series. *Reviews of Geophysics*, 40(1):1–41.
- Grenfell, M., Aalto, R. E., and Nicholas, A. P. (2012). Chute channel dynamics in large, sand-bed meandering rivers. *Earth Surface Processes and Landforms*, 37(3):315–331.
- Güneralp, İ. and Rhoads, B. L. (2011). Influence of floodplain erosional heterogeneity on planform complexity of meandering rivers. *Geophysical Research Letters*, 38(14):2–7.
- Gutierrez, R. R., Abad, J. D., Choi, M., and Montoro, H. (2014). Characterization of confluences in free meandering rivers of the Amazon basin. *Geomorphology*, 220:1–14.

- Han, B. and Endreny, T. (2014). Detailed river stage mapping and head gradient analysis during meander cutoff in a laboratory river. *Water Resources Research*, 50:1689–1703.
- Hooke, J. M. (1995). River channel adjustment to meander cutoffs on the River Bollin and River Dane, northwest England. *Geomorphology*, 14(3):235–253.
- Hooke, J. M. (2004). Cutoffs galore!: occurrence and causes of multiple cutoffs on a meandering river. *Geomorphology*, 61(3-4):225–238.
- Hormann, K. and Agathos, A. (2001). The point in polygon problem for arbitrary polygons. *Computational Geometry: Theory and Applications*, 20(3):131–144.
- Howard, A. (1996). Modelling channel evolution and floodplain morphology. *Floodplain Processes*, pages 15–62.
- Howard, A. D. and Hemberger, A. T. (1991). Multivariate characterization of meandering. *Geomorphology*, 4:161.186.
- Howard, A. D. and Knutson, T. R. (1984). Sufficient conditions for river meandering: a simulation approach. *Water Resources Research*, 20(11):1659–1667.
- Hudson, P. F. and Kesel, R. H. (2000). Channel migration and meander-bend curvature in the lower Mississippi River prior to major human modification. *Geology*, 28(6):531–534.
- Ikeda, S., Parker, G., and Sawai, K. (1981). Bend theory of river meanders. Part 1. Linear development. *Journal of Fluid Mechanics*, 112:363–377.
- Johannesson, H. and Parker, G. (1989). Linear theory of river meanders. *Water Resources Monograph*, 12:181–214.
- Kleinhans, M. G. (2010). Sorting out river channel patterns. *Progress in Physical Geography*, 34(3):287–326.
- Kleinhans, M. G. and van den Berg, J. H. (2011). River channel and bar patterns explained and predicted by an empirical and a physics-based method. *Earth Surface Processes and Landforms*, 36:721–738.

- Lancaster, S. T. and Bras, R. L. (2002). A simple model of river meandering and its comparison to natural channels. *Hydrological Processes*, 16(1):1–26.
- Lane, E. W. (1957). *A study of the shape of channels formed by natural streams flowing in erodible material*. US Army Engineer Division, Missouri River.
- Lanzoni, S. and Seminara, G. (2006). On the nature of meander instability. *Journal of Geophysical Research*, 111(4):1–14.
- Lanzoni, S., Siviglia, A., Frascati, A., and Seminara, G. (2006). Long waves in erodible channels and morphodynamic influence. *Water Resources Research*, 42:1–15.
- Latrubesse, E. M. (2008). Patterns of anabranching channels: the ultimate end-member adjustment of mega rivers. *Geomorphology*, 101(1-2):130–145.
- Lauer, J. W. and Parker, G. (2008). Net local removal of floodplain sediment by river meander migration. *Geomorphology*, 96(1-2):123–149.
- Lazarus, E. D. and Constantine, J. A. (2013). Generic theory for channel sinuosity. *PNAS*, 110(21):8447–8452.
- Leopold, L. B. and Wolman, M. G. (1957). *River channel patterns: braided, meandering, and straight*. US Government Printing Office.
- Lewin, J. and Ashworth, P. J. (2014). The negative relief of large river floodplains. *Earth-Science Reviews*, 129:1–23.
- Makaske, B., Smith, D. G., and Berendsen, H. J. (2002). Avulsions, channel evolution and floodplain sedimentation rates of the anastomosing upper Columbia River, British Columbia, Canada. *Sedimentology*, 49(5):1049–1071.
- Marani, M., Lanzoni, S., and Zandolin, D. (2002). Tidal meanders. *Water Resources Research*, 38(11).
- Miall, A. D. (1985). Architectural-element analysis: a new method of facies analysis applied to fluvial deposits.
- Motta, D., Abad, J. D., Langendoen, E. J., and Garcia, M. H. (2012a). A simplified 2d model for meander migration with physically-based bank evolution. *Geomorphology*, 163:10–25.

- Motta, D., Abad, J. D., Langendoen, E. J., and García, M. H. (2012b). The effects of floodplain soil heterogeneity on meander planform shape. *Water Resources Research*, 48(9):1–17.
- Nanson, G. C. (1980). Point bar and floodplain formation of the meandering Beatton River, northeastern British Columbia, Canada. *Sedimentology*, 27(1):3–29.
- Nicoll, T. J. and Hickin, E. J. (2010). Planform geometry and channel migration of confined meandering rivers on the Canadian prairies. *Geomorphology*, 116(1-2):37–47.
- Nitttrouer, J. A., Mohrig, D., Allison, M. A., and Peyret, A. P. B. (2011). The lowermost Mississippi River: a mixed bedrock-alluvial channel. *Sedimentology*, 58(7):1914–1934.
- Nordin, C. F. and Queen, B. S. (1992). Particle size distributions of bed sediments along the thalweg of the Mississippi River, Cairo, Illinois, to Head of Passes, September 1989. Technical report, DTIC Document.
- Orfanidis, S. J. (1995). *Introduction to signal processing*. Prentice-Hall, Inc.
- Parker, G. (1976). On the cause and characteristic scales of meandering and braiding in rivers. *Journal of fluid mechanics*, 76(03):457–480.
- Parker, G. (1990). Surface-based bedload transport relation for gravel rivers. *Journal of Hydraulic Research*, 28(4):417–436.
- Parker, G., Shimizu, Y., Wilkerson, G. V., Eke, E. C., Abad, J. D., Lauer, J. W., Paola, C., Dietrich, W. E., and Voller, V. R. (2011). A new framework for modeling the migration of meandering rivers. *Earth Surface Processes and Landforms*, 36(1):70–86.
- Perucca, E., Camporeale, C., and Ridolfi, L. (2005). Nonlinear analysis of the geometry of meandering rivers. *Geophysical Research Letters*, 32(3):1–4.
- Perucca, E., Camporeale, C., and Ridolfi, L. (2006). Influence of river meandering dynamics on riparian vegetation pattern formation. *Journal of Geophysical Research: Biogeosciences*, 111(1):1–9.
- Perucca, E., Camporeale, C., and Ridolfi, L. (2007). Significance of the riparian vegetation dynamics on meandering river morphodynamics. *Water Resources Research*, 43(3):1–10.



- Rowland, J. C., Lepper, K., Dietrich, W. E., Wilson, C. J., and Sheldon, R. (2005). Tie channel sedimentation rates, oxbow formation age and channel migration rate from optically stimulated luminescence (OSL) analysis of floodplain deposits. *Earth Surface Processes and Landforms*, 30(9):1161–1179.
- Schumm, S. A. (1986). Alluvial river response to active tectonics. *Active tectonics*, pages 80–94.
- Schuurman, F., Shimizu, Y., Iwasaki, T., and Kleinhans, M. G. (2016). Dynamic meandering in response to upstream perturbations and floodplain formation. *Geomorphology*, 253:94–109.
- Schwenk, J., Lanzoni, S., and Foufoula-Georgiou, E. (2015). The life of a meander bend : connecting shape and dynamics via analysis of a numerical model. *Journal of Geophysical Research: Earth Surface*, 120:690–710.
- Seminara, G. (2006). Meanders. *Journal of Fluid Mechanics*, 554:271–297.
- Seminara, G., Zolezzi, G., Tubino, M., and Zardi, D. (2001). Downstream and upstream influence in river meandering. Part 2. Planimetric development. *Journal of Fluid Mechanics*, 438:213–230.
- Slingerland, R. and Smith, N. D. (2004). River Avulsions and Their Deposits. *Annu. Rev. Earth Planet. Sci.*, 32(Qian 1990):257–285.
- Smith, D. G., Hubbard, S. M., Leckie, D. A., and Fustic, M. (2009). Counter point bar deposits: lithofacies and reservoir significance in the meandering modern Peace River and ancient McMurray Formation, Alberta, Canada. *Sedimentology*, 56(6):1655–1669.
- Solari, L., van Oorschot, M., Belletti, B., Hendriks, D., Rinaldi, M., and Vargas-Luna, A. (2016). Advances on modelling riparian vegetation - hydromorphology interactions. *River Research and Applications*, 32:164–178.
- Stølum, H. H. (1998). Planform geometry and dynamics of meandering rivers. *Bulletin of the Geological Society of America*, 110(11):1485–1498.
- Sun, T., Meakin, P., Jøssang, T., and Schwarz, K. (1996). A simulation model for meandering rivers. *Water Resources Research*, 32(9):2937–2954.

- Swanson, K. M., Watson, E., Aalto, R. E., Lauer, J. W., Bera, M. T., Marshall, A., Taylor, M. P., Apte, S. C., and Dietrich, W. E. (2008). Sediment load and floodplain deposition rates: Comparison of the Fly and Strickland rivers, Papua New Guinea. *Journal of Geophysical Research: Earth Surface*, 113(1):2–17.
- Sylvester, Z. and Covault, J. A. (2016). Development of cutoff-related knickpoints during early evolution of submarine channels. *Geology*, 44(10):835–838.
- Toonen, W. H., Kleinhans, M. G., and Cohen, K. M. (2012). Sedimentary architecture of abandoned channel fills. *Earth Surface Processes and Landforms*, 37(4):459–472.
- van De Lageweg, W. I., van Dijk, W. M., Baar, A. W., Rutten, J., and Kleinhans, M. G. (2014). Bank pull or bar push : What drives scroll-bar formation in meandering rivers ? *Geology*, pages 1–4.
- Van den Berg, J. H. (1995). Prediction of alluvial channel pattern of perennial rivers. *Geomorphology*, 12(4):259–279.
- van Oorschot, M., Kleinhans, M. G., Geerling, G., and Middelkoop, H. (2016). Distinct patterns of interaction between vegetation and morphodynamics. *Earth Surface Processes and Landforms*, 41(6):791–808.
- Van Rijn, L. C. (1984a). Sediment transport, part II: suspended load transport. *Journal of Hydraulic Engineering*, 110(11):1613–1641.
- Van Rijn, L. C. (1984b). Sediment transport, part III: bed forms and alluvial roughness. *Journal of Hydraulic Engineering*, 110(12):1733–1754.
- Vautard, R. and Ghil, M. (1989). Singular spectrum analysis in nonlinear dynamics with appliations to paleoclimatic time series. *Physica D*, 35:395–424.
- Wickert, A. D., Martin, J. M., Tal, M., Kim, W., Sheets, B., and Paola, C. (2013). River channel lateral mobility: Metrics, time scales, and controls. *Journal of Geophysical Research: Earth Surface*, 118(2):396–412.
- Wright, S. and Parker, G. (2005). Modeling downstream fining in sand-bed rivers. I: Formulation. *Journal of Hydraulic Research*, 43(6):613–620.

- Zen, S., Zolezzi, G., Toffolon, M., and Gurnell, A. M. (2016). Biomorphodynamic modelling of inner bank advance in migrating meander bends. *Advances in Water Resources*, 93:166–181.
- Zolezzi, G. and Seminara, G. (2001). Downstream and upstream influence in river meandering. Part 1. General theory and application to overdeepening. *Journal of Fluid Mechanics*, 438:183–211.